Optical modeling and characterization of transparent conductive oxides

Implementation in thin film solar cells

Lorena Hendrix

TUDelft

Optical modeling and characterization of transparent conductive oxides and the implementation of thin film solar cells

by

Lorena Hendrix

to obtain the degree of Master of Science
at the Delft University of Technology,
to be defended publicly on Wednesday April 26, 2023 at 9:00 AM.

Supervisors:	Prof. dr. ir. Arno Smets,	TU Delft
	Dr. ir. Rudi Santbergen,	TU Delft
	Ir. Federica Saitta,	TU Delft
Thesis committee:	Dr. ir. Tom Savenije,	TU Delft
	Dr. ir. Stephan Eijt,	TU Delft
	Dr. ir. Paula Perez Rodriguez,	TU Delft

An electronic version of this thesis is available at `http://repository.tudelft.nl/`.

TUDelft

Acknowledgements

Abstract

To make silicon thin film solar cells attractive to the market, their efficiencies should reach the efficiencies of the dominant crystalline silicon solar cell. Therefore the search for ways to improve the efficiency of silicon thin film solar cells continues. TCO front contact layers and back reflector layers play a significant role in the increase of thin film solar cell efficiencies. For the optical characterization of these TCO layers, commonly used methods are found to differ significantly in results regarding the extinction coefficient which makes their accuracy questionable.

This research consists of two main parts. For the first part, the commonly used optical characterization methods spectroscopic ellipsometry and spectrophotometry + data analysis in SCOUT are analyzed in accuracy and compared to newly introduced methods using spectrophotometry + data analysis in GenPro4 and photothermal deflection spectroscopy + data analysis in GenPro4 to build a guide on optical characterization of TCO materials. For the second part, the optical response determined using the software GenPro4 of a double junction silicon thin film solar cell for a novel bi-layer front contact design consisting of IOH and i-ZnO will be compared to the optical response for standard used AZO, and ITO single layers to find the best front contact design. Furthermore, the optical response of a double junction silicon thin film solar cell for a back reflector containing an i-ZnO layer on top of the silver back contact will be compared to the optical response for a back reflector containing an AZO layer on top of the silver back contact to find the best back reflector design.

From the results of the optical characterization methods, it is concluded that photothermal deflection spectroscopy + data analysis in GenPro4 is the most accurate method for determining the extinction coefficient of a TCO material. The results of the optical simulations for front contact TCO and back reflector TCO designs showed that the bi-layer can enhance the optical response of a double junction silicon thin film solar cell significantly compared to the AZO and ITO single layers. The i-ZnO TCO back reflector layer was found to induce less parasitic absorption and therefore a better optical response of the double junction silicon thin film solar cell.

Nomenclature

Acronyms

a-Si   amorphous silicon

AID   Angular intensity distribution

AZO   Aluminum doped zinc-oxide

BR   Back reflector

FC   Front contact

FCA   Free carrier absorption

FlamingoPV   Flexible Lightweight Advanced Materials In Next Generation of PV

GP4   GenPro4

i-ZnO   intrinsic zinc-oxide

IOH   Hydrogenated indium oxide

ITO   Indium doped tin-oxed

MSE   Mean squared error

nc-Si   nanocrystalline silicon

NIR   Near infra-red

PDS   Photothermal Deflection Spectroscopy

PVMD group   Photovoltaic materials and devices group at TU Delft

RT   Reflectance and transmittance

SC   SCOUT

SE   Spectroscopic Ellipsometry

SP   Spectrophotometry

SR   Surface roughness

TCO   Transparent Conductive Oxide

UV   Ultra violet

Vis   Visible

Symbols

α	Absorption coefficient	cm^{-1}
Δ	Delta measurement data of SE	^{o}
λ	Wavelength	nm
ψ	Psi measurement data of SE	^{o}

σ_d, SE	Error in with SE calculated thickness	nm
σ_{RMS}	Root-mean-square surface roughness	nm
σ_{SR}	Error in calculated surface roughness	nm
θ	Initial angle of light for SE measurement	^{o}
A	Absorptance	$-$
AR	Aspect ratio	$\%$
d_{back}	Thickness back reflector TCI layer	nm
$d_{bilayer}$	The total thickness of the bi-layer	nm
d_{front}	Thickness front contact TCO layer	nm
d_{i-ZnO}	Thickness i-ZnO layer	nm
d_{IOH}	Thickness IOH layer	nm
d_{SE}	Thickness calculated using SE	nm
d_{TCO}	Thickness TCO layer	nm
J_{ph}	Photo current density	mS/cm^2
k	Extinction coefficient	$-$
L_c	Surface correlation length	nm
N	Complex refractive index	$-$
n	Refractive index	$-$
N_e	Electron charge carrier density	$-$
P	Deposition power	W
p	Pressure during deposition	$mbar$
p_{H_2O}	Partial water pressure during deposition	$mbar$
R	Reflectance	$-$
R_{sh}	Sheet resistance	Ω/sq
SR	Surface roughness	nm
T	Transmittance	$-$
T_{an}	Annealing temperature	^oC
t_{dep}	Deposition time	s
T_{heater}	Heater temperature during deposition	^oC

Contents

1

Introduction

Costs reduction in the photovoltaic (PV) system is an important issue when it comes to further market growth and development of solar power generation. Therefore, research is done on thinner, and thus also cheaper, solar cells: thin film solar cells [24]. To make silicon thin film solar cells attractive to the market, they should have efficiencies that are close to conventional silicon solar cells. For conventional crystalline silicon solar cells, efficiencies of up to 27% were achieved [10]. For silicon thin film solar cells efficiencies up to 14% were achieved for triple junctions [29], [30]. Therefore the search for ways to improve the efficiency of silicon thin film solar cells continues.

1.1. Thin film solar cells

1.1.1. Working principle

When a photon is absorbed in the material, its energy is used to excite an electron from initial energy to higher energy. Only those two energy levels exist such that their difference is equal to the photon energy, $E_p = hv$, the photon can be absorbed. In an ideal semiconductor, only electron energy levels below the valence band edge E_V and above the conduction band edge E_C exist. This creates a bandgap $E_G = E_C - E_V$ in which no allowed energy states exist. A photon with a smaller energy than E_G will not be absorbed and will propagate through the material without interacting [36].

When an electron excites from energy in the valence band to an energy in the conduction band, a void is created in the valance band that behaves like a particle with a positive elementary charge. This void is called a hole and together with the excited electron, an electron-hole pair is created.In the case of a thin film silicon solar cell, the separation of the electron-hole pair happens due to the characteristics of a p-i-n junction (or n-i-p junction). A built-in electric field will be created between the p- and n-doped layer and across the intrinsic layer. Because of this electric field, the photo-generated charge carrier will move through the intrinsic layer. The holes in the valence band move up the slope toward the p-layer and the electrons in the conduction band move down the slope toward the n-layer due to drift. The separated charge carriers are extracted from the solar cell with electrical contacts and can therefore produce a current within an external circuit [36].

1.1.2. Solar cell structure

This research focuses on a thin film solar cell deposited with a superstrate configuration. This means that the deposition order starts with depositing a TCO layer serving as front contact on a glass superstrate. Then the p-doped layer, intrinsic layer, and n-doped layer are deposited, multiple times depending on the number of junctions. Lastly, a TCO back-reflector layer and metal contact layer are deposited. The light will first go through the layer that also has been deposited first.

In this research, a double junction (tandem) thin film solar cell is investigated. In figure 1.1, the structure of a tandem thin film solar cell in superstrate configuration is shown. The electrodes would in this case be placed on top of the front contact TCO layer and at the bottom attached to the metal contact layer.
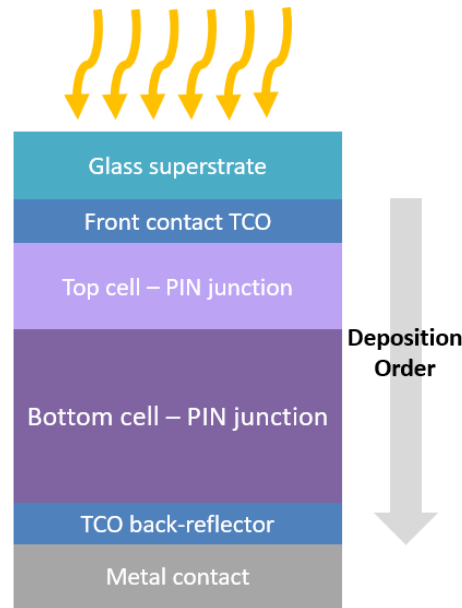
Figure 1.1: The extinction coefficient obtained using both SE and SP+SCOUT of an i-ZnO thin film

1.2. Light management

In the previous section, the working principle of a thin film solar cell was explained together with the role of the p-i-n junction within the process of the generation of electricity from light. In this section, it will be discussed how the performance of a solar cell can be enhanced by adding more junctions, TCO layers, and metal contact layers as shown in the cell structure in figure 1.1.

The thicker the absorber layers, the more light can be absorbed and converted to electricity. This is challenging when it comes to thin film solar cells, as the layers are kept very thin in order to reduce costs. There are ways to get the efficiencies of thin film solar cells closer to the efficiency values of conventional c-Si solar cells without increasing the thickness of the absorber layers: increasing the part of the light spectrum that is utilized, improving the charge carrier transport towards the electrodes, lowering the primary reflectance of the light, and increasing the optical path length of the photons passing through the solar cell.

1.2.1. Spectral Utilisation

The photons arriving at the solar cell carry a certain amount of energy depending on the wavelength according to the following formula.

$$E_{ph} = \frac{hc}{\lambda} \tag{1.1}$$

Here is h, the Planck constant, c, the speed of light, and λ, the wavelength. To get a better-performing solar cell, a bigger part of the light spectrum should be absorbed. Which wavelengths are absorbed by the absorbing layer depends on the band gap. The intrinsic a-Si layer, for example, has a band gap of about $1.8eV$ and will therefore absorb light until about $700nm$. Although a-Si is transparent for wavelengths higher than $700nm$, these wavelengths do contain a significant amount of energy that can be utilized for conversion into electricity. Therefore, junctions are added to the solar cell with different materials. For a double junction thin film solar cell, for example, the bottom junction should contain an intrinsic layer of a material that has a lower band gap energy than the intrinsic layer of the top junction. This way, the bottom absorber will absorb the higher wavelengths for which the top absorber is transparent. In the case of the solar cell used in this research, the bottom junction contains an intrinsic layer of nanocrystalline silicon. The intrinsic nc-Si layer has a band gap of about $1.1eV$, which corresponds with a wavelength of about $1100nm$. Therefore, the bottom absorbing layer will mostly absorb light with wavelengths between 700 and $1100nm$.

1.2.2. Charge carrier transportation and reflection

In a thin film solar cell, the absorber layer materials have a relatively poor lateral conductivity due to the depositing techniques and growth direction. Furthermore, the metal front electrodes are kept very small in order to minimize shading losses. Therefore, a transparent conductive oxide layer (TCO) is needed to function as a transparent electrode. Furthermore, p-doped nc-SiOx, has a high refractive index compared to the glass substrate (and air) which induces a large reflectance at the air/glass interface. Adding a TCO layer, with a refractive index in between the refractive index of glass and p-doped nc-SiOx, in between the glass and the p-doped layer will reduce the primary reflectance. The reduction in reflectance will increase the amount of light that will reach the absorber layers. The ideal front contact TCO layer has a couple of properties: it lowers the reflectivity by having a refractive index between the refractive index values of air and the adjacent layer, it has high conductivity and transparency, and low contact resistance with adjacent layers.

1.2.3. Light trapping

The light that enters the solar cell will have a certain optical path length. Wavelengths for which the materials have a high absorption profile will be more likely to be absorbed than wavelengths for which the layers have a low absorption profile. When focussing on the individual layers in the solar cell in figure 1.1 from the top, where the cell is illuminated, until the second junction, the glass substrate has a band gap energy of about $3.5eV$, the front TCO materials have a band gap energy ranging between 2 and 4, the top absorber layer of about $1.8eV$ and the bottom absorber layer of about $1.1eV$. This means that the shorter wavelengths will be absorbed earlier than the longer wavelengths and most of the photons arriving at the back of the second junction will consist of the longer wavelengths. As the last n doped layer is not very reflective, almost all of the light arriving at the back of the second junction is transmitted if the solar cell does not contain any back reflector layer. Therefore, a highly reflective material like silver is added at the back. Due to the high reflectivity, the light is reflected back into the solar cell. This increases the optical path of the light within the solar cell and the amount of light that can be absorbed by the absorber layers. Another phenomenon that increases the optical path is scattering. The rougher the interfaces of the layers, the more light can be scattered throughout the solar cell, and the longer the optical path. Due to the scattering, when adding a TCO coating on top of the silver metal contact, the light will be scattered more extensively at the back, and therefore, more light will be directed back into the solar cell towards the absorber layers. Furthermore, the addition of a TCO coating on the silver back contact can shift the wavelengths towards longer wavelengths, further away from the reflectance minimum of silver. The lateral conductivity of the TCO back-reflector coating is not as important as a good lateral conductivity is already provided by the metal back contact. It is however important that the TCO material has a low parasitic absorption in the NIR.

1.3. Optical characterization of TCOs

Accurate optical characterization of TCO materials is fundamental for the optimization of TCO layers in thin film solar cells, both within the fields of experimental research and computational analysis. The complex refractive index is the starting point for the analysis of the optical response of TCO films and solar cells. Therefore, this research will be focused on the complex refractive index for the characterization of TCO materials. The complex refractive index is a relation of the real refractive index, n, and the extinction coefficient, k via $N = n + ik$. Several methods exist in determining the complex refractive index of a material.

1.3.1. Commercially used methods

Spectroscopic Ellipsometry   Spectroscopic ellipsometry (SE), measures the changes in polarization when light is reflected in the sample of interest. This change in polarization is described by the change in amplitude and the change in phase of the electromagnetic wave. To determine the complex refractive index, the change in amplitude and phase are calculated using appropriate oscillator models and fitted on the measured change in amplitude and phase. This method is used very often concerning thin films due to its high precision en sensitivity for very small films (in the orders of nanometers). However, this high precision causes the measurement to be very sensitive to surface roughness and therefore gives rise to an overestimation in the calculated k when the proper model for the fitting is not used. Therefore, the difficulty of finding the correct model for the fitting increases highly for rough surfaces.

When the surface correlation length and root-mean-square roughness features are bigger than $0.1\lambda_0$, models reach their limit. Furthermore, it is known that this method lacks sensitivity when the material of interest has a low absorption coefficient ($\alpha < 300cm^{-1}$) [8].

Spectrophotometry + SCOUT   Spectrophotometry (SP) measures the intensity of light, in terms of the light reflected by a sample of interest and the light transmitted through a sample of interest. These measurements have a lower sensitivity for thin films (in the orders of tens of nanometers), but therefore also a lower sensitivity for rough surfaces. To determine the complex refractive index, oscillator models in the commercial software SCOUT [12] are used to fit the reflectance and transmittance data measured using spectrophotometry.

1.3.2. Extinction coefficient
In figure 1.2, an example is shown for k determined both using SE and SP+SCOUT for the TCO material i-ZnO. The figure shows that the results in k for both methods are significantly different.
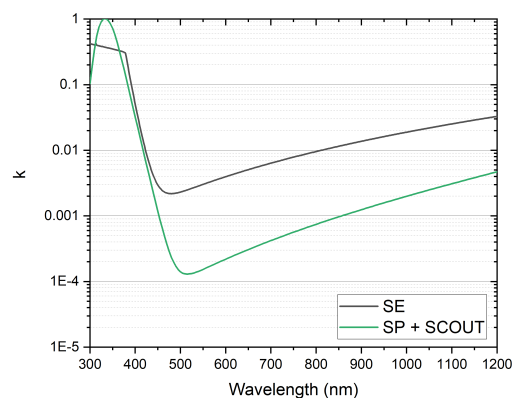
Figure 1.2

1.4. FlamingoPV
This research is part of the FlamingoPV (Flexible Lightweight Advanced Materials In Next Generation of PV) project which is a collaboration between HyET Solar and TU Delft to develop single, tandem, and triple junction cells with 12, 13, and 14% efficiencies.

1.5. Motivation, objectives, and outline
In this section, the motivation for this research will be described, as well as the objectives of the thesis and the outline of the report.

1.5.1. Motivation
Optical characterization methods   As already said, accurate optical characterization of TCO materials is fundamental for the optimization of TCO layers in thin film solar cells. It can be seen from figure 1.2, that although these SE and SP+SCOUT are often used to determine the N, in this case, they give very different results. This raises the questions: which one of the methods can be trusted? Do they both give in inaccurate results? Within this research, an attempt has been done on answering these questions. Furthermore, new methods for determining N are introduced and compared to the commonly used SE and SP+SCOUT.

Front contact TCO layer   As described in section 1.2.2, a front contact TCO layer must fulfill many functions. The TCO material aluminum-doped zinc oxide (AZO) is the standard material that FlamingoPV uses for the front contact. Furthermore, in literature, often indium-doped tin oxide (ITO) is used

as front contact layers as ITO materials provide sufficient optical and electrical properties [20], [6], [35]. But, for single films a comprise is always made between good optical and good electrical properties. It was found that when using a bi-layer instead of a single layer, the good properties of one of the materials could complement the good properties of another material [2]. Kalpoe et al. found that a combination of hydrogenated indium oxide (IOH), providing good electrical properties, and intrinsic zinc oxide (i-ZnO), providing low parasitic absorption, results in a TCO bi-layer containing both good optical properties and electrical properties that could exceed the standard single AZO and ITO layers. They found higher mobility values for the bi-layer than for the individual IOH layer [17]. As their research was experimental, they were limited in the variation in the thickness of the layer that they could explore. Furthermore, the bi-layer is not tested in the implementation of a solar cell yet. Therefore, in this research, this new bi-layer consisting of IOH, and i-ZnO, will be analyzed on its optical properties when implemented in a double junction thin film solar cell and compared with the standard used AZO, and ITO single layers to see if the bi-layer would enhance the solar cell performance compared to the single layers.

Back reflector TCO layer   As a back reflector TCO layer, FlamingoPV uses the standard AZO material. As i-ZnO is expected to have lower parasitic absorption than AZO, the effect of i-ZnO as a back reflector TCO layer on the optical response of a solar cell will be analyzed in this research. The goal will be to see if the i-ZnO layer enhances the performance of a double junction thin film solar cell compared to the AZO layer.

1.5.2. Objectives
The main objectives of this report are:

- Compare commercially used methods, spectroscopic ellipsometry, and spectrophotometry + SCOUT, for determining the complex refractive index of TCO films with new methods using spectrophotometry + GenPro4 and photothermal deflection spectroscopy + GenPro4 to build a guide for the optical characterization of TCO films.

- Compare the optical response for the design of the front contact layer in a tandem thin-film silicon solar cell for a new IOH/i-ZnO combined bi-layer with the standard AZO, and ITO single layers to find the best TCO front contact layer, and compare the optical response for the design of the back reflector in a tandem thin film solar cell for i-ZnO as back reflector TCO material with the standard AZO back reflector TCO material to find the best back reflector design.

1.5.3. Outline
A more detailed description of the theory behind transparent conductive oxides and their implementation in thin film solar cells can be found in chapter 2. Chapter 3 shows an investigation of the causes of inaccuracy for the commercially used methods SE and SP + SCOUT to determine the complex refractive index and it gives a comparison of these methods with newly introduced methods to see which one what be best for what situation. In chapter 4, an analysis on the response of double junction thin film solar cells is done to find the best front contact and back reflector design, and chapter 5 gives the main conclusions on the research done within this report.

2

Transparent Conductive Oxides

This chapter is about transparent conductive oxides, their fundamentals and properties, their implementation in thin film silicon solar cells, their characterization, and about the models used to simulate their optical behavior and response.

2.1. Fundamentals TCO materials

2.1.1. Semiconductor physics

Charge carrier generation

When a photon is absorbed in the material, its energy is used to excite an electron from initial energy E_l to higher energy E_h Only if the electron levels E_l and E_h exist such that their difference is equal to the photon energy, $E_p = hv = E_l - E_h$, the photon can be absorbed. In an ideal semiconductor, only electron energy levels below the valence band edge E_V and above the conduction band edge E_C exist. This creates a bandgap $E_G = E_C - E_V$ in which no allowed energy states exist. A photon with a smaller energy than E_G will not be absorbed and will propagate through the material without interacting [36].

When an electron excites from energy in the valence band to an energy in the conduction band, a void is created in the valance band that behaves like a particle with a positive elementary charge. This void is called a hole and together with the excited electron, an electron-hole pair is created. This is called an interband transition and indicated with E_{Inter} in figure 2.1. After some time the electron-hole pair will recombine. Recombination is the process in which the electron falls back to the initial energy level and the energy will be transferred to other electrons or holes or to lattice vibrations [36]
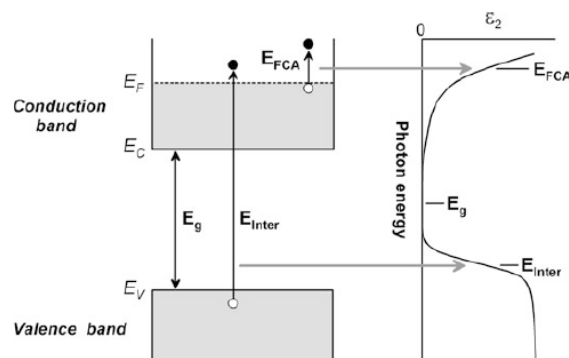
Figure 2.1: A schematic that shows the energy band with the interband and intraband (FCA) transitions. It also shows the absorption profile (imaginary dielectric function, ϵ_2 dependent on the photon energy. Figure from [8]

In most of the doped and some of the non-doped TCO layers, the free charge carrier concentration (N_e), is typically higher than $10^{18} cm^{-3}$. This is quite high and therefore, the Fermi level (E_f), is located

within the conduction band. The energy levels between the conduction band and the fermi level are occupied, so an electron from the valence band can only be excited to an energy level above the Fermi level. The interband transition is therefore much larger than the bandgap [8].
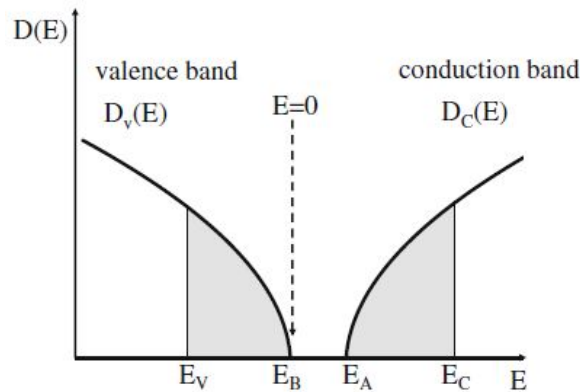
Figure 2.2: Shematic that shows the density of states for an amorphous solid. Figure from [38]

A semiconductor has a direct bandgap if an electron can be excited without changing its momentum. This is the case when the maximum of the valence band and the minimum of the conduction band exist at the same k-vector. When an electron needs a change in momentum to be able to excite, the material has an indirect bandgap. In reality, the valence and conduction bands are not flat but, due to the periodic structure of a semiconductor crystal, they depend on the k-vector that describes the momentum of an electron in the semiconductor [36].

Density of states and lattice structures

TCOs are often polycrystalline or amorphous solids. Within amorphous solids, short-range atomic arrangement orders are present, while long-range orders are not [38]. In figure 2.2 an example is shown of the density of states within the region of the valence and conduction band for an amorphous solid. An amorphous solid has multiple short-range atomic structures that each have their spatially localized band state. An electron in such a localized state has a small mobility, such that $E_C - E_V$ defines the so-called mobility gap. $E_A - E_B$ defines than the optical energy bandgap, E_{opt}, which is always smaller than the mobility bandgap [38]. While crystalline semiconductors have a "forbidden" zone where no density states exist, for amorphous solids density states can still exist between E_B and E_A. Therefore, the optical bandgap is not that well-defined [38].

2.1.2. Transparency-conductivity trade-off

Conductivity

The conductivity of the TCO layer is dependent on the charge carrier concentration and mobility according to the following relation:

$$\sigma_n = N_e e \mu \tag{2.1}$$

Here is N_e the density of electrons in the conduction band (or the hole density in the valence band), e is the electron charge ($1.6x10^{-19}C$) and μ is the mobility of the charge carriers. This relation shows that the conductivity can be increased by either increasing the concentration of charge carries or by increasing the mobility.

Transparency

The transparency of the TCOs is lower when the absorption is higher. There are three kinds of absorptions when focussing on the wavelength region from $300 - 1200nm$.

Absorption in the UV and Vis spectra   Within the Ultra-Violet and Visible spectrum, the absorption is predominantly based on interband transitions, i.e. excitation of valence electrons to the conduction band as explained earlier [38].

Absorption in the NIR   Within the near-infra-red region, the absorption is based on intraband transitions, i.e. free carrier absorption, and overtones of nucleus vibrations [38].The free carrier absorption (FCA) in the near infra-red region is dependent on the charge carrier density and mobility and described the transition from an occupied state within the conduction band to an empty state within the conduction band [8]. This is shown in figure 2.1. FCA happens when an electron scatters due to, for example, a defect. Due to the scattering, the electron loses its acceleration completely and therefore the FCA occurs. FCA increases with an increas in electrons and defects [8]. The free carrier absorption can be described using the following formula [4].

$$\alpha_f = \frac{\lambda^2 e^2 N_e}{4\pi^2 \epsilon_0 c^3 n m^{*2} \mu_{op}} \tag{2.2}$$

This formula comes from Drude model, which will be described in more detail later in this report. λ is the wavelength, ϵ_0 is the vacuum permittivity, c is the speed of light, n is the refractive index,μ_{op} is the optical mobility and m^* the effective electron mass. It can be seen that increasing the charge carrier density increases the free-carrier absorption, therefore, decreases the transmission and increasing the mobility increases the transmission.

Bandgap and plasma wavelength   In figure 2.3 the transmission, absorptance, and reflectance of an example TCO film is shown. It can be seen that the transmission is very high in the visible light and near infrared region. This is due to a low band gap wavelength, λ_g, and a high plasma wavelength, λ_p. The TCO absorbs light with a lower wavelength than the bandgap wavelength and has an absorption peak at the plasma wavelength. The plasma wavelength can be calculated by:

$$\lambda_p = 2\pi c \left(\frac{\epsilon_0 m^*}{N_e e^2} \right)^{\frac{1}{2}} \tag{2.3}$$

At this wavelength, the electron density oscillates which induces the absorption peak. Above the plasma wavelength, the plasma becomes reflective [4]. When the reflectance at the plasma absorption peak of a film is measured to be close to zero, it can be concluded that there's a homogeneous growth of the film throughout the thickness [23].

Doping
Doping could be used to increase the charge carrier density and therefore the conductivity as can be seen in formula 2.1. Formula 2.2 shows that an increase in charge carrier density also increases the free-carrier absorption in the infra-red spectrum which, in the application of a solar cell, would lead to more parasitic absorption and therefore lower the transparency.

Due to an increase in the number of free carriers, there is a shift of the optical absorption energy towards higher energies (shorter wavelengths) [23]. The effect is called the Burstein-Moss effect and is due to the Fermi level being above the conduction band gap. At room temperature, all levels until the Fermi level are occupied and therefore, free charge carriers can only be excited towards an energy level above the Fermi level. The Burstein effect is described by the following relation [23].

$$E_{opt} = E_g + \frac{h^2}{2m^*} \left(\frac{3N_e}{\pi} \right)^{\frac{2}{3}} \tag{2.4}$$

Annealing
Annealing of samples can result in an increase in grain size. A larger grain size causes a lower density of grain boundaries. Such grain boundaries behave as traps for free carriers and can be barriers to carrier transport. Therefore, an increase in grain size can cause a decreases in FCA and a decrease in grain boundary scattering, which results in an increase in mobility [19].
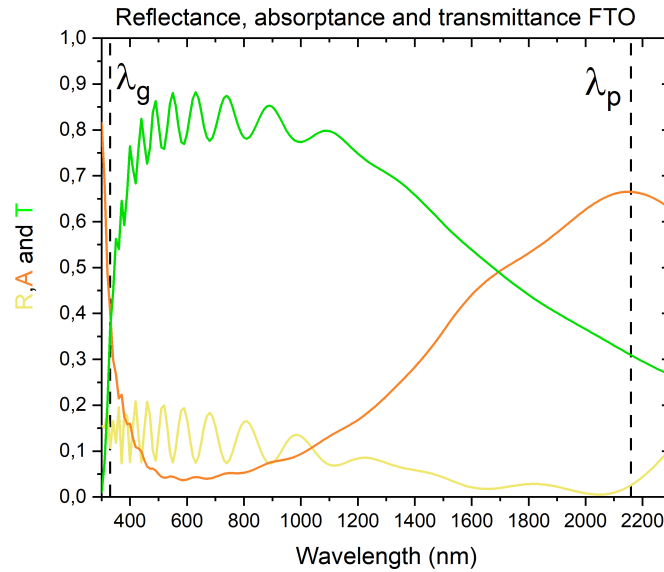
Figure 2.3: An example of the reflectance, absorptance and transmission of FTO ($SnO_2 : F$) with an indication of the bandgap wavelength, λ_g, and the plasma wavelength, λ_p.

2.2. TCO implementation in thin film solar cells

2.2.1. Thin film solar cells

Working principle solar cell

The mechanism behind the working principle of the cell is called the photovoltaic effect. In short, the photovoltaic effect is: "the generation of a potential difference at the junction of two different materials in response to electromagnetic radiation" [36]. The photovoltaic effect entails three sequential processes:

Charge carrier generation   This process is the same as explained in section 2.1.1. Except, in the case of a solar cell, the energy transferred from the photon to the electron-hole pair is preferred to be used to produce electricity, instead of getting lost in lattice vibrations [36]
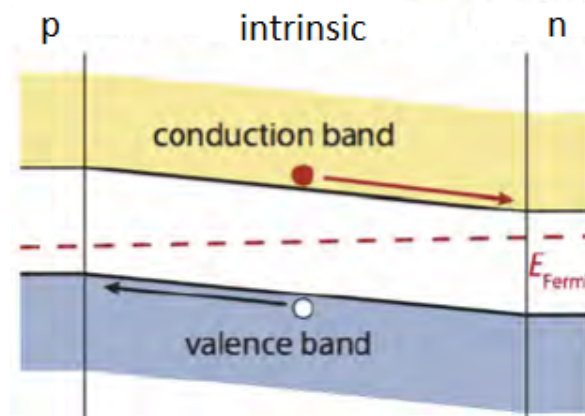
Figure 2.4: Figure adapted from [36]

Electron-hole pair separation   In the case of a thin film silicon solar cell, the separation of the electron-hole pair happens due to the characteristics of a p-i-n junction or n-i-p junction. In this research, the focus is set on a p-i-n junction. Figure 2.4 shows an example of a band diagram of a p-i-n

junction. It is shown that there's a built-in electric field created between the p- and n-doped layer and across the intrinsic layer. Because of this electric field, the photo-generated charge carrier will move through the intrinsic layer. The holes in the valence band move up the slope toward the p-layer and the electrons in the conduction band move down the slope toward the n-layer due to drift. There are also holes traveling toward the n-layer and electrons toward the p-layer due to diffusion, but in this case, the drift is the dominant transport mechanism. Within the p- and n-layers itself, the diffusion is dominant and due to the low diffusion length, both the p and n layers must be very thin to prevent recombination [36].

Charge carrier collection   The separated charge carriers are extracted from the solar cell with electrical contacts and can therefore produce a (photo-generated) current within an external circuit. After the electrons passed through the circuit, they recombine with holes again [36].

Photo current density   Using Beer-Lambert's law the photon flux, $\Phi_{ph,\lambda}(x)$ can be calculated from

$$\Phi_{ph,\lambda}(x) = \Phi^0_{ph,\lambda}exp(-\alpha(\lambda)x) \tag{2.5}$$

where α is the absorption coefficient, x the depth, and $\Phi^0_{ph,\lambda}$ the incident photon flux that can be calculated from the spectral irradiance, I, of the solar radiation using:

$$\Phi^0_{ph,\lambda} = I\frac{\lambda}{hc} \tag{2.6}$$

The total absorption in the layer is the difference between the photon flux at the surface after reflectino and the photon flux at the back of the layer, $A_{flux} = \Delta\Phi_{ph,\lambda}$. Assuming that all the absorbed photons create one electron-hole pair, the photocurrent density can be calculated from the absorbed photon flux via the following equation:

$$J_{ph} = qA_{flux} \tag{2.7}$$

where q is the elementary charge.

In the case of a double junction, a J_{ph} will be generated in both intrinsic layers. The junction that has the lowest photocurrent density will play a limiting role. Therefore, the thicknesses of the two intrinsic absorber layers need to be adjusted in order to produce a matching photocurrent density for both junctions.

2.2.2. TCO front contact layer

The front contact TCO layer has mainly the function of transmitting light so that the light can reach the absorber layers of the solar cell and transport photo-generated carriers. Therefore it needs to have a high transparency within the range of interest and a low lateral electrical resistivity (high conductivity). For a tandem thin film solar cell consisting of both amorphous silicon and nanocrystalline silicon absorber layers, the wavelength region of interest is from 300 to 1200 nm due to the absorber layers being very absorptive within this region [25]. Furthermore, the TCO material should have a refractive index in between the refractive index of the air and the adjacent layer in order to lower reflection at the front contact, it should have a low contact resistance with the adjacent layer and it should have appropriate process conditions without degrading passivation of the solar cell [11].

Performance   The performance of an individual TCO layer can be quantitated using the figure of merit, Haacke High Resolution, given by

$$\phi_H = \frac{T_{av}}{n\sqrt{R_{sh}}} \tag{2.8}$$

Here is T_{av} the average transmission over the wavelength spectrum of interest and R_{sh} is the sheet resistance of the TCO layer [5]. Cisneros et al. has found that the formula gives a high resolution when $n = 12$.

2.2.3. TCO back reflector
The longer wavelengths have a longer optical path. The more light reaches the back of the solar cell, the more light will be absorbed in the metal back contact and will therefore be not used in the conversion to electricity. To reduce the losses due to these phenomena, extra layers can be added functioning as a back-reflector. Such a back-reflector should reflect most of the light, arriving at the back of the solar cell, back into the cell so that more light can be absorbed in the absorber layers. Two aspects are important when designing such a back reflector layer:

Optical properties - Refractive index
When the incident light is normal in the interface between to media, the reflectivity can be calculated via the following Fresnel equation:

$$R_f = \left| \frac{N_2 - N_1}{N_1 + N_2} \right|^2 \tag{2.9}$$

Here is N_1, the complex refractive index of medium 1 and N_2, the complex refractive index of medium 2. $N = n + ik$, where n is the real refractive index and k is the extinction coefficient. This equation indicates that the ratio of reflected light increases when the difference between the two refractive indexes or/and the difference between the two extinction coefficients increases. So a layer functioning as a back-reflector should have a refractive index significantly different from the refractive index of the layer on top of it.

Surface morphology - Texturing
The second aspect that highly influences the reflecting functionality of the layer is surface texturing.

2.2.4. Texturing
Parameters often used to describe the features of textures are the root-mean-square surface roughness, σ_{RMS}, the surface correlation length, L_c, and the Aspect Ratio, AR. The σ_{RMS} gives an indication of the height of the texturing features, the L_c gives a measure of the distance between the texturing features, and the AR is the ratio between σ_{RMS} and L_c.

2.3. Optical characterization of TCO thin films
From classical electrodynamics, it is known that any light can be described as a superposition of electromagnetic waves. When we would like to optically characterize a certain sample, we bring this sample into interaction with electromagnetic waves (light). Due to the interaction with the sample, certain properties of the light will be modified. These modifications can give us information about the nature of the sample [38]. Assuming the electric dipole contribution is dominant within the multipole expansion of the electromagnetic field we can neglect the magnetic influence and focus on the electric field, E [38]. The polarization, P, which is the dipole moment per unit volume, has the following relation with the electric field [38].

$$P = \epsilon_0 \chi E \tag{2.10}$$

Furthermore, the electric field has a relationship with the electric displacement, D, according to the following equation.

$$D = \epsilon_0 \epsilon(\omega) E \tag{2.11}$$

Here is ω is the frequency, ϵ_0 the vacuum permittivity and $\epsilon(\omega)$ the dielectric function that is defined as:

$$\epsilon(\omega) \equiv 1 + \chi(\omega) \tag{2.12}$$

where $\chi(\omega)$ is the dielectric susceptibility. ϵ and χ are complex parameters. There are several models, discussed in the next section, that calculate the dielectric susceptibility. These models are

often used in software to characterize thin films, or to analyse their optical response.

A common parameter for describing the optical constants of a material is the complex refractive index, N, which is related to the complex dielectric function by:

$$N = \sqrt{\epsilon(\omega)} \tag{2.13}$$

This gives the following definition for the complex refractive index.

$$N \equiv n(\omega) - ik(\omega) \tag{2.14}$$

Here is n is refractive index and k the extinction coefficient. The extinction coefficient has the following relation to the absorption coefficient:

$$\alpha = \frac{4\pi k}{\lambda} \tag{2.15}$$

All these constants vary with wavelength and temperature and depend on the microstructure, composition, process conditions, etc [8].

2.3.1. Optical characterization methods

The previously described complex refractive index and absorption coefficient are both very import when characterizing TCO materials. These parameters can be determined using several methods. Some of these methods will be discussed now.

Spectroscopic Ellipsometry

The method is named ellipsometry because of the elliptic polarisation of the measured reflected light. Furthermore, the subname spectroscopic indicates the use of a continuous wavelength distribution [8]. The method consists of several steps. First, the reflectance measurement is done, then a model is constructed of the physical parameters of the TCO/substrate samples, from this the dielectric function is modeled and lastly a fitting is done in order to obtain the absorption coefficient.

SE measurement   A light with known polarization is shined onto the sample of interest and the reflected light is detected again, as shown in figure 2.5. The polarization of the reflected has become elliptic and the difference in polarization between the incident and reflected light is described by two parameters: ψ and Δ. ψ is related to the change in amplitude and Δ is related to the change in phase.

The detected light consists of both from reflections of the surface and interface between the film and substrate. the measured spectra contains peaks and valleys due to constructive and destructive interference. The thickness and refractive index of the film have an influence on the number and position of the interference features. An increase in either the thickness or refractive index, increases the number of interference features while a larger refractive index contrast Δn increases the amplitude of the oscillations [8]. Therefore, for a known substrate, the ψ oscillation amplitude can be used to estimate the refractive index of the film. If the film absorbs light, the interference will be damped or not present as then only the front reflection is detected.

Direct calculation   When calculations are done for an ideal substrate that produces a singular specular reflection from the surface, and therefore does not induce any interference effects, the dielectric function and complex refractive index of the material can be directly calculated from the SE measurement data. These functions are then called 'pseudo-dielectric functions' and can be calculated using the following formula [8].

$$\langle \epsilon \rangle = \langle N \rangle^2 = sin^2\theta \left[1 + tan^2\theta \left(\frac{1-\rho}{1+\rho} \right)^2 \right] \tag{2.16}$$

where

$$\rho = tan(\psi)^{i\Delta} \tag{2.17}$$
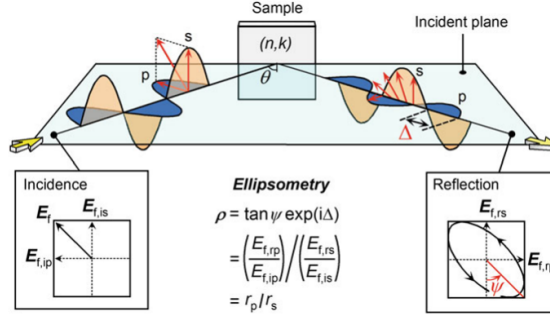
Figure 2.5: The working principle of a SE measurementFigure from [8]

The brackets, $\langle \rangle$, indicate that they are speudo functions. As the pseudo dielectric functions are directly calculated from ψ and Δ assuming a single surface reflection from an isotropic, uncoated, bulk material, these functions are only estimates for most sample measurements and can therefore only be used as an indication of the real property values[8].

Calculation via model and fitting   The fitting within the SE software is done using both Cody-Lorentz model and Drude model as will be described in the next section. The degree to which the fit agrees with the SE measurement is quantified with the Mean Squared Error (MSE). The MSE is calculated using the following formula [13].

$$MSE_{SE} = \sqrt{\frac{1}{3n-m} \sum_{i=1}^{n} [(N_{E_i} - N_{G_i})^2 + (C_{E_i} - C_{G_i})^2 + (S_{E_i} - S_{G_i})^2] \times 1000} \qquad (2.18)$$

Here is n the number of wavelengths, m, the number of fit parameters, and furthermore:
$C = \sin 2\psi \cos \Delta$,
$S = \sin 2\psi \sin \Delta$

$$(2.21)$$
$$(2.22)$$

Spectrophotometry
Two other methods for determining the complex refractive index that are analyzed in this report make use of both spectral reflectance and transmittance measurements of light. Reflectance is the ratio of reflected radiant power to the incident radiant power and can have a value between 0 and 1 due to energy conservation [9]. For the measurement, the Lambda 1050 equipment, [27] is used. This equipment consists of a UV/Vis/NIR energy source (double beam), two monochromator spectral analyzers, and some detectors which measure the reflectance or transmittance. In figure 2.6 the order of the different components during a measurement is shown. The equipment works in monochromatic mode, which means that the spectral analyzer is placed inbetween the radiation source and the sample.

The energy source consists of a tungsten-halogen lamp and a deuterium lamp. The deuterium lamp provides a continuum source from 160-380 nm, while the tungsten lamp provides a continuum source from 320-2400 nm [28]. This combination of lights provides a polychromatic source of radiation which means that it contains electromagnetic waves with each having a different wavelength. To be able to determine the reflectance and transmittance of light per wavelength, the spectrophotometer also contains a spectral analyzer. The purpose of the spectral analyzer is to convert the polychromatic source to a monochromatic source which consists of approximately one wavelength, or in reality, a narrow effective bandwidth [28]. The radiation enters the spectral analyzer through an entrance slit after it interacts with a collimating mirror or lens. This collimating mirror or lens converts the beam into a parallel beam. The parallel beam then interacts with the holographic grating that disperses the beam.
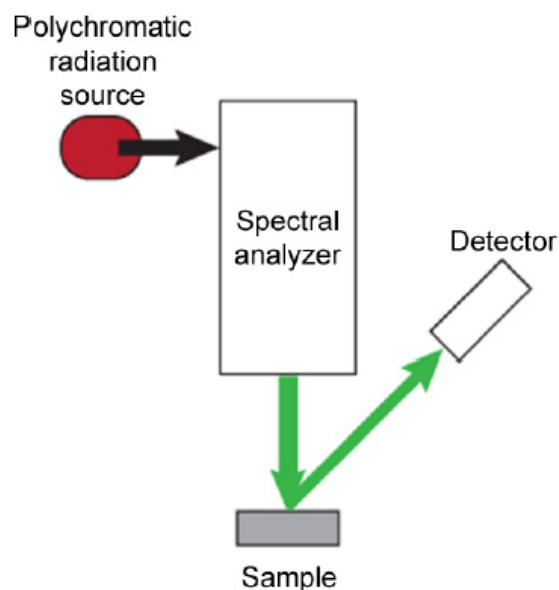
Figure 2.6: The general experimental setup of a spectrophotometric measurement. Figure from [9]

The grating is placed at a certain angle with the exit slit so that only the wavelength/effective bandwidth of interest will exit through the slit. This angle can be changed during the measurement in order the measure multiple wavelengths after each other. Narrowing the exit slit will result in a smaller effective bandwidth and better resolution, but it lowers the throughput of radiation and therefore increases the noise [28].

Photothermal Delfection Spectroscopy

PDS is a highly sensitive technique for measuring optical absorptions in thin films and coatings. In figure 2.7, the experimental setup of a PDS measurement is shown. An optically exciting beam (pump beam), in this case originating from a Dye laser, causes a change in the index of refraction of the heated region of the sample of interest due to the absorption of the beam. The absorption also causes an index-of-refraction gradient in a thin layer adjacent to the sample surface [14]. A second beam (probe beam) probes the gradient of the varying index of refraction and therefore, the deflection of the probe beam can be related to the absorption of the sample. Sensitivities of $\alpha = 10^{-6}$ are achieved for thin films and coatings [3]. Surface roughness can lead to less accurate results due to the scattering of the pump beam.
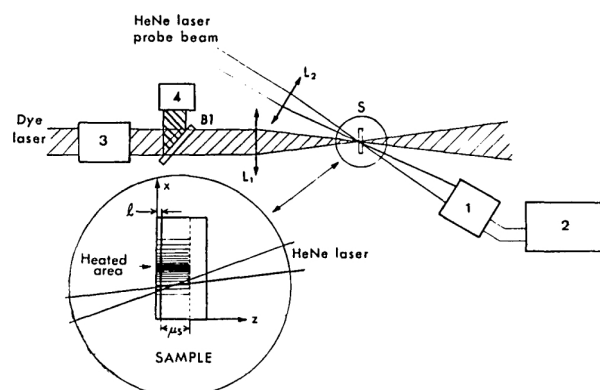
Figure 2.7: A schematic of a PDS experimental setup. 1: Position sensor, 2: lock-in amplifier, 3: modulator, 4: power meter, L1 and L2: two lenses, B1: beam splitter. Figure from [3].

2.4. Optical modeling

2.4.1. Susceptibilities

The susceptibility within equation 2.12 can be determined using different models depending on the material and light spectrum of interest.

Bound charge carriers

Both electrons and nuclei can move when excited by external electric fields, but the nuclei are much heavier compared to the electrons. The eigenfrequencies of nuclei can be expected to be about 100 times lower than the eigenfrequencies of the valence electrons. The movement of the nucleus can therefore be neglected at high frequencies. In the infrared region, where the frequencies are lower, the movements of the nuclei do have a significant influence on the optical properties of the material and therefore cannot be neglected [38]. Some of the models describing the movement of the nuclei and/or bound electrons will be discussed now.

Kim Oscillator   The Kim oscillator is an extension of the harmonic oscillator model and is designed by Kim et al. [18] to model vibrational modes. It describes a frequency-depending damping constant $\gamma(w)$ to allow a continuous shift between the Gaussian and Lorentzian models. The Susceptibility is described as:

$$\chi_{Kim} = \frac{\Omega}{\omega_0^2 - \omega^2 - i\gamma(\omega)\omega} \tag{2.23a}$$

with

$$\gamma(\omega) = \gamma_0 \exp\left(-\frac{1}{1+\sigma^2}\left(\frac{\omega-\omega_0}{\gamma_0}\right)^2\right) \tag{2.23b}$$

Here is Ω the oscillator strength, ω_0, the resonance frequency, and γ_0, the damping constant from the Harmonic oscillator model. Furthermore, σ describes if the model behaves more like the Gaussian lineshape or more like the Lorentzian lineshape. For $\sigma = 0$, the model will exclusively follow Gaussian function, and for large values, $\sigma > 5$, the model behaves exclusively like the Lorentzian function. In the near infrared where vibrational overtones can play a role, a Gaussian or Gaussian/Lorentzian behaviour model can be useful. [38]

Cody-Lorentz oscillator   The Cody-Lorentz model is developed by Ferlauto et al. [7] and describes the bound charge movements of amorphous materials. It includes an Urbach absorption term for absorptions below the bandgap, it defines the bandgap energy, the absorption at energies slightly greater than the bandgap energy, and includes the Lorentzian absorption peak [8].

As discussed before, an amorphous semiconductor can have absorptions below the energy bandgap. These absorptions can be described by the Urbach model [9]. This model assumes that within the band tail (grey regions in figure 2.2 the density of states increases linearly with energy. Within the wavelength region of the Urbach tail, the absorption coefficient decreases exponentially with frequency [38].

Within the region of photon energies slightly greater than E_g, the cody-Lorentz model assumes

$$Im\ \epsilon(E) \propto (E - E_g)^2 \tag{2.24}$$

Furthermore, the model includes the Lorentzian oscillator function that describes a resonant behaviour of the bound electron dipoles when the angular frequency of the electric field (in eq. 2.10) is near the eigenfrequency of the dipole [38].

Combined as the Cody-Lorentz oscillator, this gives the following expressions for the imaginary value of the dielectric constant [9]:

$$Im\ \epsilon(E) = \frac{E1}{A} \exp\frac{E-E_t}{E_u} \qquad 0 < E \le E_t \tag{2.25}$$

$$Im\ \epsilon(E) = G(E)L(E) = \left[\frac{(E-E_g)^2}{(E-E_g)^2 + E_p^2}\right]\left[\frac{AE_0\Gamma E}{(E^2 - E_0^2)^2\Gamma^2 E^2}\right] \qquad E > E_t \qquad (2.26)$$

where

$$E_1 = E_t G(E_t)L(E_t) \qquad (2.27)$$

In the above equations, A, E_0, and Γ originate from the Lorentzian absorption peak and define the amplitude, resonance energy, and broadening parameter respectively. E_t is the energy at which the model changes from Urbach tail transitions to band-to-band transitions and $G(E)$ and $L(E)$ define the Cody absorption behavior and the Lorentz oscillator function [38]. E_u is the exponential rate of decay.

The real value of the dielectric constant is described as:

$$Re\ \epsilon(E) = Re\ \epsilon(\infty) + \frac{2E_1}{\pi}P\int_0^{E_t}\frac{\exp\frac{(E'-E_t)}{E_u}}{E'^2 - E^2}dE' + \frac{2}{\pi}P\int_{E_t}^{\infty}\frac{E'G(E')L(E')}{E'^2 - E^2}dE' \qquad (2.28)$$

This model contains a Kramers-Kronig integration.

Tauc-Lorentz Tauc-Lorentz is developed by Jellison et al. [16] and is similar to the Cody-Lorentz oscillator. The main difference is that the Tauc-Lorentz sets the absorption below the bandgap to zero. Due to this property, this model will be less accurate for materials that have joint density states. This model is a Kramers-Kronig relation which can be added to more general models in order to make the calculations easier as it already makes some assumptions.

OJL2 interband transition This model is developed by O'Leary et al. [26] and describes interband transitions with parabolic energy bands and joint density of states that are described by tails exponentially decaying into the band gap. This model is a Kramers-Kronig relation which can be added to more general models in order to make the calculations easier as it already makes some assumptions.

Free charge carriers

Drude model The classical way of treating the free charge carries is described by the Drude model. Neglecting the movement of the atomic nuclei and therefore only considering the movement of the electrons, assuming that the motions of the electrons happen within a region much smaller than the wavelength and using Newton's equation of motion gives the following polarization [38].

$$P = -\frac{q^2 N_e E}{m}\frac{1}{\omega^2 + 2i\gamma\omega} \qquad (2.29)$$

Here is E the electric field, m is the electron mass and γ is a damping constant that considers the damping of the movement of the electrons. From equation, 2.10 can now be seen that the susceptibility is defined by [38]:

$$\chi(\omega) = -\frac{Nq^2}{\epsilon_0 m}\frac{1}{\omega^2 + 2i\gamma\omega} \qquad (2.30)$$

Here does $\frac{Nq^2}{\epsilon_0 m}$ represent the square of the plasma frequency, ω_p and filling in the susceptibility in equation 2.12 gives the dielectric function [38].

$$\epsilon(\omega) = 1 - \frac{\omega_p^2}{\omega^2 + 2i\gamma\omega} \qquad (2.31)$$

Extended Drude Model   The damping constant, γ, in equation 2.31 does not depend on frequency. However, when there's scattering at charged impurities for example, the damping of the free carriers does depend on frequency. In this case, the Drude model can be extended and the susceptibility can then be described by the following formula [12]:

$$\epsilon(\omega) = 1 - \frac{\omega_p^2}{\omega^2 + 2i\gamma(\omega)\omega} \tag{2.32}$$

with

$$\gamma(\omega) = \gamma_{low} - \frac{\gamma_{low} - \gamma_{high}}{\pi} \left(arctan\left(\frac{\omega - \gamma_{crossover}}{\gamma_{width}}\right) \frac{\pi}{2}\right) \tag{2.33}$$

Overview

Model	Phenomena	Damping	KK integration	BB abs
Kim oscillator	Bound charge	Frequency dependent	No	yes
Cody - Lorentz	Bound charge	Broadening parameter	Yes	linear tail
Tauc - Lorentz	Bound charge	Broadening parameter	Yes	zero
OJL2	Bound charge	Broadening parameter	Yes	exponential tail
Drude	FCA	Constant	No	N/A
Extended Drude	FCA	Frequency dependent	No	N/A

Table 2.1

2.4.2. Optical response simulations using GenPro4
GenPro4 is a software developed within the PVMD group to simulate the optical response of solar cells and other layered structures [31].

Flat interfaces - Flat model
When all the interfaces of the device of interest are optically flat, the optical response of the device can be modeled using the net-radiation method. Within the net-radiation method, there can be made a difference between coherent and incoherent net-radiation methods. Layers with a thickness lower than the coherence length of the incident light (about $1\mu m$ for sunlight) are treated as a coating to take into account the effects of interference. Layers with a thickness higher than the coherent length of the incident light are defined as a layer without interference. The coatings are simulated with the coherent net-radiation method, the layers with the incoherent net-radiation method [33].

Net-radiation method   By representing a solar cell as a multilayer structure as shown in figure 2.8, the overall reflectance R, transmittance T and absorptance A_i in a layer can be calculated. The subscript i indicates an individual layer or interface and each layer has a characteristic thickness d_i and complex refractive index N_i. The electromagnetic waves E indicated in figure 2.8 are complex amplitudes that are related by a set of linear equations at every interface [33]:

$$E_{ia} = \tau_{i-1}E_{(i-1)d} \tag{2.34a}$$

$$E_{ib} = r_{i>}E_{ia} + t_{i<}E_{ic} \tag{2.34b}$$

$$E_{ic} = \tau_i E_{(i+1)b} \tag{2.34c}$$

$$E_{id} = t_{i>}E_{ia} + r_{i<}E_{ic} \tag{2.34d}$$
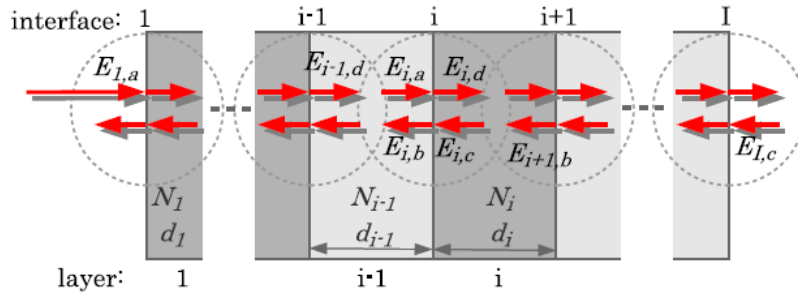
Figure 2.8: Figure from [32]

Coherent layers/coatings   The reflectance, absorptance and transmittance can be calculated with the Poynting vector, P [33].

$$R = 1 - P_1 \tag{2.35a}$$

$$A = P_i - P_{i+1} \tag{2.35b}$$

$$T = P_I \tag{2.35c}$$

where i denotes an individual interface between layers, P_1 indicates the Poyntingvector of the first interface (between air and TCO layer) and P_I the Poynting vector of the last interface. The Poynting vector can be determined from the total resultant electric field, E_i, and the complex conjugate of the magnetic field strength, H_i^* at the interface via the flowing relation.

$$P_i = \Re(E_i H_i^*) \tag{2.36}$$

Here indicates $\Re$ the real part [33].

The layer transmittance, τ_i can be described by:

$$\tau_i = \exp i\Delta_i, \tag{2.37}$$

with complex phase

$$\delta_i = \frac{2\pi N_i d_i}{\lambda} \tag{2.38}$$

These formulas describe the change in complex amplitude of the wave propagating through layer i [33].

Incoherent layers/layers   For Incoherent layers, a time-dependent phase, $\phi(t)$, should be added to the complex phase described by equation 2.38

$$\delta_i = \frac{2\pi N_i d_i}{\lambda} + \phi(t) \tag{2.39}$$

which accounts for rapidly fluctuating R and T values. Typical measurements however show the time-averaged trend of these fluctuations. Saving computational cost, these time-averaged incoherent layers R, T trends can be attained by taking the average of multiple coherent R, T calculations varying $\phi(t)$ using equidistant values of $\phi(t)$ [33].

Textured interfaces
Small textures- Wave model   When the texturing has smaller features than the wavelengths of light, wave effects like interference and diffraction need to be considered when modeling a solar cell's optic response. This modeling can be done using the scalar scattering model. The scalar scattering model developed by $Jger$ et al. assumes that the total reflectance, R_{tot} and transmittance, T_{tot}, (specular + diffused) of a slightly rough surface are equal to the reflectance, R_0, and transmittance, T_0, of a flat surface [15]. The specular reflectance, R_{spec}, and transmittance, T_{spec}, can be calculated as a fraction of T_0 and depends on the root-mean-square surface roughness of the texturing and the refractive indexes of the two media that make the interface. Then, the diffused reflectance, R_{diff}, and transmittance, T_{diff}, can be calculated with $R_{diff}(\lambda_0) = R_0(\lambda_0) - R_{spec}(\lambda_0)$ and $T_{diff}(\lambda_0) = T_0(\lambda_0) - T_{spec}(\lambda_0)$. T_{spec}, is exponentially dependent on the σ_{RMS} and the wavelength via the following 'basis' equation:

$$T_{spec}(\lambda_0) = T_0 exp\left[-\frac{(2\pi\sigma_{RMS})^2}{\lambda_0^2}(n_1 cos(\phi_1) - n_2 cos(\phi_2))^2\right]$$ (2.40)

This formula indicates that T_{spec} shows a Gaussian behavior with, σ_{RMS}, the root-mean-square roughness. n_1, and n_2, are the refractive indices of the two media, and ϕ_1, and ϕ_2, are the incident and refraction angles, respectively. This equation indicates that T_{spec} decreases with the increase in σ_{RMS}. The slope of the increase depends on λ_0. As $T_{diff}(\lambda_0) = T_0(\lambda_0) - T_{spec}(\lambda_0)$, T_{diff} increases with the increase in σ_{RMS} [15].

Large textures - Ray model   When the features of the texturing are larger than the wavelength, wave effects can be neglected. In this case, the modeling can be done using ray tracing. With ray tracing, the AID of the reflectance and transmittance of a ray with a certain incident angular interval on the interface is recorded. This is then done for multiple incident angles. [32]. In contrast to the wave model, described in the previous paragraph, the ray model calculates the total reflectance and transmittance (spectral + diffused) at a certain interface to be dependent on the texturing at that interface.

2.4.3. Beer-Lambert Law
Absorbance   The Beer-Lambert gives a relation between the absorbance, Au and the transmittance, as such:

$$Au = 2 - log_{10}(\%T)$$ (2.41)

3

Optical characterization of TCO films

As discussed in the previous chapters, accurate optical characterization of TCO materials is fundamental for the optimization of TCO layers in thin film solar cells, both within the fields of experimental research and computational analysis. The complex refractive index is the starting point for the analysis of the optical response of TCO films and solar cells. Therefore, this research will be focused on the complex refractive index for the characterization of TCO materials. Within this chapter, four different methods for determining N will be discussed and the results in N will be compared. First, one method using spectroscopic ellipsometry (SE) and two methods using spectrophotometry (SP) will be investigated on their inaccuracies, and their results in N will be compared. Then, the k values determined using photothermal deflection spectroscopy (PDS) will be compared to the SE and SP methods. All TCO samples used within this report were previously deposited within the PVMD group. The ITO, AZO, IOH and i-ZnO samples were deposited using Radio Frequency (RF) magnetron sputtering technique. Some of the samples were annealed with a saturated annealing time of 20 min and an annealing temperature varying between 130 and $250^o C$. The deposition information on the samples used within this report can be found in tables A.2 A.1, A.3 and A.4 for ITO, AZO, IOH, and i-ZnO respectively.

3.1. Methodology
In figure 3.1, the general steps taken within this chapter are visualized.
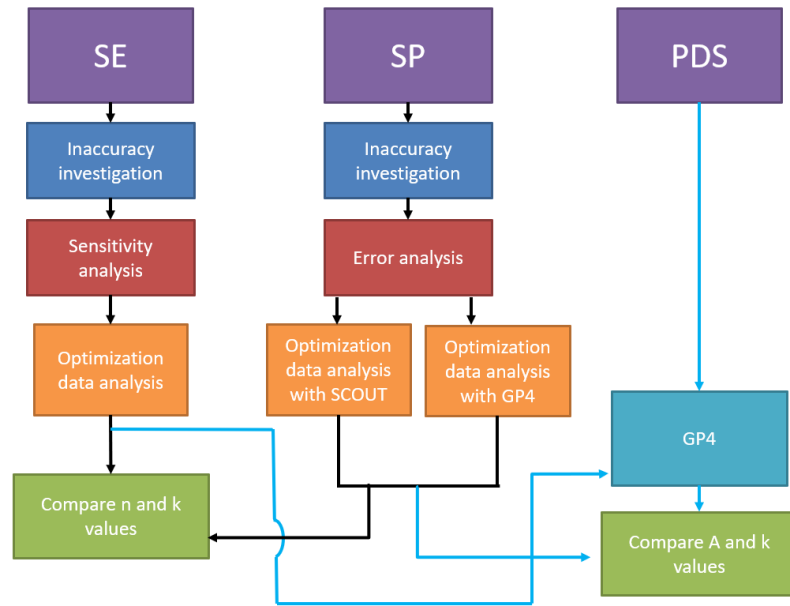
Figure 3.1: A flowchart that shows the general structure of this chapter. R: reflectance, T: transmittance, and GP4: GenPro4 [31].

3.2. Spectroscopic ellipsometry

The SE measurements were done previously within the PVMD group using the M-200D equipment from J.A. Woollam [13]. Data analysis of the SE measurements has been done using the Complete$EASE^{TM}$ software from J.A. Woollam [13].

3.2.1. Investigation into the causes of inaccuracy

The possible causes of inaccuracy using SE for the characterization of AZO, ITO, IOH, and ZnO films are investigated to get a clear overlook of when other characterization methods might be preferred. The SE data has been fitted using the Cody-Lorentz and Drude model for a wavelength range of $300 - 1200nm$. SE provides an root-mean-squared error (MSE) that indicates how well the fit agrees with the measured data. Formula 2.18 shows how the MSE is calculated. The information from the fittings is used to see if the MSE fitting value is related to film thickness, surface roughness, deposition time, and the power used during film deposition. Furthermore, to get a better idea of the inaccuracy for low k values, a sensitivity analysis is done.

The relation of the MSE with certain film structure parameters

To get a better idea of what causes high MSE values, the MSE values of all deposited samples are compared with their (via SE calculated) thickness and roughness and the deposition time, t_{dep} and power P. already deposited samples of AZO, ITO, IOH, and i-ZnO, are are divided into stacks of samples looking at the single parameters varied during deposition. In table 3.1, the single parameter that carries is specified for each stack. For example, for AZO, stack A, B, and C, contain samples that have to same deposition parameters except for the deposition time. Stack D consists of samples having the same deposition parameters except for the deposition power. This way, the relation between the MSE and the deposition time and deposition power can be clearly analyzed for every material. The graphs containing the relations between thickness and deposition, thickness and deposition power, MSE and thickness, roughness and deposition time, roughness and deposition power and roughness and MSE can be found in figures 3.2, 3.3, 3.4 and 3.7 for ITO, AZO, IOH, and i-ZnO respectively.

The maximum errors, provided by SE, regarding the thickness, σ_d, and roughness, σ_{SR}, calculation are specified for certain value ranges for every material and can be found in table 3.2. The errors are not added to the graphs as this would make them too cluttered. Furthermore, some errors are too small to be seen in the graph.

stack	A	B	C	D	I
ITO	t_{dep}	t_{dep}	-	t_{dep}	-
AZO	t_{dep}	t_{dep}	t_{dep}	P	-
IOH	P	P	P	P	t_{dep}
i-ZnO	P	P	t_{dep}	P	-

Table 3.1: The information on the stack labels used in this section and the single parameter that is varied in the stack for AZO, ITO, IOH, and i-ZnO. t_{dep}: deposition time, P: deposition power.

Material	d range (nm)	$\sigma_d (nm)$	SR range (nm)	$\sigma_{SR}(nm)$
	0 - 150	0.08	0-15	0.03
ITO	200 - 400	0.7	20- 45	0.17
	400 - 600	1.6	-	-
AZO	0-900	2.6	0-6	0.08
	-	-	6-13	0.48
IOH	0-120	0.07	-1 - 5	0.3
	120 - 300	0.5	-	-
i-ZnO	0-1200	0.7	6-10	0.2
	-	-	10-22	0.14

Table 3.2: The maximum found errors for certain ranges of thickness, d, and surface roughnes, SR, calculated by SE for ITO, AZO, IOH, and i-ZnO.

ITO In figure 3.2a, it can be seen that for ITO samples the thickness of the sample increases linearly with the increase of deposition time. This is shown for stacks A, B, and D where the deposition time is the only varying deposition parameter. It can also be seen that for stack A and B, the MSE increases linearly with thickness and therefore also linearly with deposition time. The reason for the increase in MSE with thickness is due to the increase in interference fringes in the SE measurement data. The increase in interference fringes makes it more difficult for the model to exactly fit the measurement. This is also the reason why for stack D, this relation between the MSE and thickness is not found. The thicknesses of the samples from stack D are too small for interference fringes to have any influence.
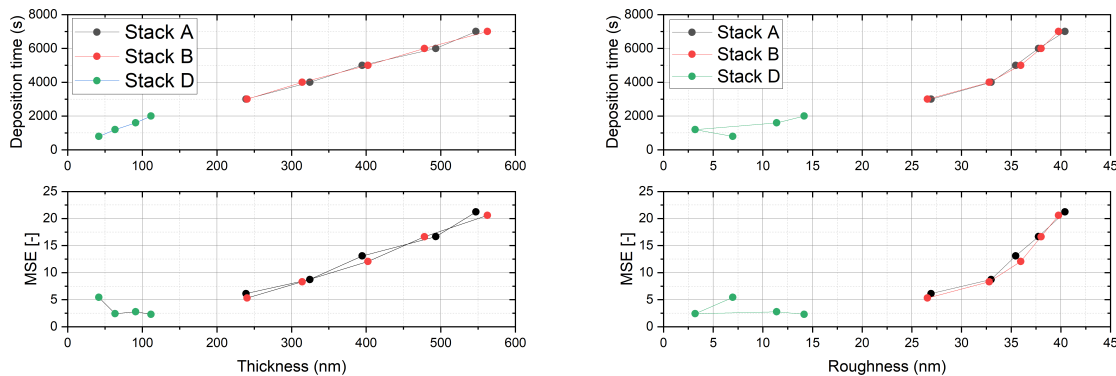
(a) Deposition time - thickness - MSE
(b) Deposition time - roughness - MSE

Figure 3.2: (a): a graph that shows the relation between the deposition time and the ITO layer thickness, and between the MSE and the ITO layer thickness, for three different stacks in which the samples only very in deposition time. (b): a graph that shows the relation between the deposition time and the ITO surface roughness, and between the MSE and the ITO layer surface roughness, for three different stacks in which the samples only vary in deposition time.

The relation between roughness and thickness can be seen in figure 3.2b. Stack A and B show an increase in roughness with an increase in deposition time. Below a deposition time of $4000s$ this is a steep increase, but from $4000s$ and longer, the roughness increases more slowly. As explained in the

previous chapter, the Bruggeman model for surface roughness can accurately correct for the roughness until a roughness with features bigger than 0.1 times the wavelength. As we are fitting for a wavelength range starting at $300nm$, it is expected that roughness with features around $30nm$ and higher will have more influence on the fitting and therefore cause a higher MSE. We can see in the figure where the MSE is plotted against the roughness, that this is indeed the case. For stacks A and B we can see a much steeper increase in MSE from about $33nm$ and higher compared to lower roughness values. For stack D we can see that there's not really a trend between the MSE and roughness. This makes sense as the Bruggeman model is capable of modeling the surface roughness accurately.

AZO   Figure 3.3a shows a linear relation between thickness and deposition time for stacks A, B, and C. It also shows a linear relation between thickness and deposition power, for stack D. The graph with MSE against thickness shows that there does not exist a linear relationship between the MSE and the film thickness. Between a thickness range of about 50 and $300nm$, as expected, an increase in MSE is found with an increase in thickness. It is interesting though, that the MSE values around $250-300nm$ are quite high, and for higher thicknesses around $400-650nm$, the MSE seems to decrease again significantly. Stack D shows a significant increase in MSE again for thicknesses higher than $600nm$.

As we can see in figure 3.3b, the surface roughness does not really show a common trend with both deposition time and MSE. Furthermore, the roughness values stay relatively low (smaller than $13nm$). Therefore, the lack of relation between MSE and roughness is expected.

(a) Deposition time and power - thickness - MSE   (b) Deposition time and power - roughness - MSE
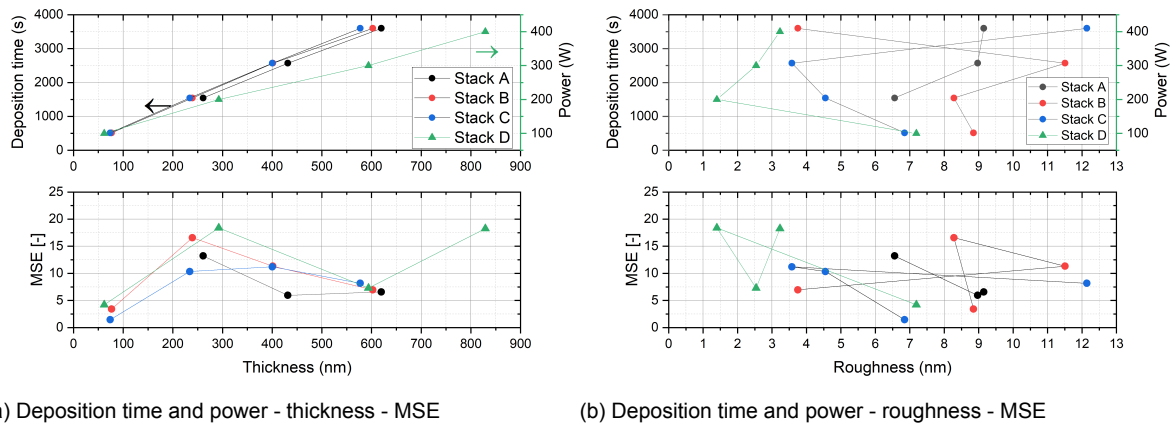
Figure 3.3: (a): a graph that shows the relation between the deposition time and the AZO layer thickness, the deposition power and the AZO layer thickness, and between the MSE and the ITO layer thickness, for three different stacks. (b): a graph that shows the relation between the deposition time and the AZO surface roughness, the deposition power and the AZO surface roughness, and between the MSE and the ITO layer surface roughness, for three different stacks.

As AZO does not show any big roughnesses, the high MSE peak around film thickness of about $250-300nm$ can not be explained by the surface roughness. When fitting the SE data for a certain sample, the fitting values of a previously fitted sample with similar properties and characteristics are used as a starting point. Therefore, often the previous fitting from samples consisting of the same material and similar film thickness is used. Therefore, it could be that the high MSE peak is a result of a systematic error within the fitting.

IOH   In figure 3.4a, it can be seen that the IOH samples show a linear relationship between the thickness and deposition time and between the thickness and deposition power. The graph with the MSE against the thickness shows that there is an increase in MSE with an increase in thickness. The relation is not found to be linear, but this could also be due to the high data resolution and the relatively small thickness range that is analyzed.

Figure 3.4b shows a lack of relation between both the deposition time and surface roughness and the MSE values and surface roughness. Furthermore, the surface roughness is found the be very low in general.
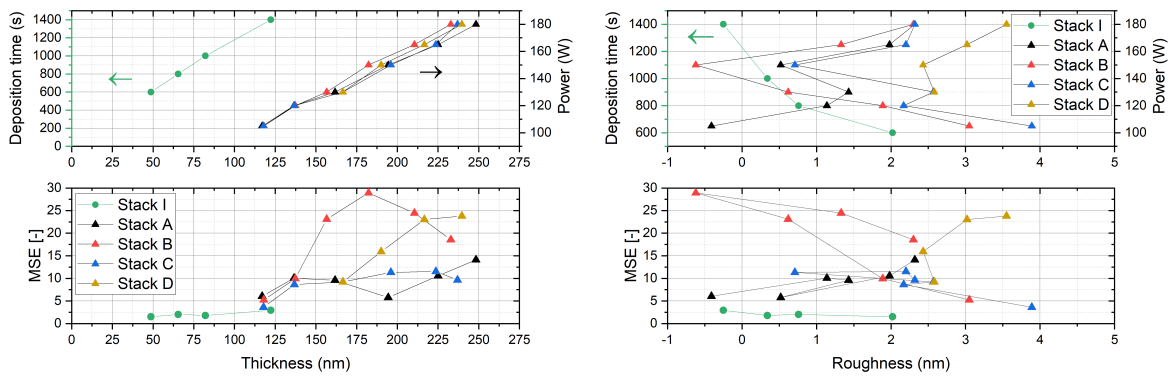
(a) Deposition time and power - thickness - MSE   (b) Deposition time and power - roughness - MSE

Figure 3.4: (a): a graph that shows the relation between the deposition time and the IOH layer thickness, the deposition power and the IOH layer thickness, and between the MSE and the IOH layer thickness, for three different stacks. (b): a graph that shows the relation between the deposition time and the IOH surface roughness, the deposition power and the IOH surface roughness, and between the MSE and the IOH layer surface roughness, for three different stacks.

i-ZnO   For i-ZnO, it can be seen in figure 3.5a that thickness most likely has a linear relation with the deposition power. For the deposition time, a linear relation is not found, but this could be due to a random error of the sample deposited with a time of $2000s$. The MSE shows, for all stacks, an increase with increasing thickness.
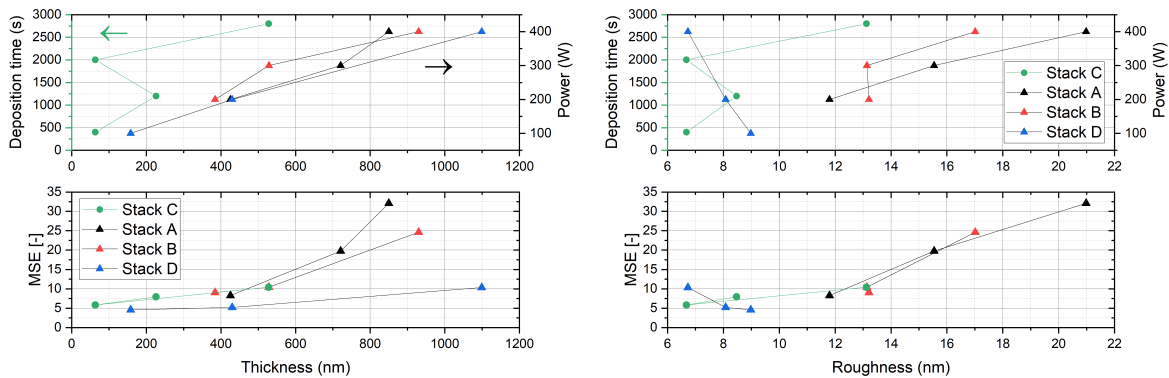
(a) Deposition time and power - thickness - MSE   (b) Deposition time and power - roughness - MSE

Figure 3.5: (a): a graph that shows the relation between the deposition time and the i-ZnO layer thickness, the deposition power and the i-ZnO layer thickness, and between the MSE and the i-ZnO layer thickness, for three different stacks. (b): a graph that shows the relation between the deposition time and the i-ZnO surface roughness, the deposition power and the i-ZnO surface roughness, and between the MSE and the i-ZnO layer surface roughness, for three different stacks.

In figure 3.5b, it can be seen that for 2 out of 3 stacks, the surface roughness (SR) increases with deposition time. These also show an increase in MSE with an increase in roughness. Stack C also shows an increase in MSE with an increase in roughness. What is interesting to see, looking at the highest deposition time data point for stacks A, B, and D, is that the data point of stack A has the lowest thickness, but the highest MSE. If we compare this with the roughness then that point has the highest roughness of the three. The other way around, the data point of stack D has the highest thickness, the lowest MSE, and the lowest roughness. So, it can be concluded from this data that even though the roughness is below 0.1λ, the roughness still has an influence on the MSE, even a greater influence than the thickness. It can be stated that the thickness still has an influence, because, for stack D, the roughness decreases with deposition time, but still has an increase in MSE with an increase in thickness. It seems that for roughness around $13nm$ or lower, the influence is less significant. This can

be seen when looking at the difference in SR and MSE for stack C

Sensitivity analysis

In literature it is stated that SE has a limited sensitivity for weak absorbing regions ($\alpha < 500cm^{-1}$) [8]. With 'sensitivity', here is it meant, how much the measurement data changes with the change in α. To get a more precise insight into the sensitivity of SE with regard to the extinction coefficient, analysis is done on the sensitivity of the Δ and ψ SE measurement data regarding low extinction coefficient values. For this, the measurement error in Δ en ψ is compared with the change in Δ en ψ due to a change in k.

The sensitivity of the SE measurement for low extinction coefficient values can be investigated using the direct conversion formula, equation 2.16. This equation can be rewritten as:

$$tan(\psi)e^{i\Delta} = \rho = \frac{2}{1 + \sqrt{\frac{1}{tan^2\theta}\left(\frac{N^2}{sin^2\theta} - 1\right)}} - 1 \tag{3.1}$$

Both the left and right sides of this equation are complex and if we say that the right side of the equation is equal to a complex number $a + ib$ that can be calculated with known values for N and θ, then the values for ψ and Δ can be calculated using the following two equations.

$$a = tan(\psi)cos(\Delta) \tag{3.2a}$$

and

$$b = tan(\psi)sin(\Delta) \tag{3.2b}$$

In order to check if the calculation is correct, the ψ and Δ have been calculated for two N values far from the low sensitivity regime and four N values within the low sensitivity regime, and these ψ and Δ are compared with fitted data. To compare, data with a low-fitting MSE from an i-ZnO sample has been used. The initial angle is set at 55° and the n and k values are taken from the fitted sample values. The n and k values regarding certain wavelengths that are used are shown in figure 3.6a with data points on the n and k trend of the i-ZnO sample. If we keep in mind, the α sensitivity limit of $500cm^{-1}$ for literature, which indicates a k limit of about 0.002 at $\lambda = 500nm$, it can be assumed that the sample has a weak absorption profile for most of the visible en NIR spectrum. The calculated ψ and Δ for the selected n and k values are plotted as square data points next to the measured and fitted ψ and Δ of sample ZnO24. This is shown in figure 3.6b. It can be seen that the calculated ψ and Δ follow a trend that's somewhat the average of the measured data. This is expected, as equation 2.16 doesn't take interference into account and therefore doesn't show any fringes, in contrast to the measured data. As the calculated data does show an expected trend compared to the measured data, it can be concluded that the calculation has been done correctly and that equation 3.1 is sufficient to use for a sensitivity analysis.

ψ and Δ have been calculated using equation 3.1 with an incident angle of 55°, a constant value $n = 2$ and a set of values for the extinction coefficient ranging from $1 * 10^{-5}$ until 0.6 (step size of $1 * 10^{-5}$) as most samples used in this research lay within this range. The results of this calculation are shown in figure 3.7a. Δ seems to be varying very little for k values lower than 0.01 and ψ seems to be varying very little below $k = 0.1$. In general, Δ does have a higher sensitivity to k than ψ. To give more meaning to these results, errors, $\sigma_\Delta = 0.1$ and $\sigma_\psi = 0.02$, have been taken into account for Δ and ψ respectively. These error values are chosen as, according to J.A. Woollam, the developer and manufacturer of the equipment: "Typical ellipsometers can accurately measure ψ and Δ to better than 0.02° and 0.1° respectively" .... Furthermore, in the software manual, it is stated that the N, C, and S values from equations 2.3.1 have a typical measuring precision and accuracy of about 0.001. Using equations 2.3.1 to calculate the error in N, C, and S using $\sigma_\Delta = 0.1$ and $\sigma_\psi = 0.02$ for different values of Δ and ψ, indeed error values of about 0.001 are obtained for N, C and S. Figure 3.7b shows ψ and Δ zoomed in together with the error bars for a low valued k region where all error bars overlap. As the error bars overlap, this means that the change in Δ and ψ within this region lies within the error marge of Δ and ψ. Therefore, it can be stated that the sensitivity of Δ and ψ regarding k within these regions is too low to get an accurate measurement, and measurements done for k values within this region could all get the same result. We can't know from the results what is actually measured within this region.
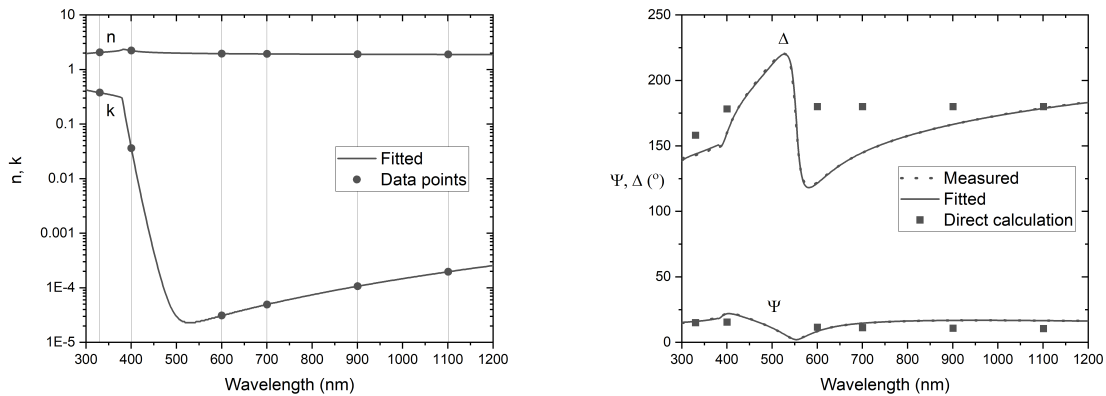
(a)   (b)

Figure 3.6: (a): graph of the example n and k fitted using SE for an i-ZnO sample, shown with the solid lines, and the data points of these n and k trends used for the Δ and ψ calculation, shown with round data points. (b): the Δ and ψ from an i-ZnO sample measured using SE (dashed lines), fitted using SE models (solid lines), and calculated using the direct conversion formula (square data points).

For the remaining plots in this section, the low sensitivity area of ψ has been indicated with a light grey color, and the low sensitivity of Δ has been indicated with a dark grey color.
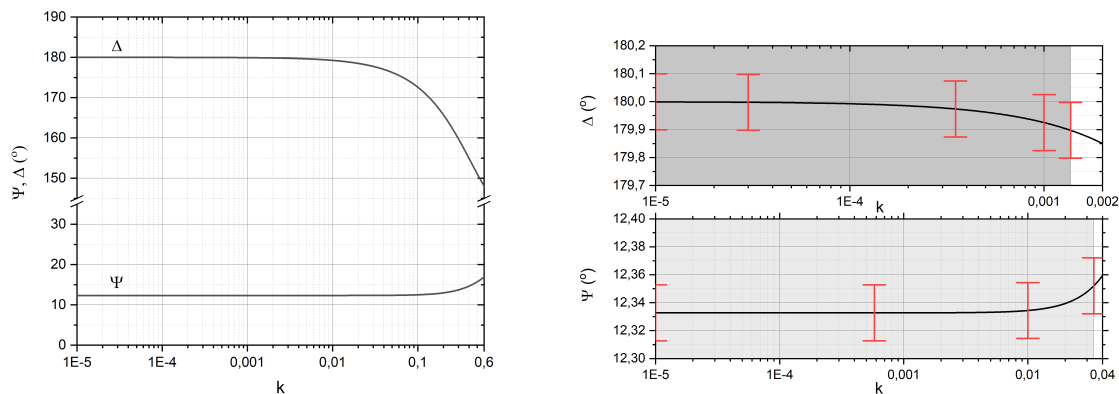
(a)   (b)

Figure 3.7: (a): a graph showing the via the direct conversion formula calculated Δ and ψ for a range of k values. (b): a graph showing the via the direct conversion formula calculated Δ and ψ for a smaller range of k values and error bars containing σ_Δ and σ_ψ.

3.2.2. The influence of roughness correction

For all SE results retrieved till now, the fitting included automatic roughness correction. In this section, the effect on the fitting results of this automatic roughness correction will be investigated to see how big the influence of the roughness is for certain samples. The results of the n and k values for certain samples can be seen in figure 3.8 and the MSE and fitting results can be found in table 3.3. It can be seen that the refractive index is barely influenced by the surface roughness correction.

AZO   Looking at figure 3.8a, it can be seen that, although AZO18 changes less in MSE, the change in extinction coefficient is bigger compared to AZO12. Furthermore, the calculated roughness of AZO12

Material	Label	MSE (no SR)	MSE (SR)	d (nm) (SR)	SR
AZO	AZO12	43.5	8.2	580	12.1
	AZO18	12.4	5.4	200	3.5
ITO	ito-4	96.4	11.3	360	35.4
	ITO20	24.3	1.8	110	11.2
IOH	IOH27	2.8	2.7	110	-0.2
	IOH 1(200)	13.4	3.6	120	3.9
i-ZnO	ZnO1	84.9	32.1	850	21.0
	ZnO7	50.8	9.1	380	13.2

Table 3.3: The AZO, ITO, IOH, and i-ZnO samples used for the analysis of the influence of surface roughness together with the MSE values for fitting results without roughness correction, the MSE values for fitting results with roughness correction, the thickness of the TCO layers calculated using SE and the surface roughness, SR, calculated by SE.

is bigger compared to AZO18, therefore, a greater influence would be expected. It must be noticed, though, that AZO12 is calculated to be deep within the low sensitivity zone. Therefore, a good explanation for the smaller change in k could be due to a big error in k. In general, the extinction coefficient values calculated using the Bruggeman model are lower than the ones calculated without the model. This is as expected [8].

(a) AZO

(b) ITO

(c) IOH

(d) i-ZnO
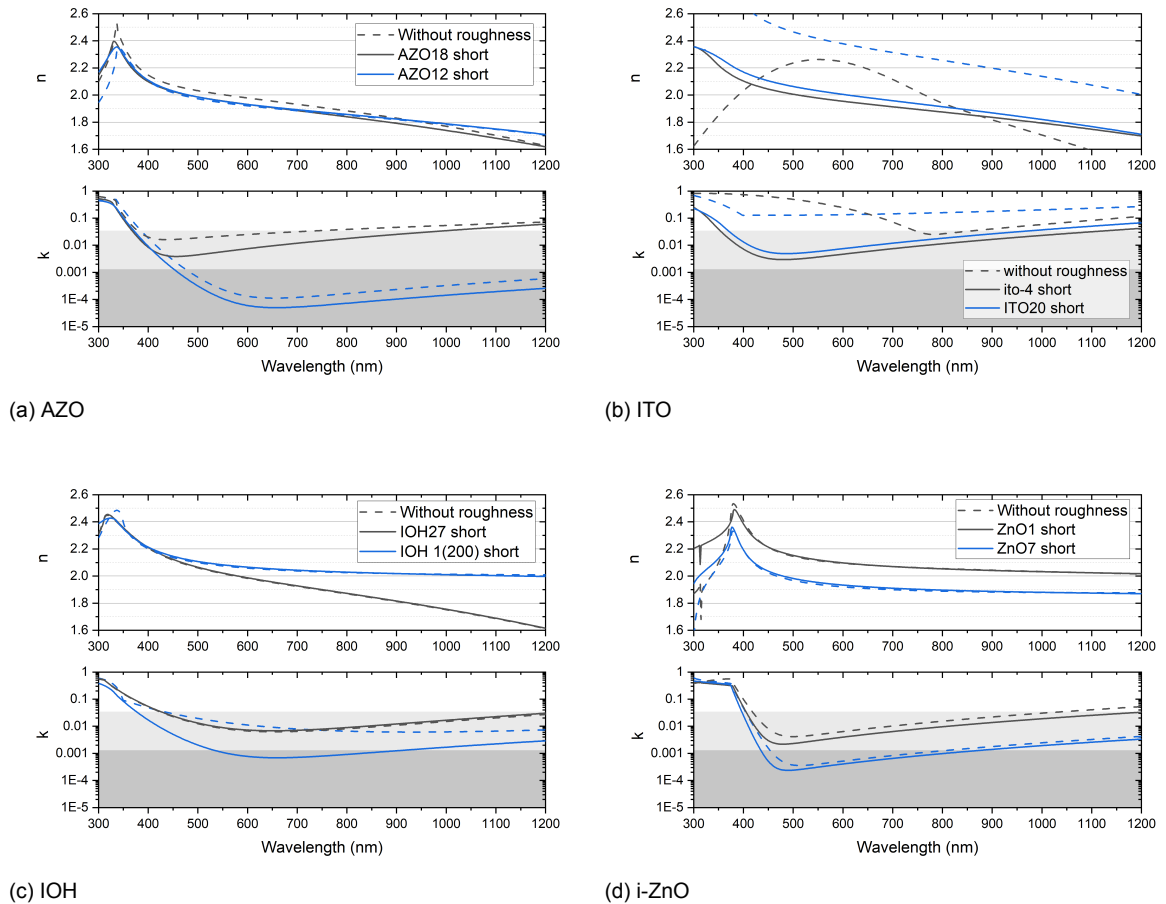
Figure 3.8: (a): graph showing the n and k values determined by SE for samples AZO18 and AZO12 for a fitting with and a fitting without the use of SR correction. (b): graph showing the n and k values determined by SE for samples ito-4 and ITO20 for a fitting with and a fitting without the use of SR correction. (c): graph showing the n and k values determined by SE for samples IOH27 and IOH 1(200) for a fitting with and a fitting without the use of SR correction. (d): graph showing the n and k values determined by SE for samples ZnO1 and ZnO7 for a fitting with and a fitting without the use of SR correction.

ITO For ito-4, the SR is calculated to be very high. This can also be seen in the change in MSE values and the change in extinction coefficient. Not only the level of the trend changes but also the trend itself. The trend shown calculated without roughness correction looks very unnatural for a TCO. ITO20 is changed less in trend, but still changed a lot in height.

IOH The k trend of IOH27 does not change significantly. This minimal change os also found within the MSE values and, the SR is very low. For IOH 1(200), a significant change in both k and MSE can be seen.

i-ZnO For both ZnO1 and ZnO7, the change in MSE is very big, but the change in extinction coefficient does not really present this big change. It is known that i-ZnO has a very low k for energies lower than the band gap. So this low change in k could again be due to low sensitivity.

Comparison When comparing the four graphs, it can be stated that the extinction coefficient is highly affected by roughness values starting from $3nm$, except when either the k trend is calculated to be deep in the low sensitivity area (AZO12), or, when the k is expected to be very low (i-ZnO). These small changes could be due to big errors in k or it could just be that the roughness has less effect on less absorbing materials. In general, the extinction coefficient is lowered when roughness is taken into account.

3.2.3. The influence of fitting wavelength range

All SE results till now were retrieved by doing a fitting for the wavelength range of $300 - 1200nm$. In this section, the effect of fitting for a larger wavelength range on the MSE value and complex refractive index is investigated. The results for a fitting of the range $300 - 1200nm$ are compared with the results for a fitting of the range $190 - 1690nm$. All SE fittings for the wavelength range of $190 - 1690nm$ used in this research were done previously within the PVMD group.

Fitting for a larger wavelength range means that there is more information available for the model to base the calculations on. This could lead to more accurate results. But on the other hand, a broader spectrum also creates a larger influence of possible inhomogeneities in the film on the SE measurement and can therefore create more complex data and a less agreeing fit. This could lead to less accurate results. The fitting MSE is not normalized, as shown in equation 2.18, but as the observables have a range that is always between -1 and 1 (very small), normalization is not needed. Therefore, it makes sense to compare the MSE values for very different fitting specifications. It can therefore also always be assumed that a lower MSE indicates a better fit-data agreement. However, when comparing MSE values for two different wavelength regions, it is not known how well the broad-region fit agrees with the data looking at the short region compared to the short-region fit itself.

Material/sample		MSE_{broad}	MSE_{short}	$d_{short}(nm)$	$SR_{short}(nm)$	$E_{g,short}(eV)$
ZnO	ZnO1	46.069	32.08	850	20.98	2.875
	ZnO2	30.121	19.74	720.98	15.54	2.884
	ZnO13	16.999	14.01	138.27	6.97	4.026
AZO	AZO3	26.368	5.95	431.43	8.97	3.404
	AZO12	35.029	8.17	577.27	12.14	3.472
	AZO19	19.758	16.553	254.56	2.74	2.298
ITO	6kPA	21.745	16.65	478.09	38.01	4.037
	ito-2	14.567	11.39	364.90	35.43	4.026
	7kA	25.403	21.223	547.06	40.42	4.026
	3(180)	35.58	23.12	156.63	0.62	3.782
IOH	IOH 8	23.11	20.58	113.02	-0.54	3.527
	IOH 42	22.659	17.29	211.38	0.65	7.225

Table 3.4: The MSE values, MSE_{broad}, of some samples for a fitting done for a broad wavelength range from 200 until $1600nm$. Furthermore, the results for a short wavelength range SE fitting from $300 - 1200nm$. MSE_{short}, d_{short}, SR_{short}, $E_{g,short}$: the short wavelength fitting results for the MSE, the TCO layer thickness, the surface roughness, and the energy band gap.

Table 3.4 shows the MSE values of the short and broad-range fittings from several samples together with the calculated film thickness, roughness, and energy bandgap regarding the short-range fitting. Figure 3.9 shows the n and k values of the broad and short range of those samples. It can be seen clearly that for all four TCO materials, the refractive index does not change that significantly. As we also saw this in the previous section, this could indicate that SE is a robust method for determining the refractive index and increases the trustworthiness of the characterization method with respect to the refractive index. The extinction coefficient on the other hand, does changes significantly. Although, how much, depends on the material.

(a) AZO

(b) ITO

(c) IOH
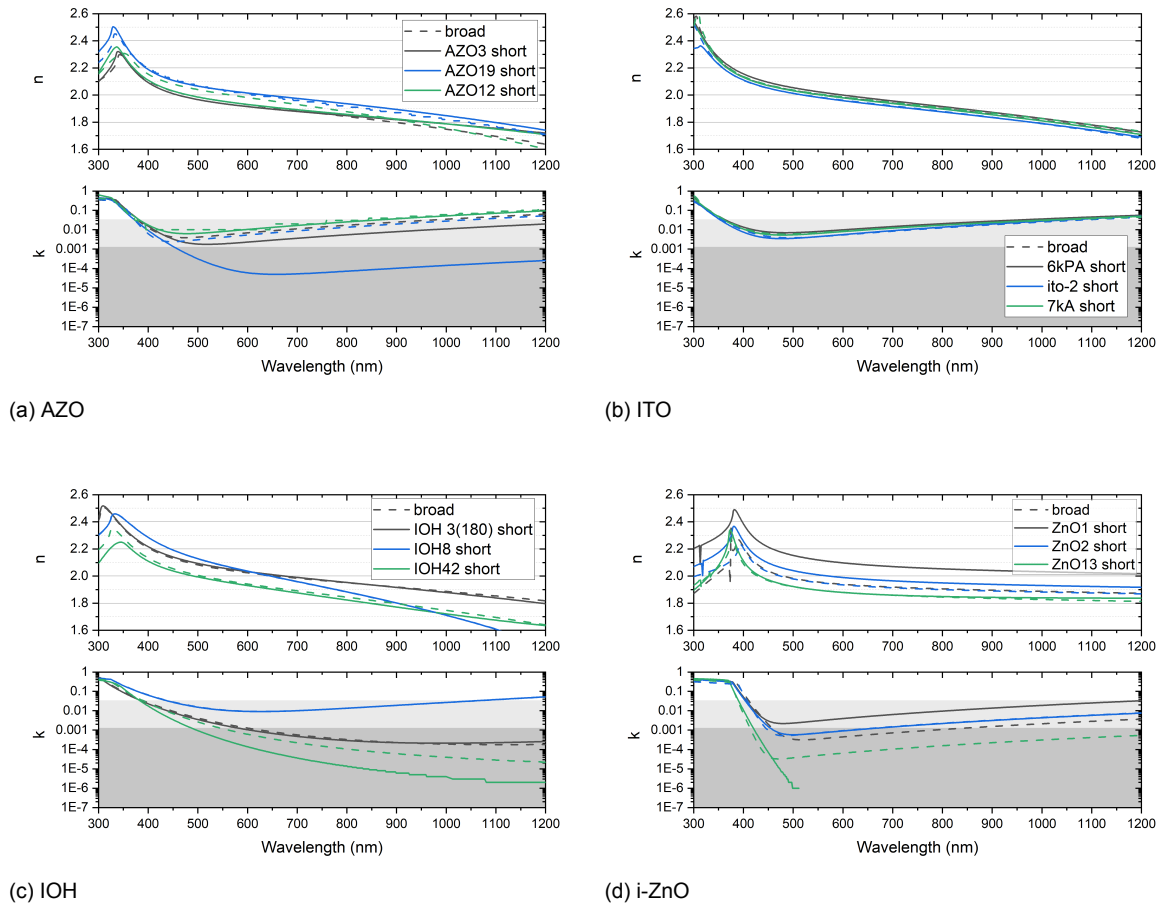
(d) i-ZnO

Figure 3.9: (a),(b),(c),(d): the n and k values determined using SE for some samples using both the broad-range fitting and short-range fitting for, AZO, ITO, IOH, and i-ZnO, respectively.

AZO For aluminium-doped zinc oxide we can see that samples AZO3 and AZO12 show a significantly lower extinction coefficient trend when fitted with the shorter range. Especially, for AZO12 there is a large difference in the range of two orders of magnitude from about 700 to $1200nm$. The k trend of AZO19 has not changed that much, except that the trend for the broad fitting shows a saw behavior. The MSE value of sample 12 also changes the most compared to the other two AZO samples. The MSE value for the short-range fitting is much lower than for the broad-range fitting.

ITO The differences between the k trends for indium-doped tin oxide are not that significant. The k trends are mostly within the same order of magnitude.

IOH One of the three samples of IOH shows a significantly lower k trend for the short-range fitting. The other two don't show a significant change in k.

i-ZnO Intrinsic zinc oxide shows for one out of two samples a higher k trend for the short-range fitting compared to the broad fitting. Sample ZnO2 does not show a significant change and for ZnO13, the short k trend has undefined values from about $510nm$. These undefined values are probably due to the sensitivity of the SE measurement.

From these graphs, it is difficult to conclude which one of the fitting ranges gives more accurate results, so the results of both ranges are compared with PDS measurements in section 3.7.

3.3. Spectrophotometry

Two other methods for determining the n, k values of the TCO films use reflectance and transmittance measurements. These reflectance and transmittance measurements are done previously by the PVMD research group of Delft University of Technology using the spectrophotometer, Lambda 1050 UV/Vis/NIR, from Perkin Elmer [27]. All measurements are done for a certain orientation of the sample shown in figure 3.10. For the transmittance measurement the orientation is not that important, the sample will transmit the same amount of light independent on the side of illumination. For the reflectance, it is important that all reflectance measurements are done on the TCO layer side of the sample. If the measurement were to be done on the glass side, the reflectance measurement is highly influenced by the light absorption in the glass.
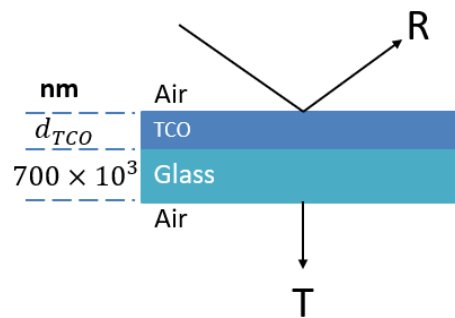
Figure 3.10: Schematic of the TCO layer on top of the glass substrate indicating the orientation of the sample for the spectrophotometric R, and T measurements, and the thicknesses of the layers.

In figures 3.11a, 3.11b and 3.11c, the measured reflectance and transmittance of an AZO, ITO, and IOH sample are shown, respectively. The law of conservation of energy states 1 = A+R+T, where A is absorptance, R is reflectance, T is transmittance. In the figures, the reflectance is presented as $1 - R$ Therefore, the absorptance, which is the difference between the $1 - R$ and T line, can also easily be seen.

3.3.1. Investigation into the causes of inaccuracy

Negative absorptance

It can be seen that for all samples, there are wavelength regions where the $1 - R$ line is lower than the T, in other words, there are regions where the absorptance has negative values. As it is known that TCO materials, in reality, do not emit any light, it can be stated that these negative values are due to some measurement error. What has to be kept in mind, is that, as explained in the previous chapter, the accuracy of the R, T depends a lot on the actions taken by the person measuring. So it could be that for example, for some of the R, T data available, the calibration of the equipment has not been done properly. This could exaggerate the negative absorption values. Three different reasons for these negative absorptance values occurring can be acknowledged by analyzing the R, T data:

1. Low absorptance region When the absorptance of the film is lower than the error of the reflectance and transmittance measurement combined, the chance is very big that the absorptance calculated from the reflectance and transmittance will be less than zero. This can happen especially in the region where there is almost no interband absorption anymore, so above bandgap wavelength, and

(a) AZO

(b) ITO

(c) IOH

(d) IOH smooth R
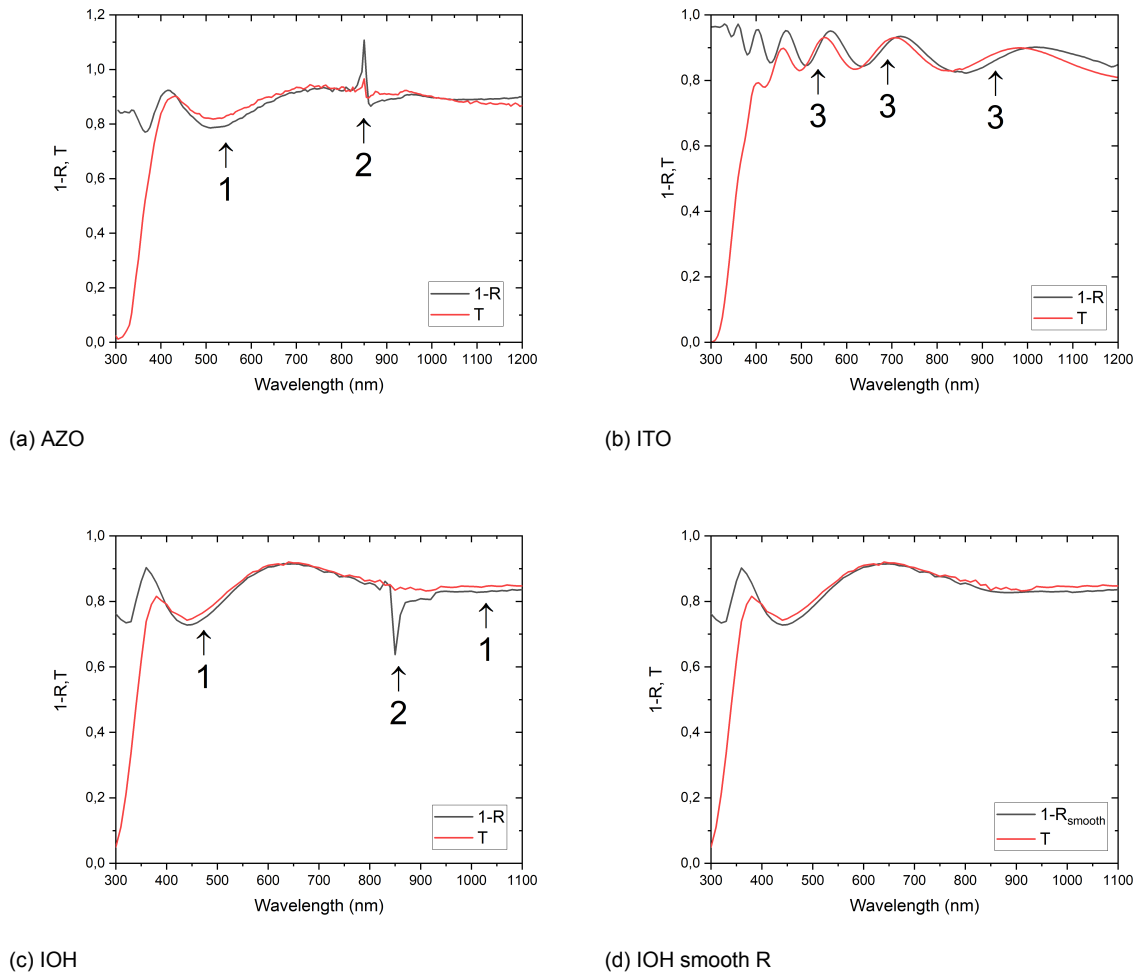
Figure 3.11: (a),(b),(c): the $1-R$, and T data measured using SP for an AZO, ITO, and IOH sample respectively. The causes of inaccuracy are indicated. 1: low absorption, 2: detector switch, 3: thickness inhomogeniousness. (d): the $1-R$, and T data measured using SP for the IOH with a correction in R (R_{smooth}) for the detector switch.

where the free carrier absorption is not that significant yet, so until about $800nm$. An obvious example of this can be seen in the R,T data for sample AZO20 in figure 3.11a. This low absorptance can also be present in the NIR region. Figure 3.11c shows this. To get an idea of when these negative values due to low absorptance occur, the lowest negative absorptance value (caused by the low absorptance reason) for the R,T data of multiple samples have been compared with parameters like film thickness.

2. Light detector switch   In for example, figures 3.11a and 3.11c, we can see unnatural jumps occurring around $850nm$. The measurement is done using different light detectors accurately for different wavelength regions. At about $860nm$, the equipment automatically changes the detector. It can be assumed that both detectors have a relatively low sensitivity at this point as it is at the end of their usable wavelength range. This poor sensitivity and switch cause the jumps at around $860nm$. These jumps cause negative absorptance values. These unnatural jumps can be removed from the data. This is shown for sample IOH 3(180) in figure 3.11d. It is obvious that some of the reflectance data points are not an accurate representation of the actual reflectance values. Therefore, these data points are deleted. Furthermore, to make the data more usable, it is smoothed using spline in Matlab [22]. It can be seen that the reflectance data has a more natural behavior around $860nm$ now. These steps can be taken for all data containing unnatural jumps due to the detector switch.

3. Thickness inhomogeneity   The thickness inhomogeneity of the sample can also cause negative absorptance values. As explained in the previous chapter, the reflectance and transmittance measurements are not done at the same time, and focusing the beam on the exact same sample spot for both the reflectance and transmittance measurement is quite difficult. Therefore, it can easily happen that the transmittance measurement is done for a different film thickness than the reflectance measurement. This causes a misalignment of the reflectance and transmittance interference fringes, and therefore overlapping regions where the absorptance is negative. This effect can be clearly seen for sample ITO 7kA in figure 3.11b. For one of the two characterization methods depending on R, T measurements, the negative absorptance due to thickness inhomogeneity can be corrected. This is shown in detail within section 3.5.
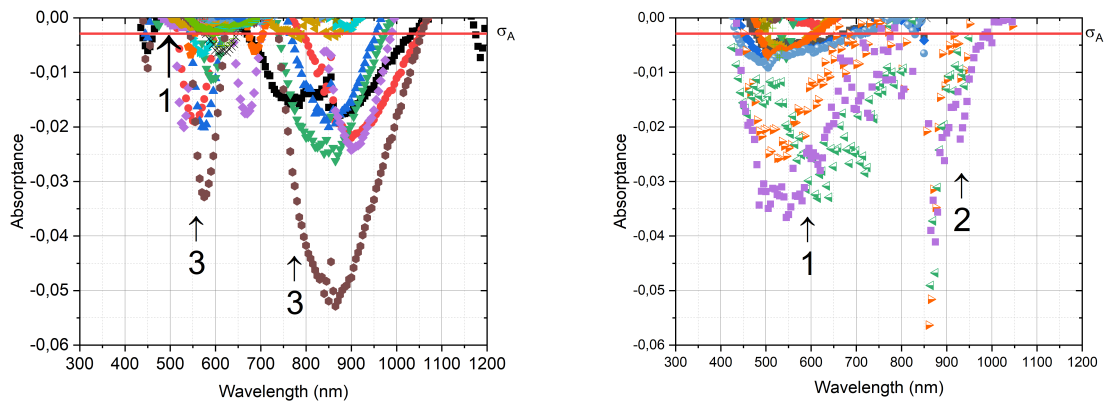
(a) ITO

(b) AZO
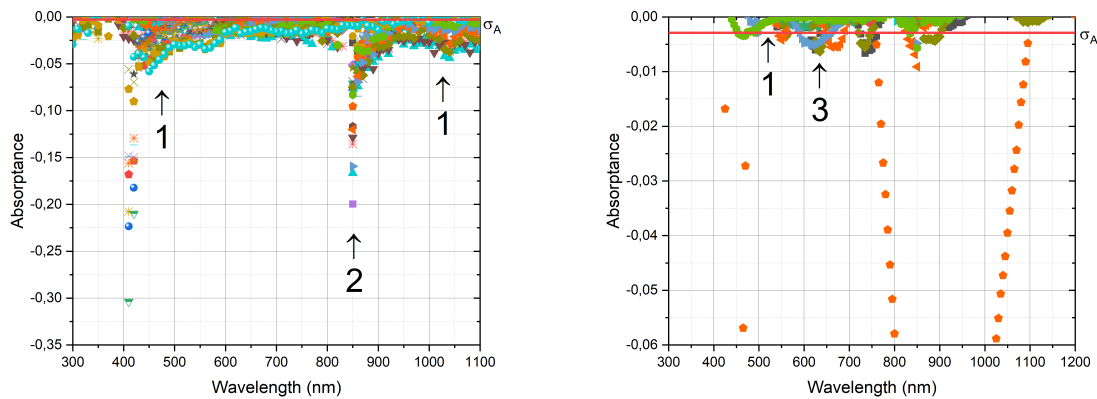
(c) IOH zoomed out

(d) i-ZnO

Figure 3.12: (a),(b),(c),(d): the negative absorptance values together with the error in absorptance, σ_A, for several samples of ITO, AZO, IOH, and i-ZnO respectively. The numbers indicate the causes of the negative absorptance, 1: low absorption, 2: detector switch, 3: thickness inhomogeneity.

3.3.2. Error analysis

Within the specifications of the Lambda 1050 equipment, the photometric accuracy is said to be ±0.002 Absorbance unit (Au) measured with NIST 930D Filters of $0.5Au$ for a wavelength region from $440 - 635nm$. Using the Beer-Lambert law and equation 2.41, this gives an accuracy in the transmittance of $\pm0.1453\%$. It is assumed that this error is valid for all wavelengths within the range of $300 - 1200nm$ and that the accuracy in the measured reflectance is the same. This gives $\sigma_R = \sigma_T = 0.1453\%$ and $\sigma_A = \sigma_R + \sigma_T = 0.2906\%$ for the absorptance. To compare this error with the negative absorptance

found from the RT measurements, these values have been put together in figure 3.12 for the ITO, AZO, IOH, and i-ZnO samples. In the figures, it is again indicated which trends belong to which type of negative absorptance. It can be seen that type 3, results mostly in parabolic features, type 2 results in sharp spikes around $850nm$, and type 1 results mostly in relatively flat trends close to zero. For AZO and IOH, it can be seen for some samples that both the trends of type 2 and type 1 are very large. This could be due to non-sufficient calibration of the equipment.

As has been explained before, negative absorptance values of types 2 and 3 can be corrected and do not relate to the accuracy of the actual equipment on itself, and can therefore be ignored in the comparison with the error σ_A. When comparing the negative absorptance of type 1 with the absorptance error σ_A, it can be seen that for ITO and i-ZnO, the error nicely includes the negative absorptance values. For AZO and IOH, the negative absorptance values of type 1 are significantly larger than the error which could indicate some systematic error of non-sufficient calibration of the equipment.

3.4. SCOUT

Like CompleteEASE [13] for spectroscopic ellipsometry, SCOUT [12] is a commercial (fitting) software that can be used to determine the optical properties of thin films. It needs RT measurements as input and then uses certain models in order to calculate RT and fit this against the RT measurement values. This way, for example, the dielectric function, complex refractive index, and thickness of the film could be retrieved. For the modeling of the TCO on a glass substrate, the layering within the software has been done as shown in figure 3.10 as this is a correct representation of how the R and T are measured.

3.4.1. The influence of roughness and inhomogeneity correction

Within SCOUT, there's also a possibility of adding a rough surface on top of the coating in the model. Just like SE, this is roughness is modeled using the Bruggeman approximation. To see the influence of this model on the resulting n and k values, the fitting has been done for four samples. Each with and without the Bruggeman model. For each material, the sample for which roughness had the most influence for SE, has been chosen. The results, together with the RT measurements of the samples, are shown in figure 3.13. Furthermore, in table 3.5, information about the fittings and fitting parameters can be found. It can be seen that the refractive index is not significantly influenced by the roughness model.

Material	Label	Model	FD $(x10^{-3})$	$d(nm)$	$d_{brugg}(nm)$
ITO	ito-4	No SR	0.93	390	-
		SR	0.18	350	70
AZO	AZO18	No SR	0.62	200	-
		SR	0.61	200	1
IOH	IOH 1(200)	No SR	0.91	120	-
		SR	0.91	120	0
i-ZnO	ZnO1	No SR	0.32	920	-
		SR	0.20	900	70

Table 3.5: Information on the fit deviation, FD, and the TCO layer thickness, d calculated using SCOUT including the Bruggeman (BM) model for roughness correction and excluding the BM model for one sample of each material. For the fittings where the BM model is included, the surface roughness height, d_{brugg}, is also given.

ito-4   SE calculated sample ito-4 to have the roughest surface and the k was also influenced the most for this sample. SCOUT, gives the same conclusion. This can be seen from both the fitting parameters and the figures. It can be seen in figure 3.13a that the roughness model especially influences the spectra region from about 400 till $550nm$. Without the roughness model, the extinction coefficient in this region is underestimated. When comparing the trend absorptance indicated in the R,T measurement graph with the extinction coefficient trend, it can be seen that from $400nm$ until $500nm$, the amount of absorptance is still increasing. The same trend is found within the extinction coefficient that includes the Bruggeman model. This trend is not found within the extinction coefficient that does not include the

Bruggeman model. From this it can be concluded that including the Bruggeman model in the SCOUT fitting, does improve the k results for rough surfaces.

AZO18 IOH 1(200)   The fit parameters for AZO18 and IOH 1(200) are pretty low and the extinction coefficients of the samples do not change that much. These changes are much smaller than those found with SE in section 3.2.2.

ZnO1   For ZnO1, the roughness fit parameters are quite high and indeed some changes in k are found. Figure 3.13d shows a significant increase in extinction coefficient in the range of $300 - 350 nm$. Furthermore, it shows a significant change in slope at about $900 nm$. So the model with roughness increases the influence of interband transitions but decreases the influence of free carrier absorption.

(a) ito-4

(b) AZO18

(c) IOH 1(200)

(d) ZnO1 (Zoomed out)
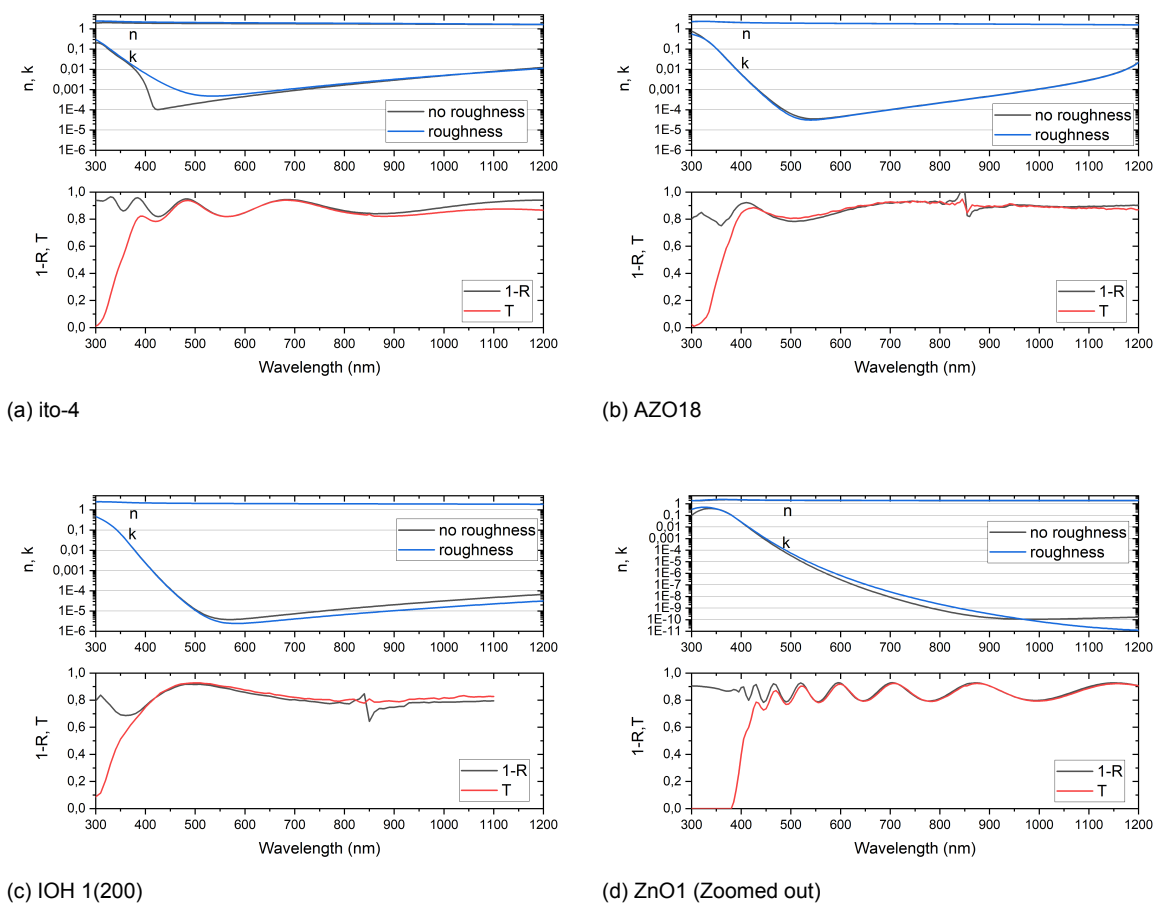
Figure 3.13: (a),(b),(c),(d): the n, and k values determined using SP + SCOUT including the Bruggeman (BM) model for roughness correction and excluding the BM model for one sample ITO, AZO, IOH, and i-ZnO respectively. The R, and T data measured using SP, on which the fittings in SCOUT were done are also shown.

3.4.2. Model comparison

Several combinations of models have been tried out for determining the n, k values. These model combinations are specified in table 3.6. An overview of the sub-models can be found in table 2.1. In figure 3.14, the results of the n and k values can be found and in table 3.7 with SCOUT calculated thicknesses and fit deviations are shown.

Model 4   It can be seen that for all four samples, model 4 gives results that are very deviating from the other three models concerning the n, k values. Furthermore, model 4 has the highest fit deviation

Absorption type\Model	1	2	3	4
Bound charge carriers	Kim	Kim + OJL2	Kim + Tauc-Lorentz	Tauc-Lorentz
Free charge carriers	Extended Drude	Extended Drude	Extended Drude	Extended Drude

Table 3.6: The combinations of models used for the SCOUT fittings and their labels.

for 3 out of four samples, which gives the indication that model 4 is not the correct model for TCOs. This makes sense, as model 4 uses only Tauc-Lorentz to model the bound charges and overtone vibrations. Tauc-Lorentz sets the absorption below the band gap to zero which is accurate for very crystalline materials. However, as explained in section 2.1.1, an amorphous or polycrystalline material has several short periodic structures which cause localized band states (within the energy gap) and therefore absorption below the band gap. The samples used here, are not fully crystalline.

Model 3   Models 1, 2, and 3 show better results than model 4, probably due to the contribution of the Kim model. Kim oscillator includes Gaussian behavior, which can be useful for modeling NIR vibrational overtones [38]. Although, model 3 shows an unnatural behavior for AZO12 between 500 and $750 nm$. From these graphs it cannot really be concluded which model is best for which material, so these models are compared with the PDS measurements in section 3.7.

(a) ITO20

(b) AZO12

(c) IOH42

(d) ZnO1 (Zoomed out)
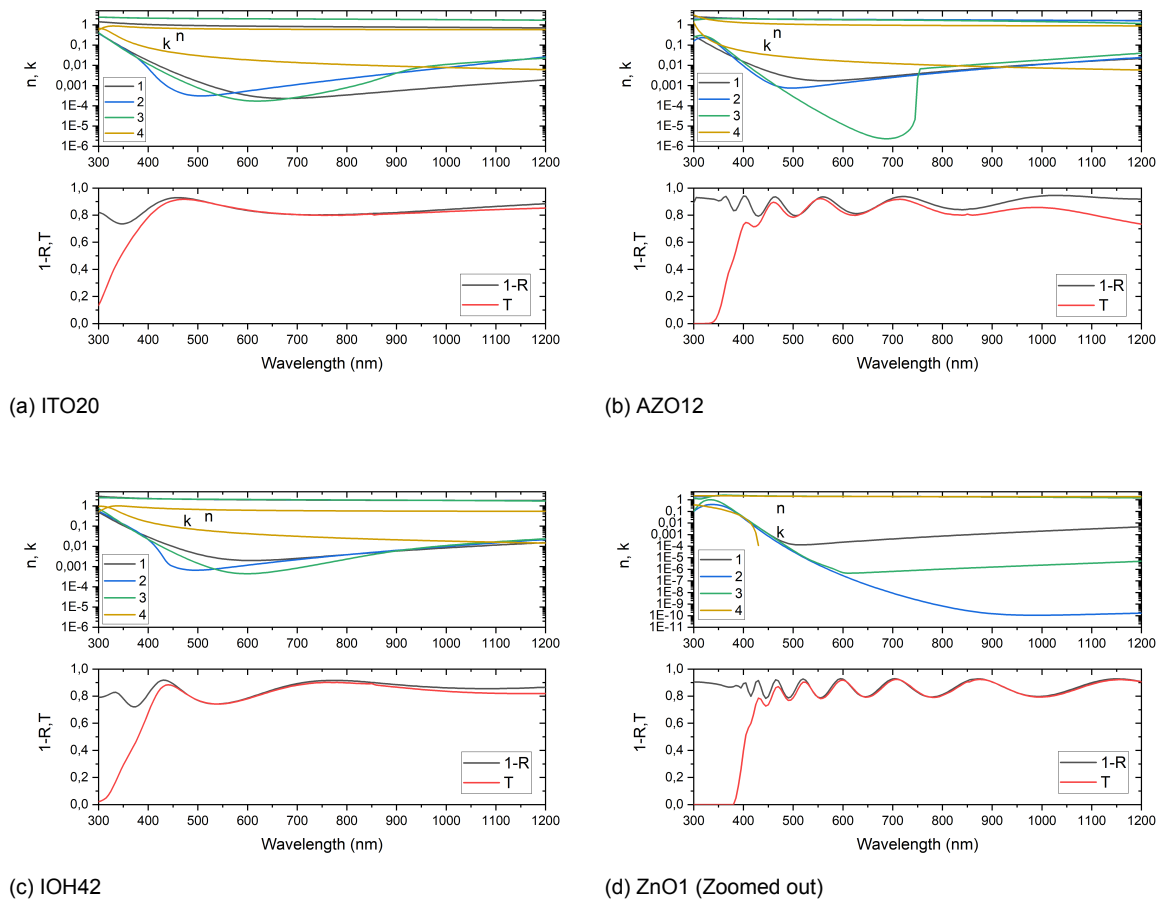
Figure 3.14: (a),(b),(c),(d): the results in n, and k determined using different combinations of fitting models in SCOUT for the samples of ITO, AZO, IOH, and i-ZnO respectively. The definitions of models 1, 2, 3, and 4 can be found in table 3.6.

Material	Label	Parameter model	1	2	3	4
ITO	ITO20	$FD(x10^{-3})$	4.56	0.08	0.10	7.55
		$d(nm)$	160	110	110	60
AZO	AZO12	$FD(x10^{-3})$	2.45	0.68	2.38	9.50
		$d(nm)$	600	600	470	260
IOH	IOH42	$FD(x10^{-3})$	0.80	0.04	0.13	6.69
		$d(nm)$	200	200	200	70
i-ZnO	ZnO1	$FD(x10^{-3})$	3.30	0.32	3.50	0.76
		$d(nm)$	760	920	760	920

Table 3.7: Information on the fit deviation, FD, and the TCO layer thickness calculated using SCOUT for the different models 1, 2, 3, and 4, for samples of the materials ITO, AZO, IOH, and i-ZnO. The definitions of models 1, 2, 3, and 4 can be found in table 3.6.

3.5. Reversed GenPro4

3.5.1. Simulation setup

Another method to determine the complex refractive index using RT measurements uses the software GenPro4 (GP4) [31], developed within the PVMD group. Normally GP4 is used to calculate the optical response of a certain layered structure. Each material modeled in the simulation needs the material-specific complex refractive index. The output of the simulation will then contain data like the absorptance in each layer, the photo current density, etc. In this report, this way of using GP4 is called "Forward GenPro4". A Flowchart describing the forward GenPro4 can be found in figure 3.15a. To use GP4 for the characterization of a certain layer, a "Reversed GenPro4" method is developed. in order to determine the complex refractive index of a TCO film of interest, a layered structure is built within GP4 as shown in figure 3.10 as the RT measurements are done in the same way. An overview of how this method works can be seen in figure 3.15b.

(a) Forward GenPro4
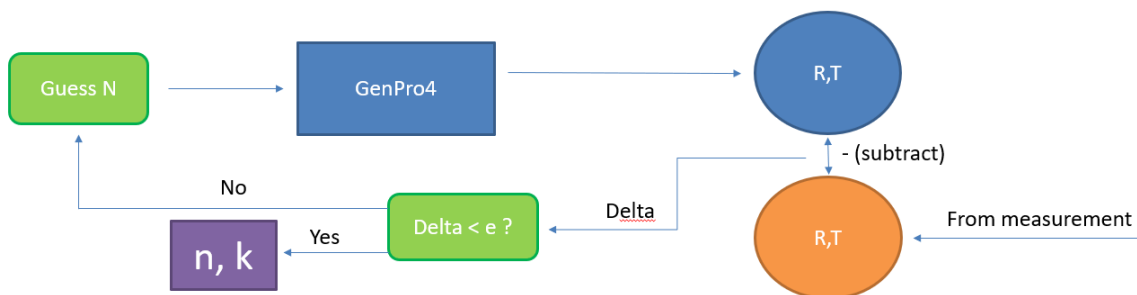
(b) Reversed GenPro4

Figure 3.15: (a): a flowchart that shows the forward way of using GenPro4 for optical response calculations. (b): the reversed way of using GenPro4 for calculations of $N = n + ik$.

The first step consists of guessing the complex refractive index of the TCO coating on top of the glass substrate. For the glass substrate, already-known values for the complex refractive index and layer thickness are used. For the thickness of the TCO coating, values resulting from SE measurements are

Material	Label	MSE_{SE}	$FD_{SC} x10^{-3}$	MSE_{GP4}	d_{SE}
AZO	AZO7	11.3	4.50	1.6	400
	AZO13	4.2	0.02	5.8	620
ITO	ITO 7kPA	20.6	1.23	2.6	590
	ITO30	3.8	0.27	3.0	150
IOH	IOH42	17.3	0.04	4.4	190
	IOH27	2.7	0.32	7.8	110
i-ZnO	ZnO1	32.1	0.40	17.6	900
	ZnO24	4.6	0.48	5.4	130

Table 3.8: Information of the fit deviations for SE, MSE_{SE}, SCOUT, FD_{SC}, and GP4, MSE_{GP4}, and the via SE calculated thickness, d_{SE}, for multiple samples.

used. GP4 then calculates the absorptance in every layer. The absorptance in the air above the TCO coating can then be compared to the reflectance measured with Lambda and the absorptance below the glass substrate can be compared with the transmittance measured using Lambda. A deviation, $Delta$, between the via GP4 calculated R_{GP4} and T_{GP4} and the measured R_L and T_L is calculated using the following formula:

$$Delta = abs(R_{GP4} - R_L) + abs(T_{GP4} - T_L) \qquad (3.3)$$

The minimization solver "Patternsearch" is used to guess new values for the complex refractive index until the solver has found the global minimum for Delta. This minimization problem is done for every wavelength separately and if the optimal N is found for one wavelength, then this N is used as an initial guess for the next wavelength. Furthermore, an MSE is calculated using the following formula:

$$MSE_{GP4} = \sqrt{\frac{1}{2}\Sigma_{i=1}^{n}[(R_{GP4} - R_L)^2 + (T_{GP4} - T_L)^2]1000} \qquad (3.4)$$

The code that is used can be found in chapter C of the appendix.

3.5.2. The influence of inhomogeneity correction

As shown in section 3.3.1, inhomogeneity of the film thickness could lead to negative absorptance for thicker films where interference fringes are very present. Normally, when the R and T of the lambda measurement are such that they result in negative absorptance values, GP4 would not be able to do the calculations and give warnings. Because of this issue, a lower bound of 0 was added to the minimization solver regarding the calculation of k. An AZO sample has been taken as an example. This sample has negative absorptance values due to inhomogeneity as can be seen from the $1 - R$, and T measurements in figure 3.16a. The simulation for this sample was done with a TCO thickness set on the thickness calculated via SE: $d = 577nm$. The result in absorption coefficient is calculated via equation 2.15 and shown in figure 3.16b. As can be seen from the blue graph, the lower bound of zero and negative absorptance, results in a very large drop in k, which is of course unnatural. An attempt on avoiding the negative absorptance values due to inhomogeneity is done.

The method described in the previous section uses a single TCO coating thickness in order to minimize for R and T. But the code can be rewritten containing two minimization problems. One for the minimization of the deviation of R and one for minimizing the deviation in T. For each minimization, a different thickness can be used. This is tried for sample AZO12. In figure 3.16a, the difference in wavelengths between two interference peaks is indicated. It is assumed that the difference in film thickness is equal to the difference in wavelength. The result in absorption coefficient calculated via equation 2.15 and shown in figure 3.16b. The TCO thickness for the reflectance minimization is set on $d_R = d = 577.27nm$. For the minimization of the transmittance, the thickness is set on $d_T = d_R - 5nm = 572.27nm$. From the result in the absorption coefficient, it can by using the two thicknesses, the negative absorptance and therefore drop in k is avoided. Furthermore, the MSE value of the simulation using one thickness was found to be 3.43 and the MSE value of the simulation using two thicknesses was
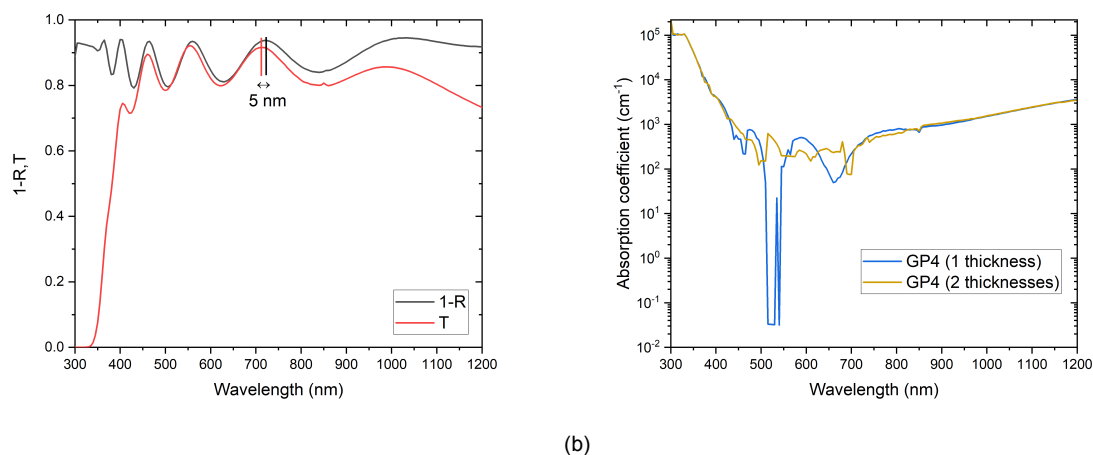
Figure 3.16: (a): the R and T data form SP measurement with the wavelength difference between two peaks indicated. (b): the result in absorption coefficient calculated from the k values determined using GP4, both for one thickness (the same thickness for R, and T, and two thickness values (one for R, and one for T).

found to be 2.66. This shows, that GP4 was able to find a better agreement between the simulated and measured R and Ts.

3.6. Comparison of the three methods

3.6.1. Refractive index

The refractive indexes for AZO samples, AZO7 and AZO13, for ITO samples, 7kPA and ITO30, for IOH samples, IOH42 and IOH27, and for i-ZnO, ZnO1, and ZnO24, are determined using the three characterization methods, and shown in figure 3.17. The It can be seen that for almost all samples shown, the refractive indexes of the three methods are very similar. GP4 refractive indexes have very large peaks due to the minimization solver not finding a low enough Delta, but the start en ending points of those peaks follow a very similar trend to SE and SCOUT. This, and the fact that the refractive index for both SE and SCOUT was quite robust with changing fitting range and/ or roughness correction, indicates that the refractive index from both SE and SCOUT can be trusted.

Material	Label	MSE_{SE}	$FD_{SC} x 10^{-3}$	MSE_{GP4}	d_{SE}
AZO	AZO7	11.3	4.50	1.6	400
	AZO13	4.2	0.02	5.8	620
ITO	ITO 7kPA	20.6	1.23	2.6	590
	ITO30	3.8	0.27	3.0	150
IOH	IOH42	17.3	0.04	4.4	190
	IOH27	2.7	0.32	7.8	110
i-ZnO	ZnO1	32.1	0.40	17.6	900
	ZnO24	4.6	0.48	5.4	130

Table 3.9: Information on the samples used for the comparison of the refractive index determined by SE, SP+SCOUT, and SP+GenPro4. MSE_{SE}: the mean-square error of the SE fitting, FD_{SC}: the fit deviation from SCOUT, MSE_{GP4}: the mean-square-error for the difference between the calculated RT and the RT data obtain using SP, d_{SE}, the TCO layer thickness determined using SE and used as thickness for the other methods.
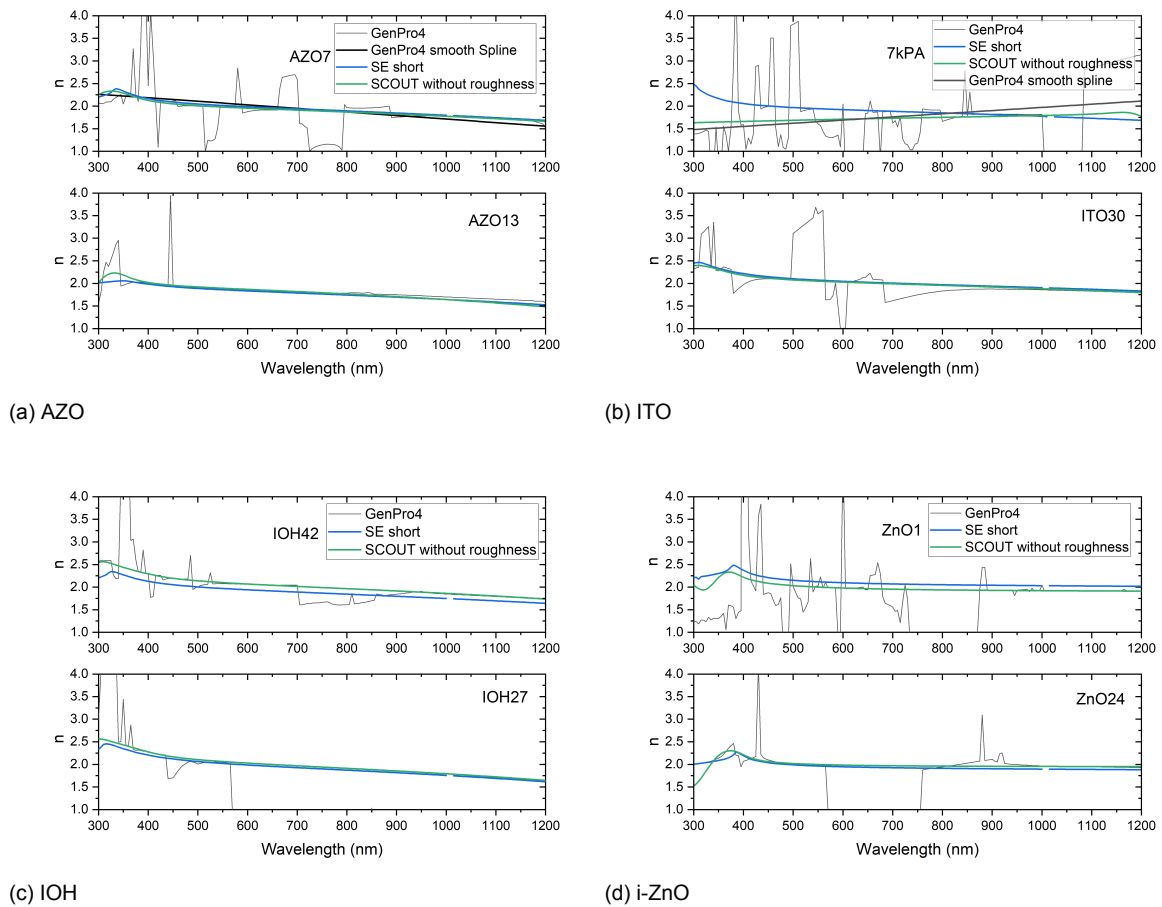
Figure 3.17: (a), (b), (c), (d): the refractive index determined using three different methods, SP + GenPro4, SP + SCOUT, and SE for several samples af AZO, ITO, IOH, and i-ZnO respectively.

3.7. Comparison with Photothermal deflection spectroscopy

3.7.1. methodology

In the last part of the characterization chapter, the measurement and data analysis methods described within this chapter will be compared to absorptance measurements obtained via Photothermal deflection spectroscopy (PDS). In order to obtain PDS measurements, new samples were deposited on a quartz substrate. This is done within the PVMD group. The deposition information of these samples can be found in chapter A of the appendix. The measurements were done in a setup built in-houese at FZU – Institute of Physics of the Czech Academy of Sciences Na Slovance in Prague. Furthermore, SE and SP measurements on those samples were done so that the characterization methods described in this chapter can be compared to the PDS measurement.

Measurement comparison

Firstly, the measurement methods will be compared by comparing absorptance values and extinction coefficient values. The SE measurement and data analysis are seen here as a one-package deal. In figure 3.18a can be seen how all the absorptance values compared, were obtained. The PDS measurement obviously gave a direct absorptance result, the absorptance using SE measurement is determined by fitting (short range) for the complex refractive index using SE measurement data and then calculating the absorptance using both GP4 and Beer-Lambert and the fitted n and k values. The absorptance of the lambda measurement is obtained using $A = 1 - R - T$. After comparing the absorptance values, the extinction coefficients are compared, as this is the result of SE. In figure 3.18b, it is shown how all

the extinction coefficient values were obtained. The extinction coefficient from the PDS measurement is obtained via Reversed GP4 and Beer-lambert law. The extinction coefficient from Lambda is obtained in the same way, using RT and $1 - R - T$. It is preferred, for the k value to be the only changing data. Therefore, for the calculation of the extinction coefficients, the refractive index determined by SE is used for every calculation.

(a) Absorptance

(b) Extinction coefficient
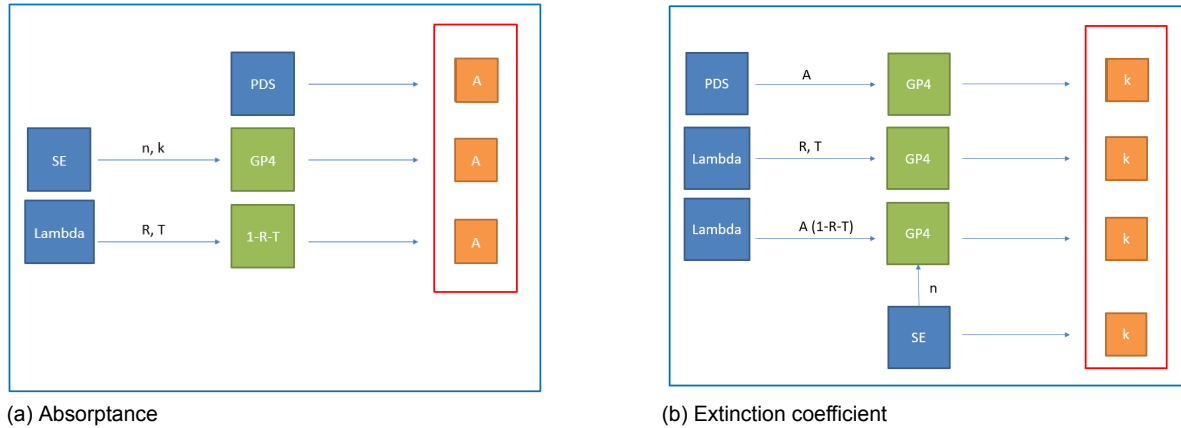
Figure 3.18: (a), (b): flowcharts that show the steps taken to compare PDS with the other methods for the absorptance, and the extinction coefficient respectively.

Measurement + data analysis comparison

After the comparison of the measurements, a comparison in the use of different data analysis models is done. For this, the complex refractive index obtained with SCOUT using the three different models is compared with the PDS complex refractive index. The same comparison is done for SE short- and broad-range fitting.

3.7.2. Measurement comparison

Absorptance comparison

As the absorptance obtained from the R, T measurements obtained negative absorptance values due to low absorptance for all the PDS samples, an extra data modification step was taken to remove the negative absorptance values. An example of this modification is shown for sample A1 in figure 3.19. In the bottom graph, the R, T data is shown and the width of the negative absorptance is indicated with red arrows. In the top graph, the absorptance from Lambda (blue) is placed next to the PDS absorptance (black dash) and it can be seen that the shape of the graphs is very similar except for the negative absorptance. As the error determined in section 3.3.2 is too small to account for the negative values, the maximum negative value, which is assumed to be at the lowest absorption point, is used as a correction value. For A1, the maximum negative value was found to be -0.01902. The yellow line in the graph shows the result of $A_{Lambda} + 0.01902$. It can be seen that by shifting the absorptance upwards just above zero, the PDS absorptance and Lambda absorptance are almost identical.

To obtain the absorptance of SE, GP4 was used. As these TCO coatings were deposited on quartz substrates, the RT measurent of the quartz substrate has been used to obtain the complex refractive index of a quartz material. As the quartz RT data also showed negative values the same correction method has been applied, but this time assuming that half of the correction value is due to the reflectance and half due to the transmittance. From this the refractive index, shown in purple in figure 3.19b, is obtained using the glass model in SCOUT and compared to the refractive index of SiO_2 from the SE database. The extinction coefficient has been set to zero as the absorptance for a quartz substrate is negligible. These quartz n and k values are used for the substrate layer in GP4.

In figure 3.20, the results can be seen for all the absorptance values. The correction method has been applied to all the lambda absorptance data. The thicknesses and SR obtained from SE are shown in table 3.10. For samples A1 and H1, it can again be seen that PDS and lambda have a very similar
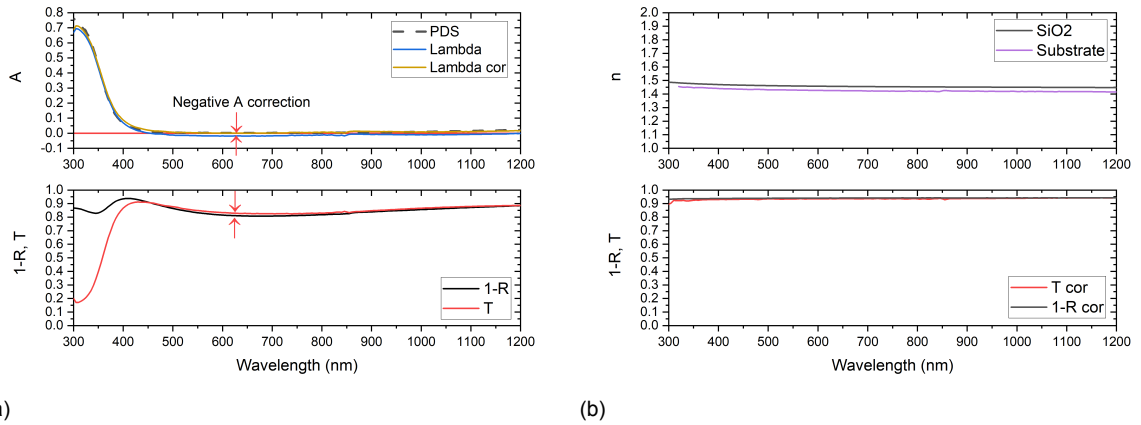
Figure 3.19: (a): the absorptance profiles of sample A1 from the PDS measurement, together with the $A = 1 - R - T$ SP measurement, with and without correction. Furthermore, the RT data is shown of sample A1. (b): the refractive index used for the quartz substrate next to the refractive index of SiO_2 from the SE database. Furthermore, the RT data is shown of sample the quartz substrate.

trend and that even for very low MSE values, SE shows a less accurate trend. For H2 and Z1, both samples are expected to have a very low free carrier absorption, and both Lambda and SE are lacking in accuracy.

Material	Sample	MSE_{SE}	$d(nm)$	$SR(nm)$	$MSE_{GP4}PDS$	$MSE_{GP4}A$ Lambda
AZO	A1	5.4	100	8.1	3.63e-05	2.84e-04
IOH	H1	2.0	85	2.4	3.79e-05	1.64e-04
	H2	2.2	85	2.1	0.0013	3.54e-05
i-ZnO	Z1	5.8	480	11.8	12.89	9.72

Table 3.10: Information on the samples A1, H1, H2, and Z1. MSE_{SE}: MSE from SE, d: TCO layer thickness, SR: surface roughness calculated using SE, MSE_{GP4}: the MSE form GP4 simulations.

Refractive index
In section 3.6.1, it was shown that SE, spectrophotometry + GP4, and spectrophotometry + SCOUT, give similar results for the refractive index. From this and the fact that the refractive index for both SE and SCOUT was quite robust with changing fitting range and/ or roughness correction, it can be concluded that the refractive index from both SE and SCOUT can be trusted and that the refractive index from SE can be used for the extinction coefficient calculation within this section.

Extinction coefficient comparison
The results of all the extinction coefficients can be found in figure 3.21 calculated using GP4. Trends similar to absorptance trends are found. For A1, it has been in addition to the other samples tried to determine the extinction coefficient for lambda using corrected RT data and the n from SE, but it can be clearly seen that this method does not give an accurate result. Furthermore, for H2, the extinction coefficient is also obtained using the not-corrected absorptance of Lambda and the n of SE, but this is also not successful.

3.7.3. Measurement + data analysis comparison
SE broad/short-fitting
In section 3.2.3, it was shown that the wavelength range for which the SE fitting is done, can have a significant influence on the result in k. In this section, the short and broad-range fitted results in k are compared with the result in k determined using the PDS absorptance measurement in combination with GP4. This is done, to see which fitting range would give results that agree more with PDS, and the results are shown within figure 3.22 for samples A1, H1, H2, and Z1. The change in fitting range

(a) A1
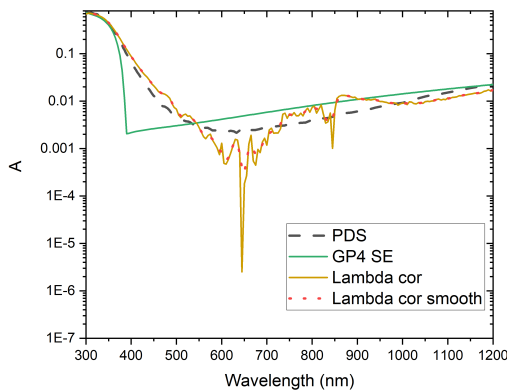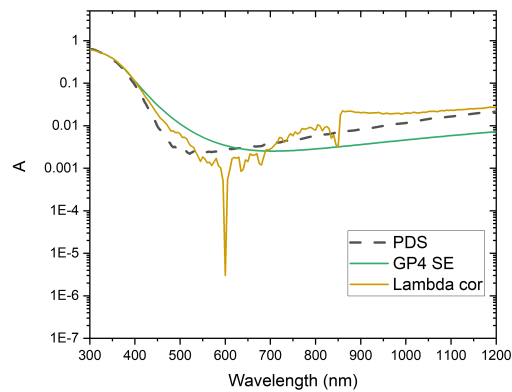
(b) H1
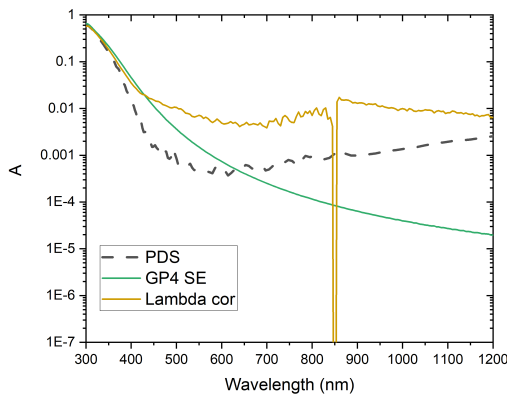
(c) H2
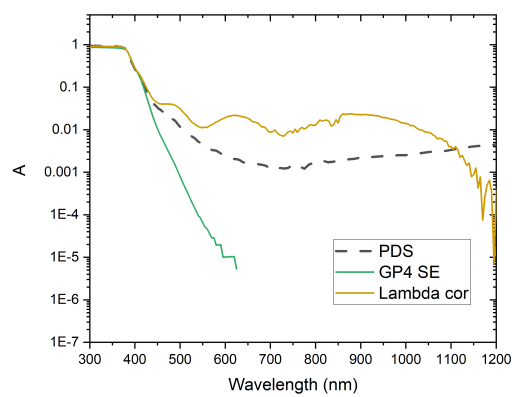
(d) Z1

Figure 3.20: (a),(b),(c),(d): The results for the absorptance determined by PDS, SE + GP4, and $A = 1 - R - T$ form SP measurements for the samples A1, H1, H2, Z1 respectively. (a) also shows the smoothed absorptance from SP using spline.

does not change the shape of the k trend much, but mostly the offset height of the values. Therefore, it can be seen that for all four samples, using the short wavelength range or the broad does not matter in terms of accuracy.

A1 and H1   For sample A1, it can be seen that from 600 until about $1000nm$, the short-range fit agrees with PDS more than the broad-range fit in terms of height level. But, from about 400 until $500nm$, the broad-range fit seems to be better. For sample H1, the short-range fit agrees better from about 700 until $1200nm$, while the broad-range fit agrees better from about 450 until $600nm$.

H2 and Z1   For both samples H2 and Z1, the results for both fitting ranges are very different from the PDS result, therefore, one result is not better than the other.

SCOUT models
In section 3.4.2, the results in k for four different model combinations were shown. In this section, three of those models are compared to the results in k for the PDS measurement in combination with GP4. These results are shown in figure 3.23. The graphs show the results for the RT data withouth any corrections made, and for the RT data the transmittance is corrected similar to the way the absorptance was corrected ($T - absorptance correction$). It can be seen the results for all three models do not agree with the PDS results at all. In 3.4.2 we saw k trends calculated by SCOUT that seemed more realistic

(a) A1
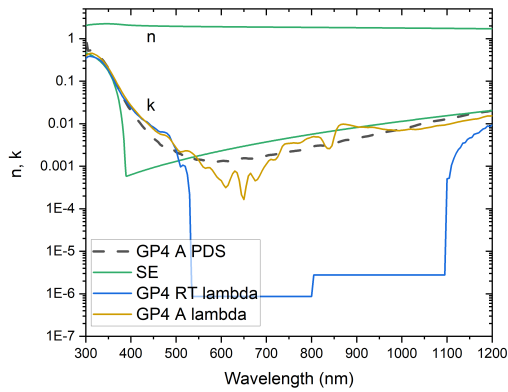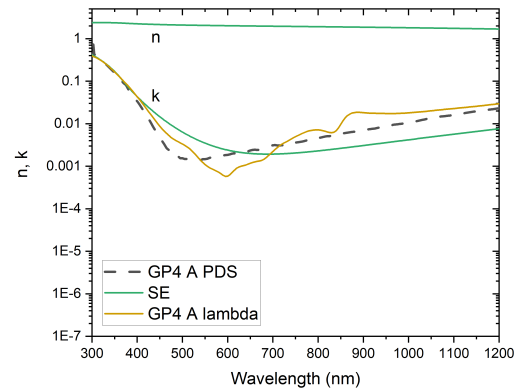
(b) H1
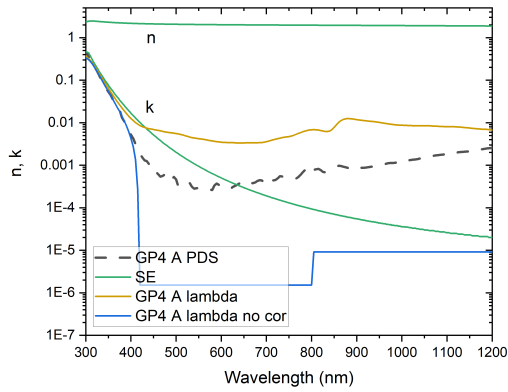
(c) H2
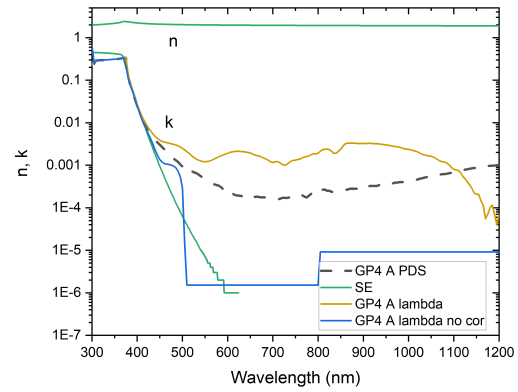
(d) Z1

Figure 3.21: (a),(b),(c),(d): The results for k determined by PDS + GP4, SE, and $A = 1 - R - T$ + GP4 with the correction for the samples A1, H1, H2, Z1 respectively. (a) also shows the k from RT+GP4, (c), and (d) also show k for $A = 1 - R - T$ + GP4 without the correction.

than the trends shown here. As in section 3.7.2, we also saw very low k values calculated by GP4 withouth the absorptance correction, it could be that the RT measurement data for samples A1, H1, H2, and Z1, contains a larger error than for the samples used in the previous sections. The larger error would result in higher negative absorptance values and therefore worse results in k.

(a) A1
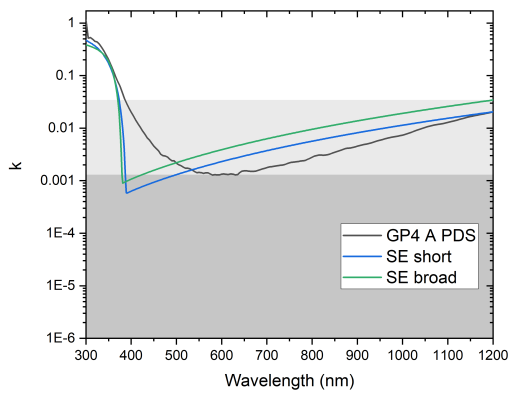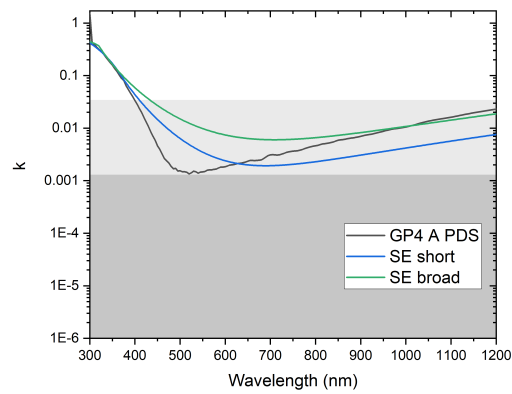
(b) H1
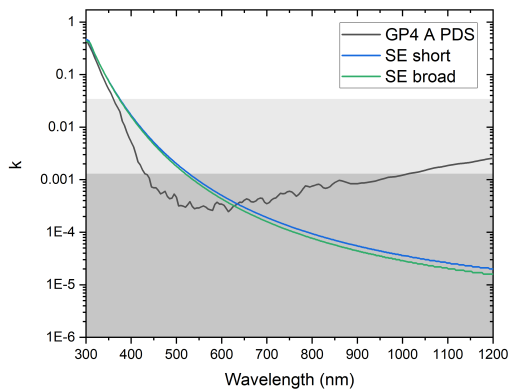
(c) H2
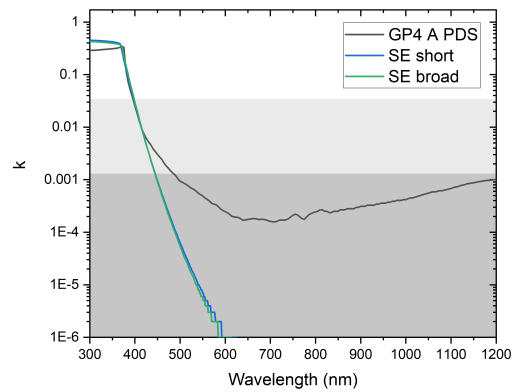
(d) Z1

Figure 3.22: (a),(b),(c),(d): The results for k determined by SE for both short-range fitting and broad-range fitting for the samples A1, H1, H2, Z1 respectively.

3.8. Conclusion

The main objective of this chapter is: Compare commercially used methods, spectroscopic ellipsometry, and spectrophotometry + SCOUT, for determining the complex refractive index of TCO films with new methods using spectrophotometry + GenPro4 and photothermal deflection spectroscopy + GenPro4 to build a guide for the optical characterization of TCO films.

A Guide on optical characterization   PDS has a very low absorption sensitivity ($\alpha = 10^{-6}$), compared to the other measurement techniques, and is not influenced by layer thickness. Therefore, PDS was assumed to be the most accurate for both thin and thick samples, and low and high absorption. As PDS can be a challenging measurement to do, other methods that show similar results to PDS are preferred. It was found, for materials with relatively high absorption profile ($k > 0.001$), so materials with a relatively high charge carrier density and/or an amorphous-like miro-structure, that SP + GenPro4 (+ applied negative A correction) can be used as a replacement of PDS + GenPro4 (under the condition that SP data does not contain negative values due to thickness inhomogeneity and/or detector switch). For this situation, SE could also be used if the exact shape of the k trend is less important.

(a) A1

(b) H1
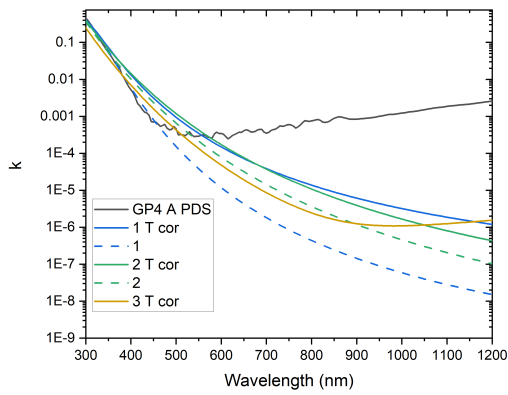
(c) H2
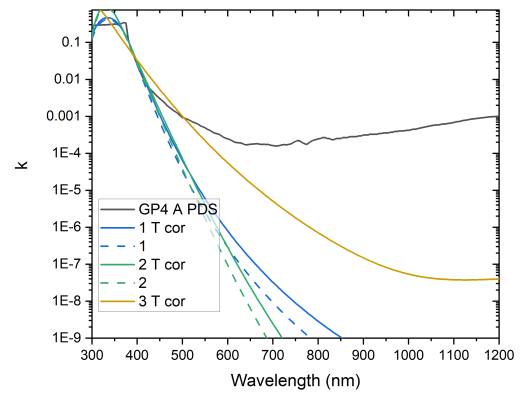
(d) Z1

Figure 3.23: (a),(b),(c),(d): The results for k determined by SCOUT for three different models using both not corrected transmittance and corrected transmittance for samples A1, H1, H2, Z1 respectively.

Front contact and back-reflector design

In chapters 1, and 2, the importance of the front contact and back reflector TCO layers in a tandem thin film silicon solar cell was explained. Within this chapter, an optical analysis is done for the design of the front contact TCO layer and back-reflector TCO layer of a tandem silicon thin film solar cell taking into account both different materials and the layer thickness. For the front contact layer, a new IOH, and i-ZnO combined bilayer will be compared to the standard AZO, and ITO single layers. For the back reflector, an i-ZnO/silver combination will be compared to the standard AZO/silver back reflector. Throughout the chapter, the analysis is done focusing on parameters like absorptance, photocurrent density, and sheet resistance. The chapter starts with choosing the best AZO, ITO, IOH, and i-ZnO samples to use for the simulations, taking into account both the optical and electrical properties of the samples. All TCO samples used within this report were previously deposited within the PVMD group. The ITO, AZO, IOH, and i-ZnO samples were deposited using Radio Frequency (RF) magnetron sputtering technique. Some of the samples were annealed with a saturated annealing time of 20 min and an annealing temperature varying between 130 and $250^o C$. The deposition information on the samples used within this report can be found in tables A.2 A.1, A.3 and A.4 for ITO, AZO, IOH, and i-ZnO respectively.

4.1. Methodology
In figure 4.1, the general structure of this chapter is visualized.
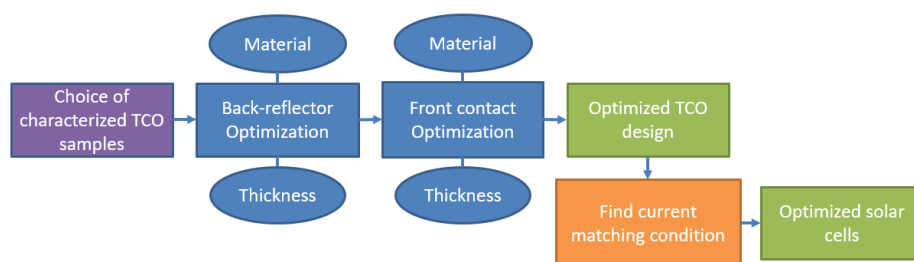
Figure 4.1: A flowchart that shows the general structure of this chapter. The oval boxes represent the parameters that are varied for comparisons and/or optimizations.

4.2. Choice of samples
For the GenPro4 simulations that are done in this research, the material-specific complex refractive index values are needed as input. The complex refractive indexes for the TCO layers simulated within this report are taken from previously deposited samples. The samples from which the complex refractive index values are used are chosen on their optical and electrical performance. In this section, it will

be explained which method to determine N is used and why, and it will be described which samples are chosen and how the choice is made.

4.2.1. Optical characterization method

In the previous chapter, it was found that for most cases, the use of PDS in combination with SE and GenPro4 would give the most accurate result regarding the N of a TCO thin film. Unfortunately, at the moment of starting the research described in this chapter, this was not yet known, furthermore, PDS was not in near availability. Therefore, a compromise had to be made in choosing the characterization method. As it was found in the previous chapter that all three methods not using PDS had a limitation for low absorption profiles, this compromise will have its biggest effect on the samples that contain very low absorption profiles. For simplicity, it was chosen to use only one characterization method for all the samples used within this chapter. The decision on the characterization method was made taking into account three aspects: the simplicity of the method, the robustness of n, and the relative differences between the k trends of different materials. SE is the quickest method compared to SP+SCOUT and SP+GenPro4. Furthermore, SE was found to have the most robust calculations for the real refractive index, and it is found that the extinction coefficients calculated via SE show a distinct difference between the different materials.
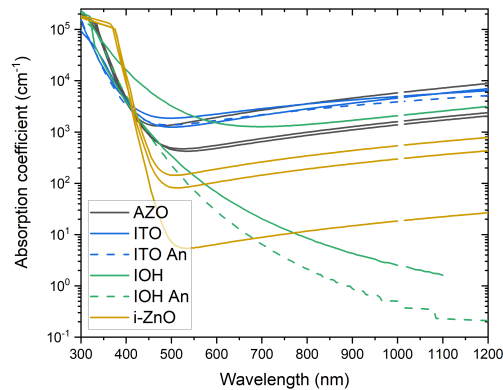
Figure 4.2: The α trends of several randomly chosen samples of AZO, ITO, IOH, i-ZnO materials calculated using SE. The dashed lines show the α of annealed samples.

In figure 4.2, the absorption coefficients calculated from the extinction coefficients using equation 2.15 are shown for a couple of samples. It can be seen that k for i-ZnO is found to be lower than AZO or ITO, which is as expected. Furthermore, it shows that annealed samples have a lower k trend than the non-annealed samples. Some of the results shown for IOH, the two lowest α trends are questionable as they are not showing any free carrier absorption, and as in the previous chapter it was found that SE is not accurate for α values lower than about $200 cm^{-1}$. Therefore, for the research in this chapter, it is assumed that for the samples that SE calculates unrealistically low k values, the absorptance, in reality, is also very low and that the k compared relatively to other samples, still makes sense.

4.2.2. Performance calculation

To simulate the optical response GenPro4 needs the complex refractive index values as material-specific input. The n and k values for each TCO material are chosen from the samples that have good optic and electric properties. This chapter focuses mostly on the optical analysis when comparing the different front and back TCO designs. But, as explained in chapter 2, the TCO film with the best optical properties, will most of the time not also have the best electrical properties. If the sample with the best optical properties is chosen without taking into account the electrical properties, the eventual analysis will be unrealistic. Therefore, a trade-off between optical and electrical performance almost always has to be made.

IOH and i-ZnO   The materials IOH and i-ZnO are in this chapter mainly used for the new bilayer design developed by Kalpoe [17]. To keep a link between the computational work done in this report and the experimental work leading to the new bi-layer design, the samples of IOH, and i-ZnO, that Kalpoe found to have high mobility and low charge carrier density are used within this chapter. The deposition parameters are given in table 3.12d.

Material	$t(s)$	$P(W)$	$T_{heater}(^oC)$	$p(E-3mbar)$	$p_{H_2O}(E-5mbar)$	$T_{an}(^oC)$
IOH	2000	150	25	5.7	3	200
i-ZnO	3600	200	95.4	2.6	-	-

Table 4.1: The deposition parameters, and the mobility, μ, and charge carrier density, N_e, of the IOH and i-ZnO samples used for the analysis of the front contact and back reflector design. t: deposition time, P: deposition power, T_{heater}: heater temperature, p: pressure, p_{H_2O}: partial water pressure, T_{an}: annealing temperature.

The n and k values of these IOH and i-ZnO samples are determined using SE and are shown in figures 4.3a, and 4.3b respectively. It can be seen that IOH has a lower k for the blue region ($300 - 400nm$) and the NIR region ($700 - 1200nm$) than i-ZnO, while i-ZnO has a lower k for the visible region. Furthermore, the important thing to notice is that the k trend for IOH, indicates that there is no free carrier absorption (FCA) in the sample. It has to be kept in mind during the remainder of this chapter that this is very likely an underestimation of the absorption in the NIR region due to the low sensitivity of SE for weak absorption.

(a) 65 nm

(b) 930 nm
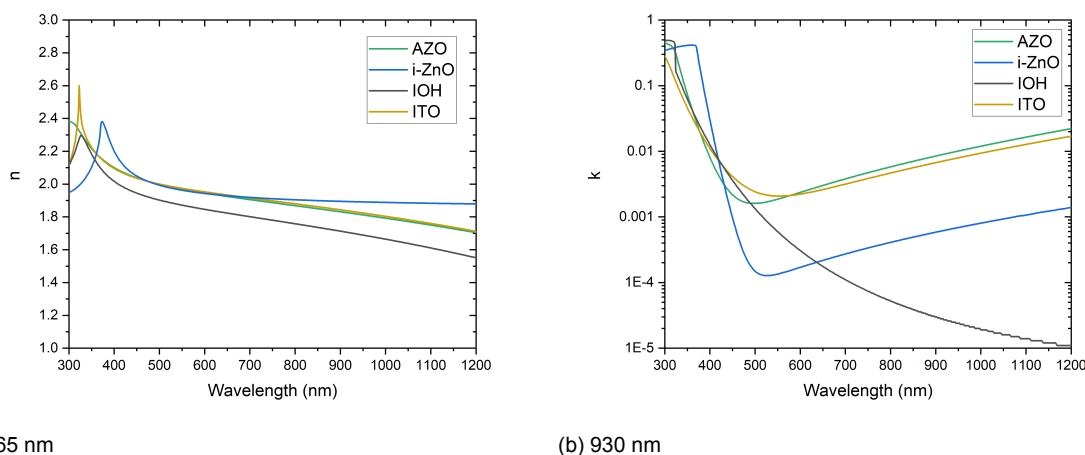
Figure 4.3: a: the refractive index of the AZO, ITO, IOH, and i-ZnO samples used within this chapter, calculated using SE. b: the extinction coefficient of the AZO, ITO, IOH, and i-ZnO samples used within this chapter, calculated using SE.

AZO and ITO   For the AZO and ITO samples, the mobility and charge carrier density were only available for a small part of the deposited samples. Therefore, other parameters are used to make a trade-off between the optical and electrical performance of the samples. The wavelength averaged transmittance (from $300-1200nm$), T_{av}, is used to describe the optical performance, and the sheet resistance, R_{sh} (and resistivity ρ), is used as a measure for the electrical performance. For the trade-off, formula 2.8, the Haacke high-resolution figure of merit, is used. It is assumed that in our case, $n = 12$ will be sufficient enough. The R_{sh} was measured previously in the PVMD group of Delft University of Technology using the 4-point probe technique.

T_{av} is calculated with GenPro4 using the 'flat' model and the layered structure shown in figure 4.4a with $d_{TCO} = 100nm$. The TCO layer is placed under the glass, as in the case of a thin film solar cell, the light will also first go through the glass and then the TCO. To match the R_{sh} with the average transmittance in terms of film thickness, the resistivity is calculated by $\rho = R_{sh} * d_{SE}$ where d_{SE} is the film thickness of the actual TCO sample calculated using SE. As the relative performance difference

Material	$t(s)$	$P(W)$	$T_{heater}(^oC)$	$T_{an}(^oC)$
AZO	3600	300	200	-
ITO	3000	130	25	180

Table 4.2: The deposition parameters, and the T_{av}, and R_{sh}, of the AZO and ITO samples used for the analysis of the front contact and back reflector design. t: deposition time, P: deposition power, T_{heater}: heater temperature, T_{an}: annealing temperature.

between the film samples of the same material is important now, for simplicity it is assumed that the different films of each material have the same resistivity/film thickness trend with different offsets. Then, the thickness-matching R_{sh} is calculated by $R_{sh} = \frac{\rho}{d_{TCO}}$. In table chapter B, in the appendix, all the results of these performance calculations can be found.

(a) Simulation structure

(b) Spectrophotometric structure
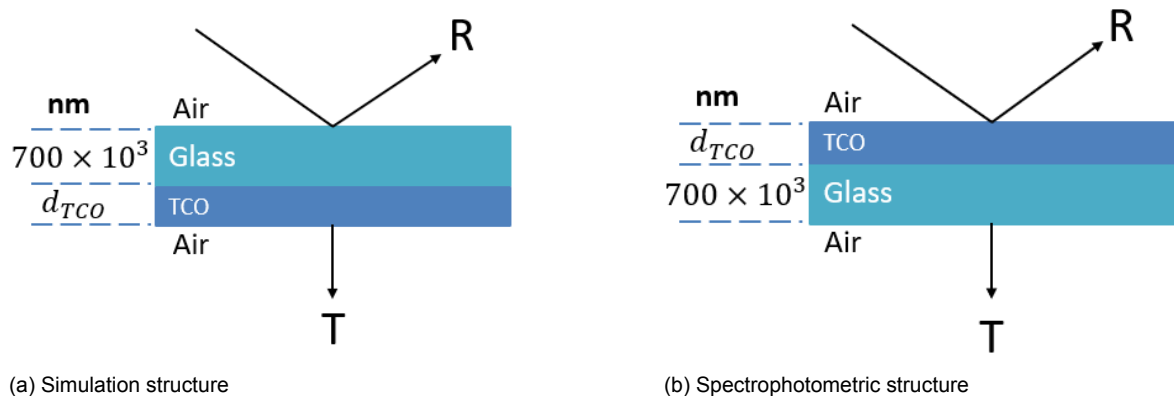
Figure 4.4: Schematics of the TCO on glass substrate-structures used for different situations. a: the structure that is used for all the TCO design-related simulations. b: the structure that is used within the spectrophotometric measurements and the simulations for the model validation.

The deposition information of the AZO and ITO samples found the have the best performance using the above-described metric, are shown in table 4.2. The n and k values of these will be used from now on as the material-specific simulation input parameters for aluminum-doped zinc oxide and indium-doped tin oxide respectively. The n and k values are shown in figure 4.3. The n and k show similar results for AZO and ITO, which is expected. It can also be seen that the k trends in the visible and NIR region for AZO and ITO are higher than for IOH and i-ZnO, which is also as expected. For the blue region, the k trends of AZO, ITO, and IOH are similar, while the k trend for i-ZnO is significantly higher.

4.2.3. Validation

To validate the use of the n and k values determined by SE and the model used in GP4, the R, and T are calculated for each TCO complex refractive index using the layered structure shown in figure 4.4b. Only for this subsection, the TCO coating will be simulated on top of the glass substrate as this is the way that the spectrophotometric measurement of R and T is done using the Lambda equipment. The simulated R and T values are compared with the measured R and T. The results for each sample can be found in figure 4.5. It can be seen that the simulated and measured trends are found to be very similar. For ITO and AZO, some interference shifts are found due to the thickness inhomogeneity of the sample and because the SE, R, and T measurements are not done at the exact same spot on the sample. Furthermore, for AZO a significant difference in T can be found from about 1000 until $1200 nm$. Here the SE data seems to represent a lower absorption than the measured R and T represent. The figure for IOH shows a very good agreement with the measurement for the NIR region. This shows that the spectrophotometric most likely also underestimates the absorption in the NIR region.
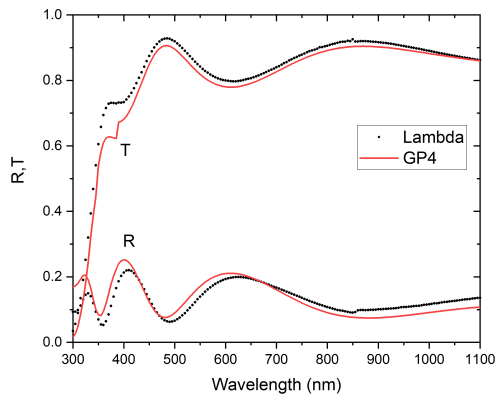
(a) ITO validation
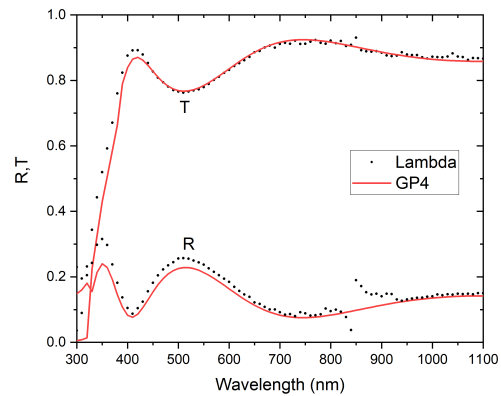
(b) IOH validation
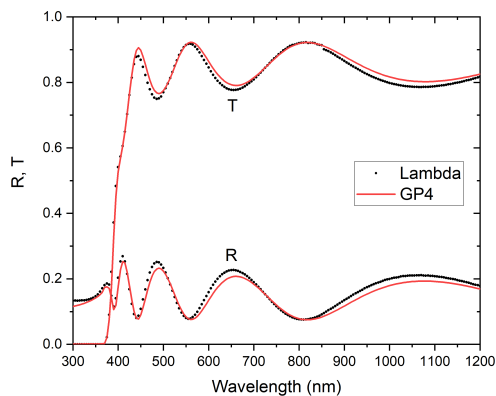
(c) i-ZnO validation
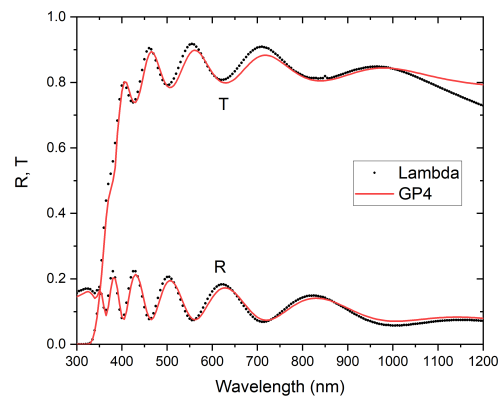
(d) AZO validation

Figure 4.5: The validation of the simulation model and used n, and k values calculated with SE by comparing the simulated R and T values with the via SP measured R and T values. a: validation for the ITO sample, b: validation for the IOH sample, c: validation for the i-ZnO sample, and d: validation for the AZO sample.

4.3. Solar cell design

The layered structure of the tandem solar cell, that will be used within this chapter, is shown in figure 4.6a. For every material used in the simulations with GenPro4, a material characteristic input is needed. These materials' characteristic inputs are the complex refractive index values dependent on the wavelength. In the previous section, it is shown which N values are used for the TCO materials: AZO, ITO, IOH, and i-ZnO. The N values from the GenPro4 database are used for the materials on which the focus of this research is not: glass, nc-SiOx (p), a-Si (i), nc-SiOx (n), Ag, Al, and air. Within GenPro4, layers can be modeled as a coating to take into account interference, or as a layer, when interference effects can be neglected. A more detailed explanation of the use of coating and layer models can be found in section 2.4.2. For the simulations, the air will be modeled as an infinite layer. As the glass substrate is much thicker than the coherence length of light, and therefore, interference will not play a role, the glass substrate will be modeled as a layer. Interference also plays less of a role when the absorption is high. Therefore, the absorber layers, intrinsic a-Si, and intrinsic nc-Si, are also modeled as layers. For all the other layers, interference plays an important role, and the other layers will therefore be modeled as a coating. In the remainder chapter the 'coatings' will still be addressed as layers. Within this section, the focus will lay on the design of the two TCO layers indicated in the solar cell structure.

Front contact   For the TCO coating under the glass substrate (front contact TCO layer), a new bi-layer design consisting of IOH and i-ZnO sublayers will be compared to the standard AZO and ITO single-layer front contacts. Kalpoe et al. found that a combination of IOH, providing good electrical properties, and i-ZnO, inducing low parasitic absorption, provides a TCO layer containing both good optical properties and electrical properties that could exceed that standard single AZO and ITO layers. They found higher mobility values for the bilayer than for the individual IOH layer [17]. The structure of the bi-layer (on glass substrate) can be found in figure 4.6b.

(a) Solar cell   (b) Bi-layer
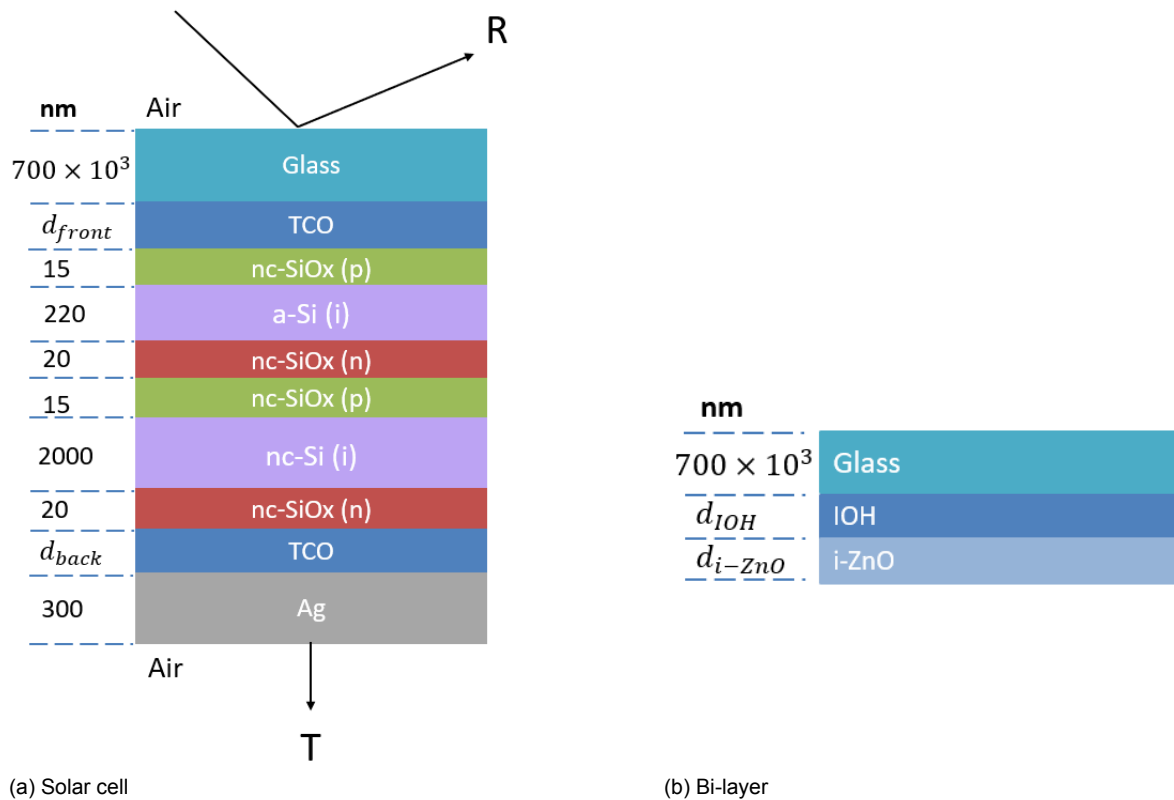
Figure 4.6: a: a schematic of the solar cell structure used within this chapter. d_{front} is the total thickness of the front TCO layer, and d_{back} is the thickness of the back TCO layer. b: a schematic of the IOH/i-ZnO bi-layer structure where d_{IOH} is the thickness of the IOH layer and d_{i-ZnO} is the thickness of the i-ZnO layer.

Back reflector   For the TCO layer on top of the silver back contact, the i-ZnO material is compared with the more standard-used AZO material in terms of the optical performance of the solar cell. The light arriving at the back TCO back reflector layer will mostly contain wavelengths of the NIR region. i-ZnO is a non-doped material, while AZO is an aluminum-doped material. It is therefore expected that i-ZnO has lower charge carrier densities than AZO. Due to the lower N_e, i-ZnO will have less FCA in the NIR. Therefore, it is investigated using optical simulations from GenPro4, if the i-ZnO back reflector layer will indeed result in a better optical response of the solar cell than the standard-used AZO back reflector layer. Furthermore, as a lot of solar cells use an aluminum back contact instead of silver, a short comparison between aluminum and silver as metal back contact is done. The complex refractive index values of the TCO layers are determined with one of the characterization methods discussed in the previous chapter, this will be discussed in section 4.2.

This section first focuses on the optimization of the back reflector and investigates the influence of texturing and simulation models on the effect of the back reflector designs. Then, the section will continue with the already optimized back reflector and focus on the front contact designs.

4.3.1. Texturing, simulation model, and the back-reflector

The purpose of this subsection is to find the best back reflector design in terms of the solar cell optical response. As the performance of a back reflector design is dependent on the textures at the interfaces of the solar cell layers, the back reflector designs are compared using different textures. Furthermore, the influence of the simulation model on the effect of the texturing is analyzed.

Types of texturing

As explained in chapters 1, and 2, the surface texturing at the interfaces of the solar cell layers plays a big role in the light-absorbing performance of the intrinsic layers. To see the effect of texturing with different features, three different textures are applied to the simulations. One texture with nano features, 'Asahi U-type' texturing, one with micro features and developed at HyET solar, 'Flam01' and one microfeature texture that is optimized by Apte et al. for the backreflector of a nc-Si single junction thin film solar cell, 'E.Z.500e' [1]. The visualization of these textures can be found in figure 4.7 and information about their root-mean-square height, σ_{RMS}, their surface correlation length, L_c, and AR, can be found in table 4.3.

Texturing	$\sigma_{RMS}(nm)$	$L_c(nm)$	$AR\%$	Model
Asahi U-type	40	175	22.9	wave
Flam01	233	2270	10.2	ray
E.Z.500e	309	1893	16.3	ray

Table 4.3: The root-mean-square surface roughness, $\sigma_{RMS}(nm)$, the surface correlation length, $L_c(nm)$, and the aspect ratio, $AR\%$, for the three different textures used for the thin film solar cell simulation, determined by an atomic force microscope.

Asahi U-type   The Asahi U-type texturing is a commercially available texturing type with nano features [34]. This texturing was developed on the TCO material: fluorine doped tin oxide to enhance the light trapping of a-Si solar cells [34]. A visualization of this texture is shown in figure 4.7a. Within the simulation, the light illuminates from above, and the texturing is oriented as if it was made on the glass substrate. As the wave model in GenPro4 is validated for Asahi U-type textures, the wave model will be used for the simulations with the Asahi U-type texturing.

Flam01   Texture developed by Limodio et al.[21]. This texture is created by etching Aluminum foils in a $KOH:H_2O$ diluted solution. A visualization of this texture is shown in figure 4.7b. Within the simulation, the light illuminates from above, and the texture is oriented as if it is created on the metal back reflector of the solar cell. As this texture has a surface correlation length in the order of micrometers, it is assumed that the ray model within GenPro4 will model this texture more accurately than the wave model. Therefore, the ray model will be used in combination with the E.Z.500e texture.

E.Z.500e   E.Z.500e is a texturing developed by Adwait [1] for the optimization of the back-reflector of a nc-silicon thin film solar cell. The texturing was made by etching away AZO from a glass substrate using a 0.5% hydrochloric acid solution [1]. A visualization of this texture is shown in figure 4.7c. Within the simulation, the light illuminates from above and the texture is oriented as if it were made on the glass substrate. As this texture has a surface correlation length in the order of micrometers, it is assumed that the ray model within GenPro4 will model this texture more accurately than the wave model. Therefore, the ray model will be used in combination with the E.Z.500e texture.

Influence of the model

The 'wave' and 'ray' models are each validated for different texture structures. As explained in section 2.4.2, the wave model is mostly validated for textures with features of $100nm$ or lower, and the ray model is mostly validated for micro textures. For textures with features in between those boundaries, a more accurate model is still in development. For those textures, the results of the simulations will come with an error due to the model used. To see what the influence of both models is on the textures, the J_{ph} of and absorptance in the $a-Si$ and $nc-Si$ layers are compared for Asahi U-type, FB, and EZ500e texturing simulating with wave model, and for Asahi U-type, FB, Flam01 and EZ500e texturing simulated using ray model. For these simulations, the solar cell structure shown in figure 4.6a, is used

(a) Asahi U-type

(b) Flam01   (c) E.Z.500e
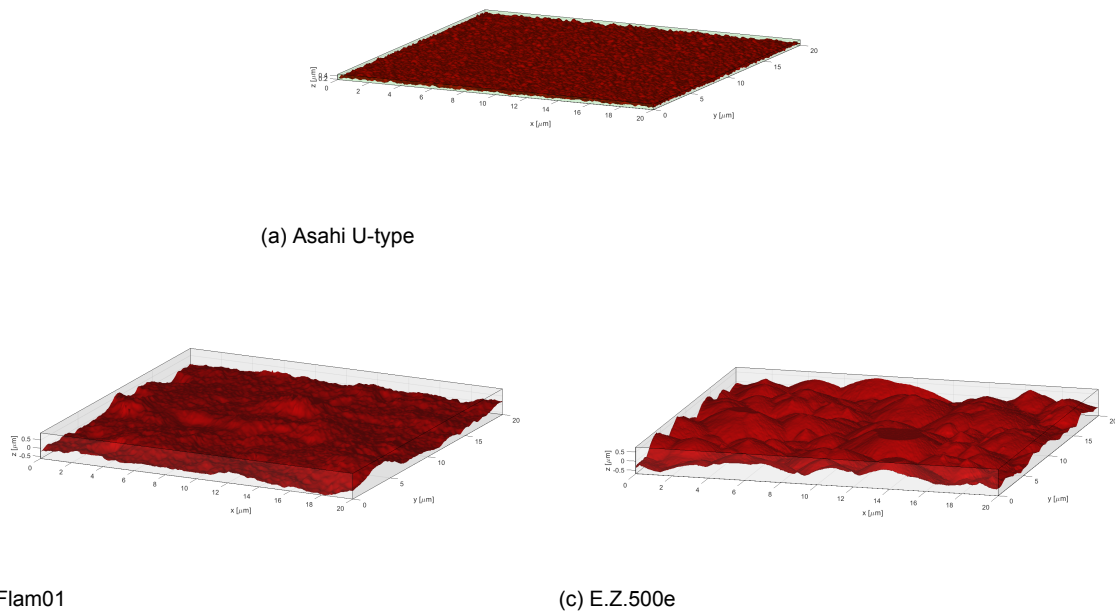
Figure 4.7: The three textures used for the thin film solar cell simulations: Asahi U-type, Flam01, and E.Z.500e. Shown in figures a, b, c, respectively.

with the bi-layer, $d_{IOH} = 100nm$, and $d_{i-ZnO} = 500nm$, as front contact TCO layer, and a back reflector design of an i-ZnO layer with $d_{back} = 80nm$ on top of the silver metal contact. The reflectance and absorption in the back reflector are also analyzed. The results are shown in figure 4.8.

Wave   For the textures simulated using the wave model, it can be clearly seen that the features of the texturing don't have any influence on both the J_{ph} and the absorptance values. This indicates that the wave model, whatever texturing is applied, sees the interfaces as having the same textures and suggests that the model sees the interfaces as almost flat. To check if these results indeed indicate the modeling of (almost) flat surfaces, the same solar cell structure is simulated without the application of texturing using the 'flat' model. The results in absorptance in the absorber layer and the back reflector, and the reflectance are shown in figure 4.8a, and the results in J_{ph} are shown in figure 4.8c, together with the wave-model-simulated results. It can be seen that the difference between the wave-model-simulated J_{ph} and the flat-model simulated J_{ph} is very small, lower than $0.01 mA/cm^2$. This shows that the wave model indeed models every texturing to be "practically" flat. This little difference between wave and flat is expected as within the model, the total reflectance and transmittance (spectral + diffused) are assumed to be equal to the reflectance and transmittance of a flat surface, as explained in section 2.4.2. Therefore, the only difference between the flat and textured surface will be the secondary reflections internally in the solar cell layers. How much secondary reflections will occur depends on the amount of diffused reflectance and transmittance. It is also explained that the diffused transmittance increases with the increase in σ_{RMS}, therefore it is interesting to see that the results in J_{ph} for the micro textures, are not to be found higher than for the Asahi U-type texture. It could be that in this case the difference calculated is too small to notice.

As we can assume the wave model to be accurate for the Asahi U-type texturing due to its small features, with these results we can also conclude that the wave model is not the correct model for the other textures.

Ray   The simulations that were done with the ray model show, in contrast to the wave-model simulations, significant differences in J_{ph} between the different textures. This is shown in figure 4.8d and makes sense, as explained in section 2.4.2, the ray model calculates the total reflectance and transmit-
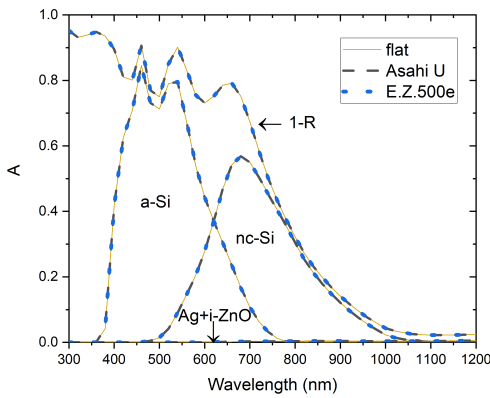
(a) Wave + flat
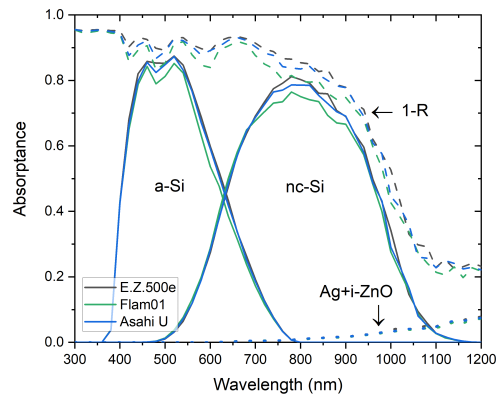
(b) Ray
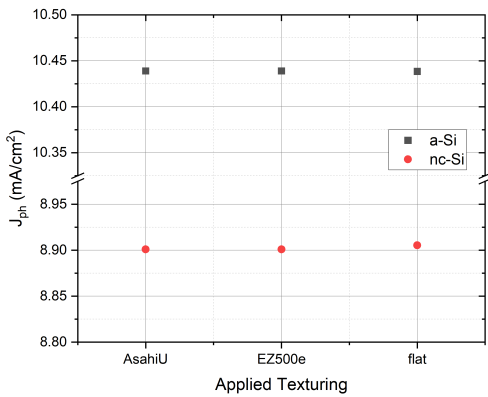
(c) Wave + flat
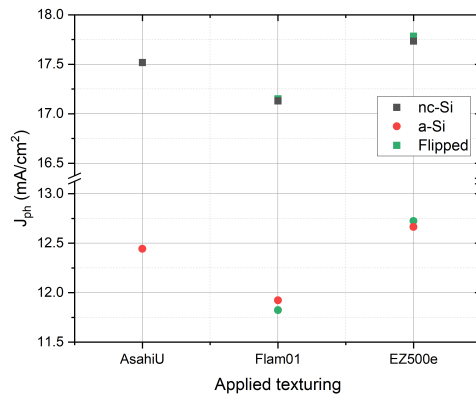
(d) Ray

Figure 4.8: (a),(b): the results of the absorber layer absorptance, the reflectance, and the absorptance in the BR for the solar cell simulations for the three textures simulated using the wave and flat model, and the ray model respectively. (c),(d): the results of the absorber layer J_{ph} for the solar cell simulations for the three textures simulated using the wave and flat model, and the ray model respectively.

tance (spectral + diffused) for every interface dependent on the texturing. The rays at a certain interface are simulated by recording the AID of the reflectance and transmittance at every interface for a certain amount of incident angles. The AID, therefore, depends highly on the texture, as explained in section 2.2.4. The interesting result that figures 4.8b, and 4.8d show is that the Asahi texturing is found to have a higher result than the Flam01 texture in both the absorptance in the absorber layers and the J_{ph} in the absorber layers. When comparing the three textures and their results in absorptance in the absorber layers and the J_{ph} in the absorber layers, a relation can be found between these parameters and the AR of the textures. The absorptance and J_{ph} in the absorber layers seem to increase with increasing AR. This makes sense as the AR is a measure of quantifying how dense the texturing is. A denser texture has more, and/or larger features in a smaller area, and will therefore induce more scattering per unit of area. Although, in reality not only the AR ratio is important in the scattering effect, but also the σ_{RMS}, and the L_c. The Asahi U-type texture has an σ_{RMS}, and L_c, the order of tens of nanometers, and will therefore, in reality, have too small features to have a significant effect on the scattering and absorptance in the absorber layers (as shown by using the validated wave model).

Texture orientation   As the three textures are simulated using different orientations, the effect of the orientation is analyzed. Simulations are done for the Flam01, and E.Z.500e texturing using the opposite (180°) orientation from the orientation described in section 4.3.1. The results in J_{ph} are shown in figure

4.8d (green data points). It can be seen that for both textures a difference is found in J_{ph}, but, in the comparison of the two textures, this difference does not matter that much. Therefore, this difference is not important for the rest of this research and will not be explored any further.

Model offset   The purpose of this subsection was to analyze the influence of the two simulation models on the results in absorptance and J_{ph} in the absorber layers. It is found that the wave model shows no difference in results between the different textures. The ray model was found to give high values in J_{ph} in the a-Si and nc-Si layers for the Asahi U-type texture compared with using the wave model that is validated for Asahi U-type textures (about $3.5 mA/cm^2$, and $5 mA/cm^2$ higher in J_{ph} for a-Si, and nc-Si, respectively). It is known that the higher outcome for the ray model is not realistic and it can be stated that the ray model, therefore, for nano-featured textures, with a relatively high AR induces a certain unrealistic offset on the absorption in the absorber layers. As in the remainder of this chapter, the textures Flam01 and E.Z.500e are simulated using the ray model, while their σ_{RMS} values are in the range between nano, and micro-features, a possible offset and therefore error in the results has to be kept in mind.

A comparison in texture and back reflector design

The different textures described, and the insight gained on the influence of the simulation models on the results in absorptance and J_{ph} are used in the comparison of the different back reflector designs in terms of TCO material and the optimization of these designs in terms of TCO layer thickness. First, the back reflector designs compared for this analysis will be described.

Back reflector designs   Four different back reflector (BR) designs are compared. These designs are shown in figure 4.9. The first design does not contain any BR layers, the second design only contains a silver back contact with a thickness of $300 nm$, the third design consists of an AZO layer on top of the silver back contact, and the fourth consists of an i-ZnO layer on top of the silver back contact. The first two designs are compared to see the influence on the thin film solar cell optical response of the highly reflective silver. The second, third, and fourth design are compared to see the influence on the thin film solar cell optical response when adding a TCO layer on top of the silver back contact. Furthermore, the third and fourth design are compared to see if the use of an i-ZnO back reflector layer will result in an enhanced thin film solar cell optical response, compared to the use of the standard AZO back reflector layer.
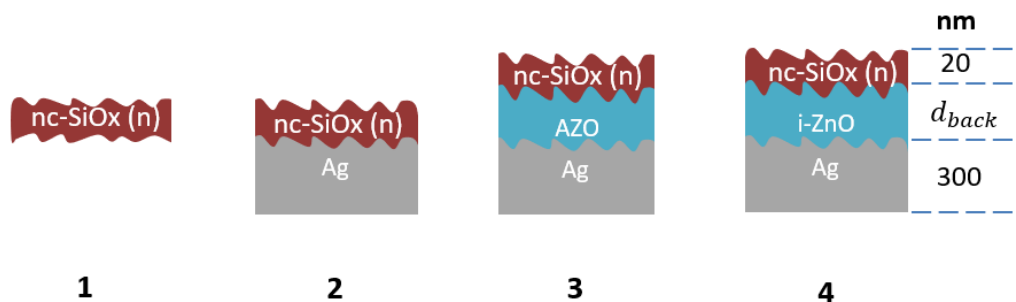
Figure 4.9: A schematic of the four different back reflector designs that are compared in section 4.3.1.

Texture comparison   Simulations are done for the designs shown in figure 4.9, for both an IOH/i-ZnO bilayer as front contact and for all three textures described previously. The following thickness specifications are used: $d_{bilayer} = 600 nm$ with $d_{IOH} = 100 nm$ and $d_{i-ZnO} = 500 nm$, and $d_{back,TCO} = 80 nm$. The J_{ph} for a-Si and nc-Si for these different solar cell structures, applying Asahi U-type, Flam01, and EZ500e texturing, is shown in figure 4.10a. It can be seen that for all the BR designs, of the three textures, E.Z.500e induces the highest J_{ph} in both absorber layers. Flam01 induces the second highest J_{ph}, and Asahi U-type the lowest. This trend is also found for the absorptance values for the top and

bottom absorber layer shown in figure 4.10b. This figure contains furthermore the $1 - R$, and absorptance in the BR in the case of BR design 4. The figure shows that the textures with lower absorptance in the absorber layers have a higher reflectance but lower absorptance in the BR. For the absorptance in the BR, it has to be kept in mind that GenPro4 does not have a model included for plasmonic absorption in the silver back contact. Plasmonic absorption occurs in silver when the surface is rough. It has to be kept in mind during this chapter that due to the lack of plasmonic absorption in the simulation model, the absorptance values found for the BR throughout this chapter can be underestimated. This also results in possible overestimation of the reflectance. In literature, it is found that the plasmonic absorption increases with the aspect ratio of the rough surface... From the results that were described in this paragraph it could be concluded that the E.Z.500e texture scatters light more effectively than the Flam01 texture. But, as E.Z.500e has a higher AR, in reality, it could be that the E.Z.500e texture induces a higher plasmonic absorption and therefore less absorptance in the absorber layers than found with the GenPro4 simulations. The next paragraphs go into more detail about the differences in the optical response of the solar cell for the different BR designs focused on the Asahi U-type texture and the E.Z.500e texture.
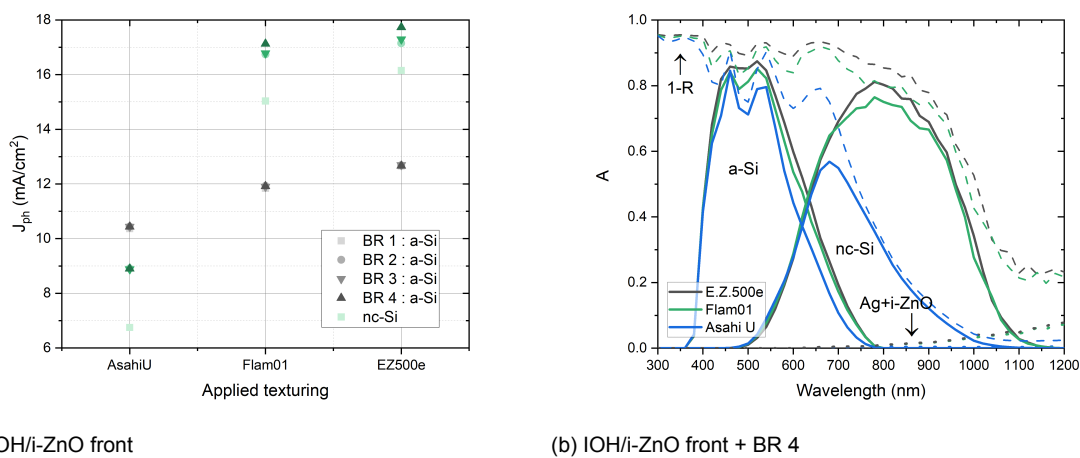
(a) IOH/i-ZnO front

(b) IOH/i-ZnO front + BR 4

Figure 4.10: (a): the results of the absorber layer J_{ph} for the solar cell simulations for the three textures. (b): the results of the absorber layer absorptance, the reflectance, and the absorptance in the BR for the solar cell simulations for the three textures.

Asahi U-type   Figure 4.11a, shows the results in absorptance and J_{ph} for both the top and bottom cell absorber layers for the simulations using the Asahi U-type texture and bi-layer front contact design. Comparing the results for BR design 1 (no BR), and BR design 2 (Ag BR), it can be stated that adding the silver metal back contact improves the optical response of the solar cell highly by increasing the absorptance in the bottom absorber layer. The difference in bottom cell J_{ph} for BR 1 and 2 is found to be about $2.2 mA/cm^2$. In figure 4.11b, the n, and k values of n-doped nc-SiOx, AZO, i-ZNO, and Ag, can be found. It can be seen that the difference in both n and k between the n-doped layer and the silver back contact in the solar are significantly high. Fresnel formula 2.9, indicates that the reflectivity at the interface between two media increases if the difference between n, and k od those two media increases. From this, it can be expected that adding the silver back contact to the n-doped layer, increases the reflectivity significantly, and therefore the absorption in the absorber bottom absorber layer. Adding a TCO layer on top of the silver back contact, BR designs 3 and 4, has very little effect and even lowers the J_{ph} in the absorber layers. This little and negative influence of the TCO layers is as expected as the Asahi U-type texturing gives results similar to a flat surface. Therefore, the light scattering will be minor and the light trapping performance will mostly be influenced by the difference in n and k values between the n-doped layer and the TCO back-reflector layer. As shown in figure 4.11b, these differences in n and k are not significant and therefore, the effect of the little improvement in light trapping will be canceled by the effect of absorption in the TCO back-reflector layer.
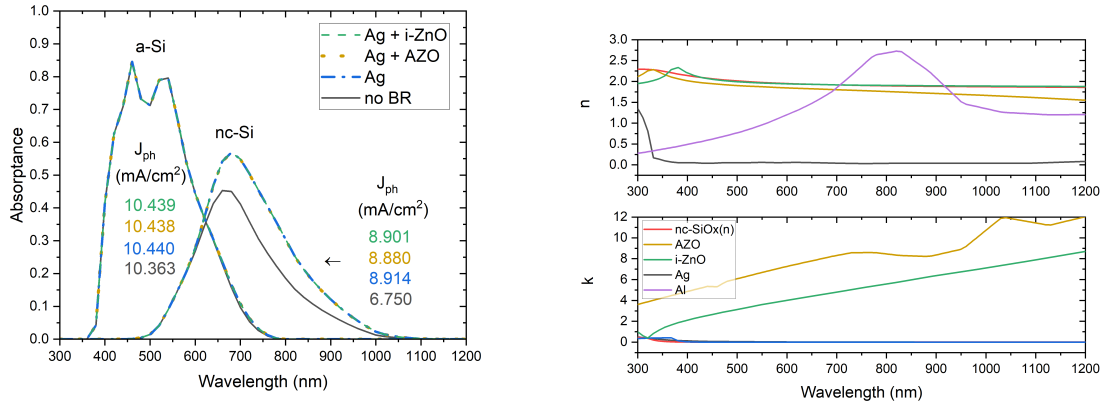
(a) Asahi U-type + IOH/i-ZnO front   (b) Complex refractive indexes

Figure 4.11: (a): the results of the absorber layer J_{ph} and absorptance for the solar cell simulations for the different BR designs using Asahi U-type texturing. (b): the n, and k values for n-doped nc-SiOx, AZO, i-ZnO, Ag, and Al.

E.Z.500e   For the E.Z.500e texturing, a clear increase in J_{ph} for the bottom absorber layer is found when comparing from BR 1 until BR 4. This can be seen in figure 4.12b. Furthermore, in figure 4.12a, the same trend can be found for the absorptance in the bottom cell. This figure also shows the absorptance in the BR and the reflectance. The higher absorptance in the back reflector found for BR 3, compared to BR 4, indicates that AZO absorbes more light than i-ZnO in the NIR wavelength region. This is expected as the i-ZnO was found to have a significantly lower k trend in the NIR compared to AZO (figure 4.3). These results indicate that BR 4 induces a better solar cell optical performance than BR 3. The difference in J_{ph} between BR 4 and BR 3 was found to be about $0.5 mA/cm^2$. This shows that the optical response of a tandem thin film solar cell can significantly be improved by using an i-ZnO as a TCO back reflector layer instead of the commonly used AZO. As the top cell absorption is not significantly influenced by the different BR designs, it can also be stated that the back reflector designs mostly influence the longer wavelength for which the a-Si is transparent.
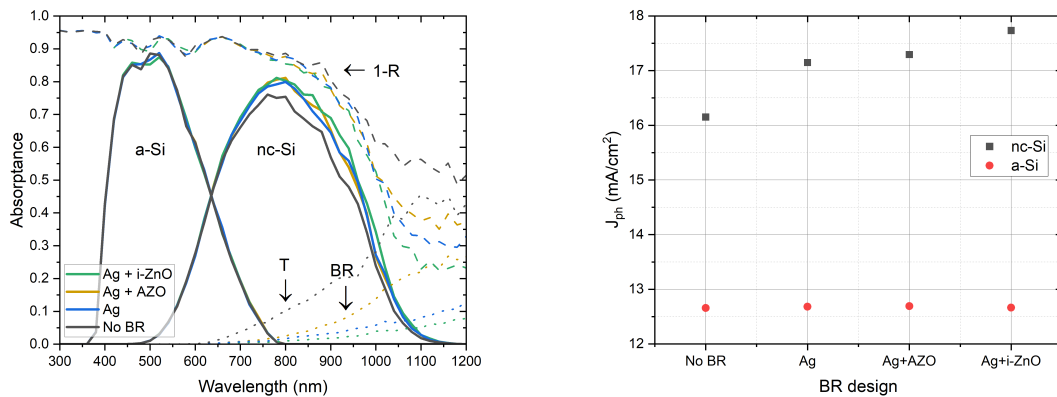
(a) Bilayer   (b) Bilayer

Figure 4.12: (a): the results of the absorber layer absorptance, the reflectance, and the absorptance in the BR for the solar cell simulations for the different BR designs using the E.Z.500e texturing. (b): the results of the absorber layer J_{ph} for the solar cell simulations for the different BR designs using the E.Z.500e texturing.

The influence of TCO layer thickness

To see if the thickness of the i-ZnO layer of the back-reflector influences the result in J_{ph}, simulations are done for the solar cell with the i-ZnO/silver back-reflector for a range in $d_{back,TCO}$ of 40 until $260 nm$

with a stepsize of $20nm$. These simulations are done for the bi-layer front contact design, and the AZO, and ITO front contact design. For the bi-layer front contact, the results in J_{ph} for the a-Si and nc-Si layers are shown in figure 4.13. The results for AZO and ITO can be found in chapter B of the appendix. The results show some dependence of the J_{ph} on the TCO BR layer thickness for both the top and bottom cell, although not that significant. Maximum J_{ph} differences of about $0.1mA/cm^2$ and about $0.2mA/cm^2$, for the top and bottom cell respectively. The best thickness regarding the J_{ph} in the top and bottom cell is chosen and indicated with a vertical green dashed line. The same was done for the results of the AZO, and ITO front contact designs. The best improvements in the absorptance in the active layers have been found for thicknesses $100nm$, $120nm$, and $140nm$, for AZO, ITO, and bi-layer front contact respectively.
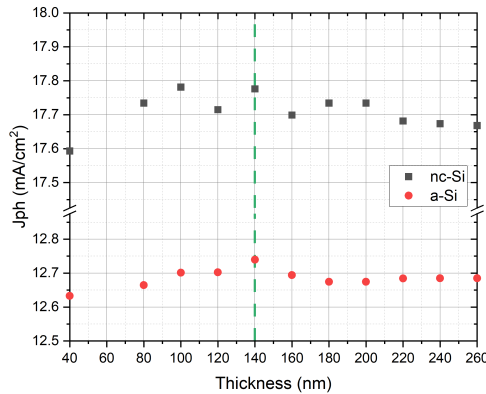
Figure 4.13: The results in the absorber layer J_{ph} for the solar cell simulations varying the i-ZnO layer thickness of BR design 4.

Silver vs Aluminum   As in many solar cells, aluminum is used as a back-reflector material instead of silver due to the lower costs and abundance, the difference in J_{ph} is analyzed for the different i-ZnO back-reflector layer thicknesses using silver and aluminum as back contact. The results are shown in figure 4.14 and show that the difference in J_{ph} between the BR with silver and the BR with aluminum is very significant for the bottom cell.
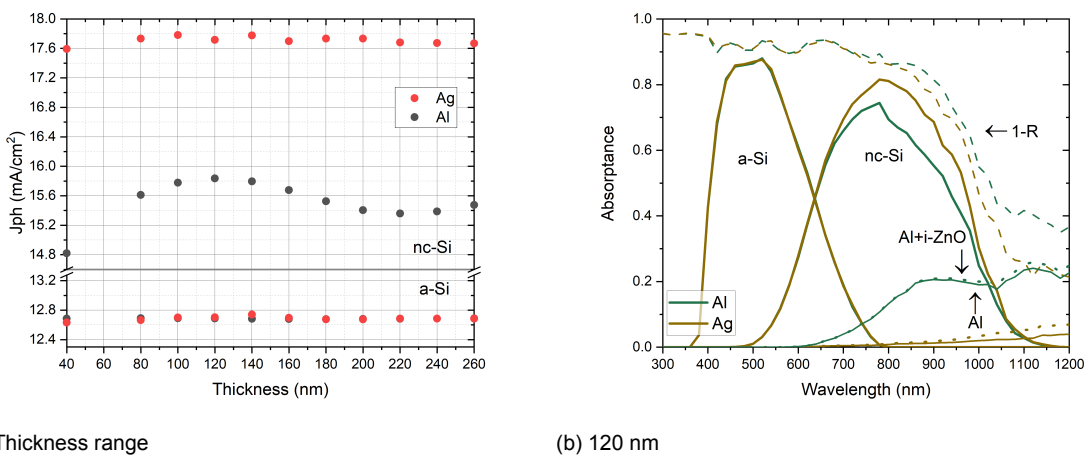
(a) Thickness range   (b) 120 nm

Figure 4.14: (a): The results in the absorber layer J_{ph} for the solar cell simulations varying the i-ZnO layer thickness of BR design with a silver back contact and the BR design with an aluminum back contact. (b): The results in the absorber layer absorptance, the reflectance, and the absorptance in the BR for the solar cell simulations varying the i-ZnO layer thickness of BR design with a silver back contact and the BR design with an aluminum back contact.

A difference of about $2mA/cm^2$ is found for the different layer thicknesses. This big difference is due to the optical properties of silver and aluminum. In figure 4.11b, the n and k values of aluminum are also shown and it can be seen that aluminum and the n-doped layer have a much lower difference in n compared to silver and the n-doped layer. Especially for the longer wavelengths. The difference in the top cell is not significant. Furthermore, it can be seen that for aluminum, the J_{ph} is much more dependent on the i-ZnO layer thickness. As aluminum is less reflective and has, therefore, less influence on the optical response of the solar cell, the role of the i-ZnO layer becomes more significant, and therefore, the interference behavior of the i-ZnO layer is clearly visible...

4.3.2. Front contact design

Now that an optimized design has been found for the back reflector, the influence of the front contact TCO layer will be further analyzed. Simulations are done for the solar cells with the optimized back-reflector for AZO, ITO, and the bi-layer front contact. The thicknesses of the TCO front contact layers are varied: d_{AZO}, and d_{ITO} are varied from 100 until $1600nm$, d_{IOH} from 50 until $600nm$, and d_{i-ZnO} from 200 until $1000nm$.

Bilayer

The results in J_{ph} for the top and bottom cell are shown in figures 4.15a and 4.15b respectively. For clarity, both figures have been given the same colorbar range of $1mA/cm^2$. The figures show that the increase in thickness of the i-ZnO layer has more influence on the photo-induced current for both the bottom and top cells. This is as expected as i-ZnO has a higher extinction coefficient for the short wavelengths (until about $450nm$) and for the longer wavelengths (from about $650nm$ until $1200nm$) compared to IOH (figure 4.3). For those wavelengths, i-ZnO absorbs more light, and therefore, fewer photons are left for the active layers to absorb. The change in J_{ph} for the bottom cell is found to be very small with a maximum difference of about $0.5mA/cm^2$. A good optical response seems to be found for the thickness ranges of 50 until $600nm$ for i-ZnO, and 50 until $600nm$ for IOH. Ofcourse, this analysis only includes te optical response and these ranges will be partly unrealistic when also including the electrical properties.

(a) a-Si   (b) nc-Si
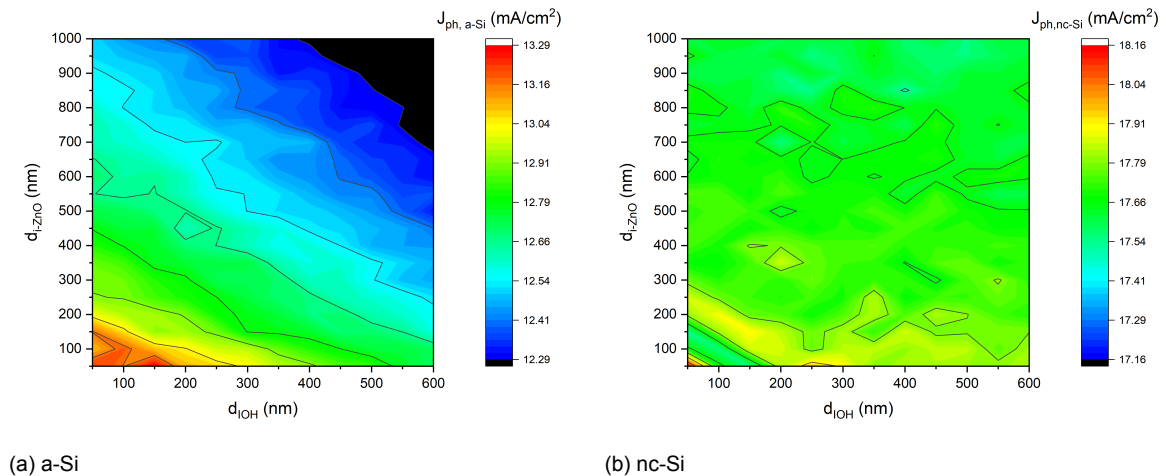
Figure 4.15: (a): The results of the top cell J_{ph} for the solar cell simulations varying the IOH and i-ZnO thickness of the bi-layer. (b): The results of the bottom cell J_{ph} for the solar cell simulations varying the IOH and i-ZnO thickness of the bi-layer.

Comparison with single layers

The results in J_{ph} for the IOH/i-ZnO thickness combinations that give a certain total bilayer thickness, $d_{bilayer} = d_{IOH} + d_{i-ZnO}$ are compared with the AZO and ITO results for which d_{AZO} and d_{ITO} are equal to $d_{bilayer}$. These results are structured using the Matlab [22] script that can be found in chapter C in the appendix. Figure 4.16a shows these results for the AZO, ITO, and the bi-layer front contact.
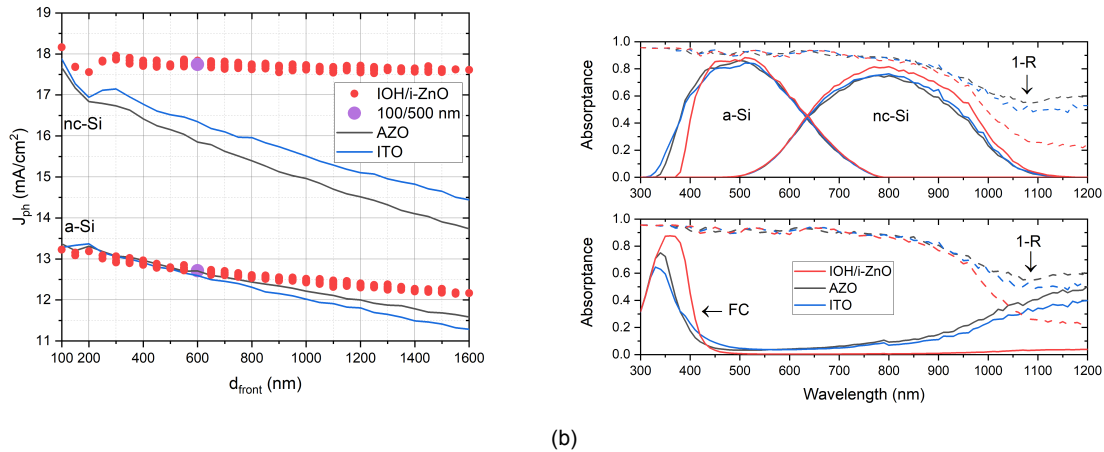
Figure 4.16: (a): The results of the top cell and bottom cell J_{ph} for the solar cell simulations varying the bi-layer, AZO, and ITO front contact thicknesses.(b): the absorptance in the absorber layer, and the FC, and the reflectance for the solar cell simulation with the bi-layer, AZO, and ITO FC and $d_{front} = 600nm$.

The results show that in this case, the IOH/i-ZnO bilayer is a big improvement compared to the AZO and ITO single layers. Especially from a total thickness of about $600nm$ where the bilayer shows a higher J_{ph} for both the top and bottom cell. Due to the significantly lower extinction coefficient of IOH and i-ZnO, compared to AZO and ITO for the NIR region, more light containing longer wavelengths is left to absorb for the absorber layers. Therefore, the bi-layer follows a less steep trend with thickness than AZO and ITO and that's why the improvement of the bi-layer compared to a single layer becomes more significant with the increase in thickness.

To see the influence of the parasitic absorption in the front contact TCO layers, the absorptance in the front contact layers together with the reflectance and the absortance in the absorber layers are shown in figure 4.16b for AZO, ITO and IOH/i-ZnO with $d_{front} = 600nm$, $d_{IOH} = 100nm$, and d_{500nm}. It can be seen that from $300 - 440nm$, the bi-layer absorbes significantly mor light than both single layers, but from $440nm$ and higher the bi-layer absorbs less than the single layers. It can be seen from figure 4.16a, where the bilayer with $d_{IOH} = 100nm$, and $d_{i-ZnO} = 500nm$ is indicated with a bigger purple dot, that the J_{ph} of the top cell are similar for the bi-layer and single layers. The J_{ph} for the bi-layer in the bottom cell, on the other hand, is found to be about $1.6mA/cm^2$ higher than for ITO, and about $2mA/cm^2$ higher than for AZO. So due to the lower parasitic absorption from about $440nm$, the bi-layer will still arrive at a better performing solar cell than the single layers (when in current matching conditions) despite the higher absorption at the short wavelengths.

Focussing on the absorptance in the absorber layers, it can be seen that the change in front contact material has influence on the absorptance of both the short and the long wavelengths and therefore on both the top and bottom cell. While, for the in the previous section, we saw that the back reflector only influenced the longer wave lengths and therefore only the absorptance in the bottom cell. For the absorptance in the top cell, the bi-layer induces a significantly lower absorptance than the single layer from 300 until about $440nm$ and a slightly larger absorptance at around $500nm$. Due to the solar irradiation peak at around $500nm$, the slightly higher absorptance for the bi-layer at $500nm$ as more onfluence on the J_{ph} than the significant lower absorptance from $300 - 440nm$. As for the large wavelengths, the parasitic absorptance is found to be significantly lower for the bi-layer, the reflectance is found to be significantly higher for the larger wavelengths.

4.4. Comparison ITO and bi-layer front contact

The eventual goal in optimizing the front contact and back reflector layers within a solar cell is to increase the efficiency of the solar cell. The optical response of the several solar cell designs can not solely tell us which solar cell design would eventually result in the highest efficiency. For this, an analysis of the

d (nm)	Design	$J_{ph,a-Si}(mA/cm^2)$	$J_{ph,nc-Si}$	d_{a-Si} (nm)
600	ITO	14.5	14.5	445
	IOH/i-ZnO	15.2	15.3	525
240	ITO	15.2	15.1	444
	IOH/i-ZnO	15.4	15.4	496

Table 4.4: The current matching J_{ph} and d_{a-Si} values for several front contact designs.

electrical properties is needed in addition. A thorough investigation of the electrical performance of the solar cell designs lies without the scope of this research, as well as the calculation of efficiencies. But, to still get an idea of the eventual total performance of a bi-layer design compared to a single-layer design, the electrical properties already available have been taken into account. The ITO sample used within this chapter comes from a stack of 4 samples for which only the deposition power is adjusted. Sample 3kA had the highest performance and therefore it is assumed that this material has the highest performance at the film thickness of sample 3kA, $d_{ITO} = 240nm$. To compare this single-layer design with the bilayer, the following thicknesses will be used for the bilayer: $d_{IOH} = 40nm$, $d_{i-ZnO} = 200nm$. Furthermore, from experimental research, it was found that the bilayer with $d_{IOH} = 100nm$, $d_{i-ZnO} = 500nm$ has very good electrical properties [17]. Therefore this bilayer design is compared with an ITO single-layer design with $d_{ITO} = 600nm$. To get a more clear idea of how much the photo-induced current between the solar cell design with ITO front contact and the solar cell design with bilayer front contact is, the layer thickness of the intrinsic a-Si layer is varied in a simulation for both the solar cell designs to get the matching photo-currents. This minimization problem is solved using the Matlab [22] function 'fminsearch' and the code used can be found in chapter C of the appendix. In table 4.4, the results of the a-Si layer thicknesses and matching photo-currents can be found for the solar cell designs.

It can be seen that the bilayer of $600nm$ results in a photo current matching value of about $0.7mA/cm^2$ higher than the ITO single layer of $600nm$. From wat we saw in the previous section, this makes sense as for the bi-layer the total J_{ph} (top + bottom cell) for decreases with a less steep slope with layer thickness than ITO. For d_{240nm}, the difference in current-matched J_{ph} is only about $0.2mA/cm^2$. The most insightful aspect of the results, is the difference in J_{ph} between the best ITO front contact layer design ($d_{front} = 240nm$) and the best bi-layer front contact layer design $d_{front} = 600nm$. The difference in J_{ph} is in this case found to be not significant. Both designs result in a J_{ph} of about $15.22mA/cm^2$. This indicated that in this case, from the optical side of view the IOH/i-ZnO bilayer would not be a better choice than the ITO single layer. Especially when keeping in mind that the FCA for the IOH sample is most likely underestimated during this analysis.

4.5. Conclusion

The main objective of this chapter is: Compare the optical response for the design of the front contact layer in a tandem thin-film silicon solar cell for a new IOH/i-ZnO combined bi-layer with the standard AZO, and ITO single layers to find the best TCO front contact layer, and compare the optical response for the design of the back reflector in a tandem thin film solar cell for i-ZnO as back reflector TCO material with the standard AZO back reflector TCO material to find the best back reflector design.

Front contact

For non-current-matching conditions, it was found that the bi-layer, compared to both single layers, enhances the absorption in the bottom cell significantly. The slope of the decrease in J_{ph} in the bottom cell with the increase in total front contact thickness was found to be small for the bi-layer, compared to the single layers: a change of about $0.5mA/cm^2$ compared to a change of about $3.5mA/cm^2$ for ITO, and $4mA/cm^2$ for AZO, for a change in thickness of $1500nm$. This is due to the low parasitic absorption in the NIR region in the bi-layer, compared to the single layers. FCA absorption for IOH was found to be underestimated within the analysis, therefore the improvement in the optical response of the thin film solar cell for using the bi-layer instead of the single layers is assumed to be too optimistic. When comparing the optically and electrically optimized single ITO layer with the optically and electrically optimized bi-layer for current-matching conditions, the same J_{ph} in the absorber layers were found at about $15.2mA/cm^2$. Keeping in mind that the parasitic absorption in the bi-layer is underestimated, the bi-layer was not found to be a better front contact layer optically speaking.

Back reflector

It was found that an i-ZnO TCO back reflector layer on top of the silver back reflector enhances absorption in the absorber layer to a higher extent than an AZO TCO back reflector layer on top of a silver back reflector. A difference in J_{ph} of about $0.5mA/cm^2$ was found in the bottom cell for non-current matching conditions. This is because i-ZnO has lower parasitic absorption than AZO in the NIR wavelength region.

5

Conclusion

5.1. Conclusions

This chapter underlines the main conclusions found within this research. The main objectives of this report are:

- Compare commercially used methods, spectroscopic ellipsometry, and spectrophotometry + SCOUT, for determining the complex refractive index of TCO films with new methods using spectrophotometry + GenPro4 and photothermal deflection spectroscopy + GenPro4 to build a guide for the optical characterization of TCO films.

- Compare the optical response for the design of the front contact layer in a tandem thin-film silicon solar cell for a new IOH/i-ZnO combined bi-layer with the standard AZO, and ITO single layers to find the best TCO front contact layer, and compare the optical response for the design of the back reflector in a tandem thin film solar cell for i-ZnO as back reflector TCO material with the standard AZO back reflector TCO material to find the best back reflector design.

5.1.1. A guide on optical characterization

PDS has a very low absorption sensitivity ($\alpha = 10^{-6}$), compared to the other measurement techniques, and is not influenced by layer thickness. Therefore, PDS was assumed to be the most accurate for both thin and thick samples, and low and high absorption. As PDS can be a challenging measurement to do, other methods that show similar results to PDS are preferred. It was found, for materials with relatively high absorption profile ($k > 0.001$), so materials with a relatively high charge carrier density and/or an amorphous-like miro-structure, that SP + GenPro4 (+ applied negative A correction) can be used as a replacement of PDS + GenPro4 (under the condition that SP data does not contain negative values due to thickness inhomogeneity and/or detector switch). For this situation, SE could also be used if the exact shape of the k trend is less important.

5.1.2. TCO front contact and back reflector design

Front contact

For non-current-matching conditions, it was found that the bi-layer, compared to both single layers, enhances the absorption in the bottom cell significantly. The slope of the decrease in J_{ph} in the bottom cell with the increase in total front contact thickness was found to be small for the bi-layer, compared to the single layers: a change of about $0.5mA/cm^2$ compared to a change of about $3.5mA/cm^2$ for ITO, and $4mA/cm^2$ for AZO, for a change in thickness of $1500nm$. This is due to the low parasitic absorption in the NIR region in the bi-layer, compared to the single layers. FCA absorption for IOH was found to be underestimated within the analysis, therefore the improvement in the optical response of the thin film solar cell for using the bi-layer instead of the single layers is assumed to be too optimistic. When comparing the optically and electrically optimized single ITO layer with the optically and electrically optimized bi-layer for current-matching conditions, the same J_{ph} in the absorber layers were found at about $15.2mA/cm^2$. Keeping in mind that the parasitic absorption in the bi-layer is underestimated, the bi-layer was not found to be a better front contact layer optically speaking.

Back reflector
It was found that an i-ZnO TCO back reflector layer on top of the silver back reflector enhances absorption in the absorber layer to a higher extent than an AZO TCO back reflector layer on top of a silver back reflector. A difference in J_{ph} of about $0.5mA/cm^2$ was found in the bottom cell for non-current matching conditions. This is because i-ZnO has lower parasitic absorption than AZO in the NIR wavelength region.

5.2. Recommendations for future work

5.2.1. Optical characterization
From this research, it could not be investigated if PDS would still be the best method for samples containing a high surface roughness. There is not much literature that addresses the effect of surface roughness in PDS measurement. It was found that the scattering of the pump beam on the sample surface does have an influence on the measurement for glass and liquids [39],[37], but a more thorough investigation would be needed to see how this translates to the accuracy for measuring the absorption for thin film TCOs.

It was found that for the materials used within this report, PDS measurements would give the most accurate absorption profile of a thin film. PDS can be a complicated measurement though for which certain training is needed. To reduce the use of PDS measurements it would be worth the time to investigate the turning points more thoroughly: when to switch to PDS for low k. For SE it was found to be $k = 0.001$, but how does this translate to crystallinity and free charge carrier density? Furthermore, Spectrophotometry was also found to have a low sensitivity for low-absorbing materials, but the exact limit in k was not found. An investigation could be done, by comparing PDS measurements for different levels of crystallinity, surface roughness, and different levels of charge carrier densities with the SE and SE+SP+GP4 methods to see where the turning points are. Ideally, the goal of such an investigation would be to find one or two parameters that can indicate which method to use regarding all TCO materials. Crystallinity and charge carrier density would be a good start to investigate as they both have a significant influence on the absorption profile of a material.

5.2.2. TCO front contact and back reflector design
In the models used for the simulations, a single texture was applied to all the interfaces of the solar cell. In literature, it is found that, in reality, the texture applied at the first depositing step (the front) is not the same texture found at the last interface (the back) of the solar cell. The deposition of each layer causes changes in texturing. Therefore, to model the optical response of a thin film solar cell more accurately, for future research this change in texture should be taken into account.

Some phenomena that happen due to the features of the textures applied at the interfaces have not been taken into account within this research. A rough surface of the silver metal contact, for example, causes plasmonic absorption. This absorption is not yet implemented in the models of GenPro4, and therefore, the absorption in the silver contact is most likely underestimated within this research. A model for the plasmonic absorption should be developed to get more accurate results in the optical response. Another phenomenon that is neglected in this research is that textures can induce defects at the interfaces. These defects can reduce the open circuit voltage and the fill factor of the solar cell. A good model that takes into account these defects should be developed.

A
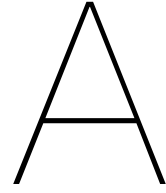
Sample information

This chapters gives more information on the samples used within this report.

Stack	AZO	Theater (C)	Tsubstrate (C)	t (s)	P (W)	$R_{sh,avg}(\Omega/sq)$
A	2	100	34,3	1543	300	132
	3	100	34,3	2571	300	65
	4	100	34,3	3600	300	37
B	5	200	95,4	514	300	1625
	6	200	95,4	1543	300	125
	7	200	95,4	2571	300	55
	8	200	95,4	3600	300	14
C	9	300	156,5	2571	300	30
	10	300	156,5	1543	300	70
	11	300	156,5	514	300	616
	12	300	156,5	3600	300	32
D	13	400	217,6	3600	100	319
	14	400	217,6	3600	200	37
	15	400	217,6	3600	300	19
	16	400	217,6	3600	400	-
E	17	300	156,5	3600	100	1287
	18	300	156,5	2700	200	108
	19	300	156,5	1800	300	77
	20	300	156,5	900	400	126
F	21	200	95,4	3600	100	278
	22	200	95,4	2700	200	82
	23	200	95,4	1800	300	75
	24	200	95,4	900	400	132

Table A.1: Information on the deposition parameters of the AZO samples together with the other stack labels and sheet resistance

Stack	ITO	Theater (C)	Tsubstrate (C)	t (s)	power (W)	anneal (C)	$R_{sh,avg}(\Omega/sq)$
A	3k A	25	24,03	3000	130	180	130
	4k A	25	24,03	4000	130	180	105
	5k A	25	24,03	5000	130	180	105
	6k A	25	24,03	6000	130	180	120
	7k A	25	24,03	7000	130	180	101
B	3k PA	25	24,03	3000	130	no	121
	4k PA	25	24,03	4000	130	no	115
	5k PA	25	24,03	5000	130	no	99
	6k PA	25	24,03	6000	130	no	95
	7k PA	25	24,03	7000	130	no	82
C	ito-1	25	24,03	5000	130	200	120
	ito-2	25	24,03	5000	130	250	198
	ito-3	25	24,03	5000	130	300	94
	ito-4	25	24,03	5000	130	350	123
D	ITO16	25	24,03	800	130	no	261
	ITO17	25	24,03	1200	130	no	200
	ITO18	25	24,03	1600	130	no	219
	ITO19	25	24,03	2000	130	no	178
E	ITO20	100	57,92	2000	135	no	132
	ITO21	100	57,92	1600	190	no	175
	ITO22	100	57,92	1200	245	no	197
	ITO23	100	57,92	800	300	no	261
F	ITO24	200	102,32	2000	135	no	160
	ITO25	200	102,32	1600	190	no	172
	ITO26	200	102,32	1200	245	no	136
	ITO27	200	102,32	800	300	no	199
G	ITO28	300	145,87	2000	135	no	237
	ITO29	300	145,87	1600	190	no	123
	ITO30	300	145,87	1200	245	no	143
	ITO31	300	145,87	800	300	no	194

Table A.2: Information on the deposition parameters of the ITO samples together with the stack labels and sheet resistance

Stack	IOH	T (C)	dep time (s)	p H2O (e-5 mbar)	Power [W]	Annealed (C)	$R_{sh,avg}(\Omega/sq)$
A	1	25	2000	3	105	130	37
	2	25	2000	3	120	130	23
	3	25	2000	3	130	130	19
	4	25	2000	3	150	130	15
	5	25	2000	3	165	130	16
	6	25	2000	3	180	130	14
B	1	25	2000	3	105	180	221
	2	25	2000	3	120	180	42
	3	25	2000	3	130	180	20
	4	25	2000	3	150	180	17
	5	25	2000	3	165	180	19
	6	25	2000	3	180	180	17
C	1	25	2000	3	105	200	38219
	2	25	2000	3	120	200	88
	3	25	2000	3	130	200	21
	4	25	2000	3	150	200	15
	5	25	2000	3	165	200	15
	6	25	2000	3	180	200	15
D	3	25	2000	3	130	250	
	4	25	2000	3	150	250	
	5	25	2000	3	165	250	
	6	25	2000	3	180	250	
E	8	100	1800	3	120	-	19
	9	100	1600	3	130	-	20
	10	100	1400	3	150	-	20
	11	100	1200	3	165	-	
	12	100	1000	3	180	-	21
F	13	200	2000	3	105	-	23
	14	200	1800	3	120	-	45
	16	200	1400	3	150	-	86
	17	200	1200	3	165	-	124
	18	200	1000	3	180	-	119
G	19	25	2000	1	105	-	25
	20	25	2000	2	105	-	27
	21	25	2000	3	105	-	35
	22	25	2000	4	105	-	30
	23	25	2000	5	105	-	34
H	24	25	1200	1	150	-	33
	25	25	1200	2	150	-	28
	26	25	1200	3	150	-	29
	27	25	1200	4	150	-	26
	28	25	1200	5	150	-	29
I	29	25	1400	3	150	-	28
	30	25	1000	3	150	-	43
	31	25	800	3	150	-	53
	32	25	600	3	150	-	76
	33	100	1200	1	150	-	58
	37	100	1200	5	150	-	30
J	38	25	2000	3	105		33
	39	25	2000	3	120		28
	40	25	2000	3	130		25
	41	25	2000	3	150		21
	42	25	2000	3	165		22

Table A.3: Information on the deposition parameters of the IOH samples together with the stack labels and sheet resistance

Stack	ZnO	T heater (C)	Tsubstrate (C)	dep time (s)	Power (W)	$R_{sh,avg}(\Omega/sq)$
A	1	250	125,95	3600	400	37993
	2	250	125,95	3600	300	1000931
	3	250	125,95	3600	200	184890
B	5	300	156,5	3600	400	175521
	6	300	156,5	3600	300	9622
	7	300	156,5	3600	200	2775236
C	9	300	156,5	2800	300	99691
	10	300	156,5	2000	300	22433593
	11	300	156,5	1200	300	34059
	12	300	156,5	400	300	7552
	13	350	187,05	3600	400	9372898
	19	400	217,6	3600	200	250244
	20	400	217,6	3600	100	50173
D	21	200	95,4	3600	400	1191278
	23	200	95,4	3600	200	error
	24	200	95,4	3600	100	442342

Table A.4: Information on the deposition parameters of the i-ZnO samples together with the stack labels and sheet resistance

Material	Label	T (C)	Time (s)	Power (W)	p H2O (e-5 mbar)	Annealing
AZO	A1	100	660	300	-	
IOH	H1	25	1100	150	3	
	H2	25	1100	150	3	215C for 30 min
i-ZnO	Z1	200	4200	200	-	

Table A.5: Information on the deposition parameters of the samples used for the PDS comparison, together with the stack labels and sheet resistance

B

Additional results chapter 4

This chapter gives a few results not shown in the main part of this report.

AZO	ϕ_H	$E_g(eV)$	$R_{sh}\left(\frac{Ohm}{sq}\right)$ at $100nm$	$T\_\{av\}$ for $d = 100nm$
2	0.49414	3.409	261.58	0.7858
3	0.49055	3.404	282.92	0.7852
4	0.50653	3.520	232.89	0.7977
5	0.42503	3.228	1247.24	0.7699
6	0.47135	3.438	300.55	0.7583
7	0.49738	3.339	220.86	0.7800
8	**0.56236**	3.683	**85.53**	**0.8147**
9	0.52754	**3.796**	118.91	0.7856
10	0.4995	3.460	162.66	0.7635
11	0.38498	3.446	4543.74	0.7766
12	0.51477	3.472	186.76	0.7960
13	0.51033	3.209	197.26	0.7927
18	0.499	3.681	212.19	0.7798
19	0.47858	2.298	195.71	0.7429
20	0.48122	3.298	249.85	0.7623

Table B.1: The results on the performance, ϕ_H, calculations for AZO.

ITO	ϕ_H	$R_{sh}Ohm/sq$	$T\_\{av\}$ for $d = 100nm$
ito-1	0.4745	432	0.7868
ito-2	0.4555	724	0.7885
ito-3	0.4850	338	0.7880
ito-4	0.4758	450	0.7916
3kA	**0.4954**	**312**	**0.7994**
4kA	0.4873	341	0.7923
5kA	0.4670	416	0.7719
6kA	0.4551	582	0.7736
7kA	0.4600	551	0.7783

Table B.2: The results on the performance, ϕ_H, calculations for ITO.
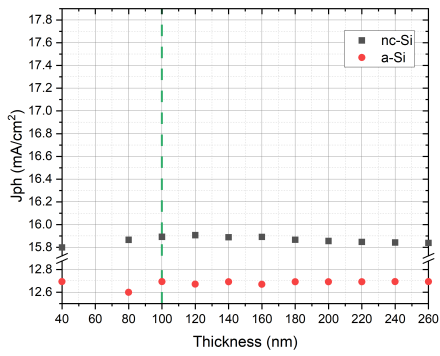
(a) AZO
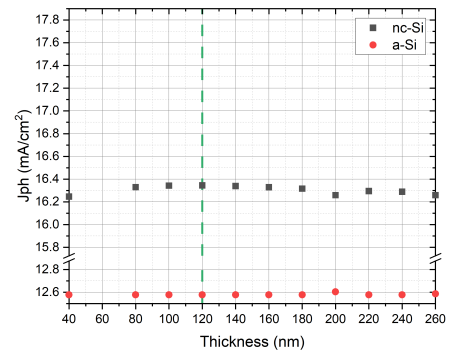
(b) ITO
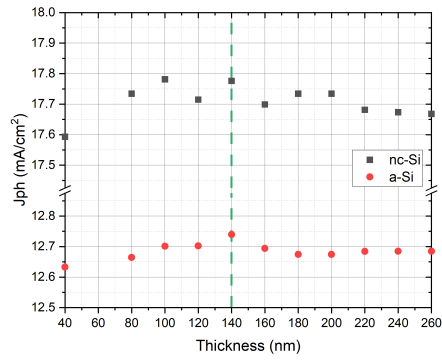
(c) Bilayer

Figure B.1: The J_{ph}, of the top and bottom absorber layers for several i-ZnO back reflector thicknesses.

C
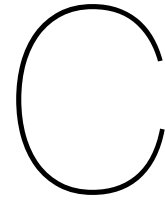
Matlab codes

In this chapter of the appendix all the matlab scripts used within this report are given. The reversed GenPro4 analysis was done for multiple cases which each have their own Matlab script. For clarity these cases are labeled as shown in table C.1.

Label	Case
1	Reversed analysis using RT data and one layer thickness
2	Reversed analysis using RT data and two layer thicknesses
3	Reversed analysis using already determined n values, and A data to determine k

Table C.1: The reversed GP4 cases and their labels

C.1. Call Reversed analysis function - Case 1

```matlab
%-- Written by Lorena Hendrix -- 2023

clear Workspace

%% specify simulation conditions

%%==== COATING THICKNESS(in um)====

Conditions(1).coat_thick = 0.06192;     % Sample 1
Conditions(2).coat_thick = 0.21218;     % Sample 2

%==== WAVELENGTH RANGE ====

wav_short = 300;
wav_long = 1200;

Conditions(1).wav(1) = wav_short;
Conditions(1).wav(2) = wav_long;
Conditions(2).wav(1) = wav_short;
Conditions(2).wav(2) = wav_long;


%==== DATA TYPE ==== (1 = xls, 2 = txt)

Conditions(1).datatype = 1;
```

```matlab
Conditions(2).datatype = 1;

%==== PATH DATA FILE ==== (header at first row, data starts at 2nd row)

Conditions(1).datafile = 'filepath.xlsx';
Conditions(2).datafile = 'filepath.xlsx';


%==== WAVELENGTH COLLUMN ====
Conditions(1).col(1) = 1;        % wavelengths in first collumn
Conditions(2).col(1) = 1;

%==== REFLECTANCE COLLUMN ====
Conditions(1).col(2) = 2;
Conditions(2).col(2) = 2;

%==== TRANSMITTANCE COLLUMN ====
Conditions(1).col(3) = 3;
Conditions(2).col(3) = 3;


%==== INITIAL GUESS N ====

Conditions(1).N_guess = 1 + 0.1i;
Conditions(2).N_guess = 1 + 0.1i;


%==== SAVE OUTPUT FILE ====

Conditions(1).outputfilepath = 'Filepath/';
Conditions(1).outputfilename = 'Filename';
Conditions(2).outputfilepath = 'Filepath/';
Conditions(2).outputfilename = 'Filename';


%% Run reversed analysis

[Output] = ReversedAnalysis(Conditions);
```

C.2. Reversed analysis function - Case 1

```matlab
%-- Written by Lorena Hendrix -- 2023

function [Output] = ReversedAnalysis(Conditions)
tic


num_samples = length(Conditions)
for s = 1:num_samples

    % specify sample conditions for GenPro4

    clear Lay Int         %clear variables 'Lay' and 'Int'

    %===LAYERS===
```

```matlab
    Lay(1).med = 'air';                Lay(1).thi = inf;
    Lay(2).med = 'glass';              Lay(2).thi = 700;
    Lay(3).med = 'air';                Lay(3).thi = inf;

    %===INTERFACES===

    Int(1).coat(1).med = 'something';
    Int(1).coat(1).thi = Conditions(s).coat_thick;

    %===READ RT DATA===
    if Conditions(s).datatype == 1
        data = xlsread(Conditions(s).datafile);

    elseif Conditions(s).datatype ==2
        data = table2array(readtable(Conditions(s).datafile));

    end

    wavel = data(:,Conditions(s).col(1));
    R_meas = data(:,Conditions(s).col(2));
    T_meas = data(:,Conditions(s).col(3));


    if wavel(1) < wavel(2)
        T_meas = flip(T_meas);
        R_meas = flip(R_meas);
        wavel = flip(wavel);
    end

    m = find(wavel == Conditions(s).wav(2)); %first row to read from data
    M = find(wavel == Conditions(s).wav(1)); %last row to read from data

    wavel = wavel(m:M);
    R_meas = R_meas(m:M);
    T_meas = T_meas(m:M);

    %=== Initialize Arrays ===

    n_fit = zeros(M+1 - m,1);
    k_fit = zeros(M+1 - m,1);
    delta = zeros(M+1 - m,1);
    thickness = zeros(M+1 - m,1);
    delta_R = zeros(M+1 - m,1);
    delta_T = zeros(M+1 - m,1);
    delta_R_perc = zeros(M+1 - m,1);
    delta_T_perc = zeros(M+1 - m,1);
    delta_perc = zeros(M+1 - m,1);
    R_sim = zeros(M+1 - m,1);
    T_sim = zeros(M+1 - m,1);
    exitflag = zeros(M+1 - m,1);
    iter = zeros(M+1 - m,1);
    N_iter = zeros(1,1);
    delta_iter = zeros(1,1);
    N_fit = zeros(M+1 - m,2);
    N_min = [0,0];                     %Zero lower boundary
    N_max = [[],[]];
```

```matlab
%=== Initial Guess ===
x = [real(Conditions(s).N_guess),imag(Conditions(s).N_guess)];%,
    Conditions(s).coat_thick];


%=== Find minimum ===

iter_800 = (1200-800)/5;
iter_600 = (1200-600)/5;

opts = optimoptions("patternsearch",'Tolmesh',1e-5,'PollMethod', '
    gpspositivebasis2n');


for i = 1:abs(M-m)+1

    S.wav = [wavel(i)-1,wavel(i)]*10^(-3);


    if i > iter_800
        opts = optimoptions("patternsearch",'Tolmesh',1e-6,'PollMethod
            ', 'gpspositivebasis2n');

    elseif i >= iter_600
        opts = optimoptions("patternsearch",'Tolmesh',1e-7,'PollMethod
            ', 'gpspositivebasis2n');
    end

    [N_fit(i,:),delta(i),exitflag,output] = patternsearch(@
        minimization,x,[],[],[],[],N_min,N_max,[],opts);

    iter(i) = output.iterations;
    x = N_fit(i,:);
    n_fit(i) = x(1);
    k_fit(i) = x(2);


    figure(1)
    plot(wavel, delta, 'o')
    title(string(s))


    Output(s).N.n = n_fit;
    Output(s).N.k = k_fit;
    Output(s).Alpha = 4.*pi.*k_fit.*10^7./wavel;
    Output(s).Delta = delta;
    Output(s).Delta_R = delta_R;
    Output(s).Delta_T = delta_T;
    Output(s).R = R_sim;
    Output(s).T = T_sim;
    Output(s).MSE(1) = sqrt(1/(2*length(delta))*sum((delta_R).^2 + (
        delta_T).^2))*1000;

%===EXPORT DATA TO WORKSPACE FILE===
```

```matlab
            name1 = Conditions(s).outputfilename;
            path_data = Conditions(s).outputfilepath;
            name1 = [path_data name1];
            save(name1,'Conditions','Int','Lay','Output','wavel');

    end



end

function delta = minimization(x)

    N = complex(x(1),x(2))                  %create complex N for genpro4
        input

    Int(1).coat(1).N = [N;N];

    [Lay,Int,out] = GENPRO4(Lay,Int,S);     %call genpro4

    R_sim(i) = Lay(1).abs(2);               %store reflectance from
        simulation
    T_sim(i) = Lay(3).abs(2);               %store transmittance from
        simulation

    delta_R(i) = abs(R_sim(i)-R_meas(i));
    delta_T(i) = abs(T_sim(i)-T_meas(i));
    delta = (delta_R(i) + delta_T(i))           %calculate delta



end
toc
end
```

C.3. Call Reversed analysis function - Case 2

```matlab
    clear Workspace

%% specify simulation conditions

%%==== COATING THICKNESS(in um)====
Conditions(1).coat_thick_R = 0.54706;
Conditions(1).coat_thick_T = 0.54706 - 0.015;



%==== WAVELENGTH RANGE ====

wav_short = 300;
wav_long = 1200;

Conditions(1).wav(1) = wav_short;
Conditions(1).wav(2) = wav_long;



%==== DATA TYPE ==== (1 = xls, 2 = txt)
```

```matlab
Conditions(1).datatype = 1;


%==== PATH DATA FILE ==== (header at first row, data starts at 2nd row)

Conditions(1).datafile = 'filepath.xlsx';

%==== WAVELENGTH COLLUMN ====

Conditions(1).col(1) = 1;


%==== REFLECTANCE COLLUMN ====
Conditions(1).col(2) = 2;


%==== TRANSMITTANCE COLLUMN ====
Conditions(1).col(3) = 3;


%==== INITIAL GUESS N ====

Conditions(1).N_guess = 1 + 0.1i;


%==== SAVE OUTPUT FILE ====

Conditions(1).outputfilepath = 'Filepath/';
Conditions(1).outputfilename = 'Filename';

%% Run reversed analysis

[Output] = ReversedAnalysis_2thicknesses(Conditions);
```

C.4. Reversed analysis function - Case 2

```matlab
function [Output] = ReversedAnalysis_2thicknesses(Conditions)
tic

num_samples = length(Conditions)

for s = 1:int64(num_samples)

    % specify sample conditions for GenPro4

    clear Lay Int          %clear variables 'Lay' and 'Int'

    %===LAYERS===
    Lay(1).med = 'air';              Lay(1).thi = inf;
    Lay(2).med = 'glass';            Lay(2).thi = 700;
    Lay(3).med = 'air';              Lay(3).thi = inf;

    %===INTERFACES===
```

```matlab
    Int(1).coat(1).med = 'something';



    %===READ RT DATA===
    if Conditions(s).datatype == 1
        data = xlsread(Conditions(s).datafile);

    elseif Conditions(s).datatype ==2
        data = table2array(readtable(Conditions(s).datafile));

    end

    wavel = data(:,Conditions(s).col(1));
    R_meas = data(:,Conditions(s).col(2));
    T_meas = data(:,Conditions(s).col(3));


    if wavel(1) < wavel(2)
        T_meas = flip(T_meas);
        R_meas = flip(R_meas);
        wavel = flip(wavel);
    end

    m = find(wavel == Conditions(s).wav(2)) %first row to read from data
    M = find(wavel == Conditions(s).wav(1)); %last row to read from data

    wavel = wavel(m:M)
    R_meas = R_meas(m:M);
    T_meas = T_meas(m:M);

    %=== Initialize Arrays ===

    n_fit = zeros(M+1 - m,1);
    k_fit = zeros(M+1 - m,1);
    delta = zeros(M+1 - m,1);
    thickness = zeros(M+1 - m,1);
    delta_R = zeros(M+1 - m,1);
    delta_T = zeros(M+1 - m,1);
    R_sim = zeros(M+1 - m,1);
    T_sim = zeros(M+1 - m,1);
    exitflag = zeros(M+1 - m,1);
    iter = zeros(M+1 - m,1);
    N_iter = zeros(1,1);
    delta_iter = zeros(1,1);
    N_fit = zeros(M+1 - m,2);
    N_min = [0,0];%,Conditions(s).coat_thick*(1 - 0.15)];
    N_max = [[],[]];%,Conditions(s).coat_thick*(1 + 0.15)];


    %=== Initial Guess ===
    x = [real(Conditions(s).N_guess),imag(Conditions(s).N_guess)];


    %=== Find minimum ===

    iter_800 = (1200-800)/5;
```

```matlab
iter_600 = (1200-600)/5;

opts = optimoptions("patternsearch",'Tolmesh',1e-5,'PollMethod', '
    gpspositivebasis2n');


for i = 1:int64(abs(M-m)+1)

    S.wav = [wavel(i)-1,wavel(i)]*10^(-3);


    if i > iter_800
        opts = optimoptions("patternsearch",'Tolmesh',1e-6,'PollMethod
            ', 'gpspositivebasis2n');

    elseif i >= iter_600
        opts = optimoptions("patternsearch",'Tolmesh',1e-7,'PollMethod
            ', 'gpspositivebasis2n');
    end

    [N_fit(i,:),delta(i),exitflag,output] = patternsearch(@
        minimization,x,[],[],[],[],N_min,N_max,[],opts);

    iter(i) = output.iterations;
    x = N_fit(i,:);
    n_fit(i) = x(1);
    k_fit(i) = x(2);

    figure(1)
    plot(wavel, delta, 'o')
    %ylim([0 0.3])
    title(string(s))


    % Output

    Output(s).N.n = n_fit;
    Output(s).N.k = k_fit;
    Output(s).Alpha = 4.*pi.*k_fit.*10^7./wavel;
    Output(s).Delta = delta;
    Output(s).Delta_R = delta_R;
    Output(s).Delta_T = delta_T;
    Output(s).R = R_sim;
    Output(s).T = T_sim;
    Output(s).MSE(1) = sqrt(1/(2*length(delta))*sum((delta_R).^2 + (
        delta_T).^2))*1000;

    %===EXPORT DATA TO WORKSPACE FILE===

    name1 = Conditions(s).outputfilename;
    path_data = Conditions(s).outputfilepath;
    name1 = [path_data name1];
    save(name1,'Conditions','Int','Lay','Output','wavel');

end
```

```matlab
end
function delta = minimization(x)

    N = complex(x(1),x(2))                  %create complex N for genpro4
        input

    Int(1).coat(1).N = [N;N];

    Int(1).coat(1).thi = Conditions(s).coat_thick_R;
    [Lay,Int,out] = GENPRO4(Lay,Int,S);     %call genpro4
    R_sim(i) = Lay(1).abs(2);               %store reflectance from
        simulation
    delta_R(i) = abs(R_sim(i)-R_meas(i));


    Int(1).coat(1).thi = Conditions(s).coat_thick_T;
    [Lay,Int,out] = GENPRO4(Lay,Int,S);     %call genpro4
    T_sim(i) = Lay(3).abs(2);               %store transmittance from
        simulation
    delta_T(i) = abs(T_sim(i)-T_meas(i));


    delta = (delta_R(i) + delta_T(i))         %calculate delta


end
toc
end
```

C.5. Call reversed analysis function - Case 3

```matlab
    clear Workspace

%% specify simulation conditions

%%==== COATING THICKNESS(in um)====

Conditions(1).coat_thick = 0.08566;

%==== WAVELENGTH RANGE ====

wav_short = 300;
wav_long = 1200;

Conditions(1).wav(1) = wav_short;
Conditions(1).wav(2) = wav_long;

%==== DATA TYPE ==== (1 = xls, 2 = txt)

Conditions(1).datatype = 1;


%==== PATH DATA FILE ==== (header at first row, data starts at 2nd row)

Conditions(1).datafile = 'filepath.xlsx';
```

```matlab
%==== WAVELENGTH COLLUMN ====
Conditions(1).col(1) = 1;        % wavelengths in first collumn



%==== Absorptance COLLUMN ====
Conditions(1).col(2) = 2;



%==== REFRACTIVE INDEX COLLUMN ====
Conditions(1).col(3) = 3;



%==== INITIAL GUESS k ====

Conditions(1).k_guess = 0.1;

%==== SAVE OUTPUT FILE ====

Conditions(1).outputfilepath = 'Filepath/';
Conditions(1).outputfilename = 'Filename';

%% Run reversed analysis

[Output] = ReversedAnalysis_A(Conditions);
```

C.6. Reversed analysis function - Case 3

```matlab
function [Output] = ReversedAnalysis_A(Conditions)
tic

num_samples = length(Conditions)

for s = 1:num_samples

    % specify sample conditions for GenPro4

    clear Lay Int            %clear variables 'Lay' and 'Int'

    %===LAYERS===
    Lay(1).med = 'air';               Lay(1).thi = inf;
    Lay(2).med = 'quartz';            Lay(2).thi = 1100;
    Lay(3).med = 'air';               Lay(3).thi = inf;

    %===INTERFACES===

    Int(1).coat(1).med = 'something';
    Int(1).coat(1).thi = Conditions(s).coat_thick;

    %===READ RT DATA===
    if Conditions(s).datatype == 1
        data = xlsread(Conditions(s).datafile);
```

```matlab
    elseif Conditions(s).datatype ==2
        data = table2array(readtable(Conditions(s).datafile));

    end

    wavel = data(:,Conditions(s).col(1));
    A_meas = data(:,Conditions(s).col(2));
    refractive = data(:,Conditions(s).col(3));


    if wavel(1) < wavel(2)
        A_meas = flip(A_meas);
        refractive = flip(refractive);
        wavel = flip(wavel);
    end

    m = find(wavel == Conditions(s).wav(2)); %first row to read from data
    M = find(wavel == Conditions(s).wav(1)); %last row to read from data

    wavel = wavel(m:M);
    A_meas = A_meas(m:M);
    refractive = refractive(m:M);

    %=== Initialize Arrays ===

    delta_A = zeros(M+1 - m,1);
    thickness = zeros(M+1 - m,1);
    delta_perc = zeros(M+1 - m,1);
    A_sim = zeros(M+1 - m,1);
    exitflag = zeros(M+1 - m,1);
    iter = zeros(M+1 - m,1);
    k_iter = zeros(1,1);
    delta_iter = zeros(1,1);
    k_min = 0;              %Lower boundary
    k_max = [];


    %=== Initial Guess ===
    x = Conditions(s).k_guess;

    %=== Find minimum ===


    iter_800 = (1200-800)/5;
    iter_600 = (1200-600)/5;

    opts = optimoptions("patternsearch",'Tolmesh',1e-5,'PollMethod', '
        gpspositivebasis2n');


    for i = 1:abs(M-m)+1

        S.wav = [wavel(i)-1,wavel(i)]*10^(-3);
```

```matlab
        if i > iter_800
            opts = optimoptions("patternsearch",'Tolmesh',1e-6,'PollMethod
                ', 'gpspositivebasis2n');

        elseif i >= iter_600
            opts = optimoptions("patternsearch",'Tolmesh',1e-7,'PollMethod
                ', 'gpspositivebasis2n');
        end

        n = refractive(i);

        [k_fit(i),delta_A(i),exitflag,output] = patternsearch(@
            minimization,x,[],[],[],[],k_min,k_max,[],opts);

        iter(i) = output.iterations;
        x = k_fit(i);

        figure(1)
        plot(wavel, delta_A, 'o')
        title(string(s))


        % Output

        Output(s).N.k = k_fit;
        Output(s).Alpha = 4.*pi.*k_fit.*10^7./wavel;
        Output(s).Delta = delta_A;
        Output(s).A = A_sim;
        Output(s).MSE(1) = sqrt(1/(2*length(delta_A))*sum((delta_A).^2))
            *1000;

        %===EXPORT DATA TO WORKSPACE FILE===

        name1 = Conditions(s).outputfilename;
        path_data = Conditions(s).outputfilepath;
        name1 = [path_data name1];
        save(name1,'Conditions','Int','Lay','Output','wavel');

    end

end
function delta_A = minimization(x)
    path_data = 'Data_reversedAnalysis\ITO20\Tolmesh_negSetZero_basisNp1_e
        -4_basis2n_e-5_e-7\';

    N = complex(n,x)                    %create complex N for genpro4 input

    Int(1).coat(1).N = [N;N];

    [Lay,Int,out] = GENPRO4(Lay,Int,S);    %call genpro4

    R_sim(i) = Lay(1).abs(2);              %store reflectance from
        simulation
    T_sim(i) = Lay(3).abs(2);              %store transmittance from
        simulation
    A_sim(i) = 1-R_sim(i)-T_sim(i);
```

```matlab
    delta_A = abs(A_sim(i)-A_meas(i));              %calculate delta


end
toc
end
```

C.7. Example of solar cell simulation script

```matlab
    clear Lay Int S

load('EZ500e_20um') %load texturing

%===LAYERS===
Lay(1).med = 'air';                     Lay(1).thi = inf;
Lay(2).med = 'glass';                   Lay(2).thi = 700;
Lay(3).med = 'a-Si(i)';                 Lay(3).thi = 0.220;
Lay(4).med = 'nc-Si(i)';                Lay(4).thi = 2;
Lay(5).med = 'air';                     Lay(5).thi = inf;


%Interface 1
Int(1).model= 'flat';


%Interface 2
Int(2).model = 'ray';
Int(2).Z = -EZ500e_20um;
Int(2).xy = [20,20];

Int(2).coat(1).med = 'IOH_150(200)_SE';     Int(2).coat(1).thi = 0.100 ;
Int(2).coat(2).med = 'ZnO23_SE';            Int(2).coat(2).thi = 0.5;
Int(2).coat(3).med = 'nc-SiOx(p)';          Int(2).coat(3).thi = 0.015;

%Interface 3
Int(3).model = 'ray';
Int(3).Z = -EZ500e_20um;
Int(3).xy = [20,20];

Int(3).coat(1).med = 'nc-SiOx(n)';          Int(3).coat(1).thi = 0.020;
Int(3).coat(2).med = 'nc-SiOx(p)';          Int(3).coat(2).thi = 0.015;

%Interface 4
Int(4).model = 'ray';
Int(4).Z =- EZ500e_20um;
Int(4).xy = [20,20];

Int(4).coat(1).med = 'nc-SiOx(n)';          Int(4).coat(1).thi = 0.020;
Int(4).coat(2).med = 'ZnO23_SE';             Int(4).coat(2).thi = 0.080;
Int(4).coat(3).med = 'Ag';                  Int(4).coat(3).thi = 0.300;



S.wav = 0.3:0.02:1.2;
```

```
[Lay,Int,out] = GENPRO4(Lay,Int,S)

out.wav=1000*out.wav;
out.abp=out.abp';
save('Filename')
```

C.8. Example of solar cell simulation script varying layer thickness

```
clear Lay Int

load('EZ500e_20um') %load texturing

%===LAYERS===
Lay(1).med = 'air';                              Lay(1).thi = inf;
Lay(2).med = 'glass';                            Lay(2).thi = 700;
Lay(3).med = 'a-Si(i)';                          Lay(3).thi = 0.220;
Lay(4).med = 'nc-Si(i)';                         Lay(4).thi = 2;
Lay(5).med = 'air';                              Lay(5).thi = inf;


%===INTERFACES===
%Interface 1

Int(1).model = 'flat';


%Interface 2

Int(2).model = 'ray';
Int(2).Z = -EZ500e_20um;
Int(2).xy = [20,20];

Int(2).coat(1).med = 'IOH_150(200)_SE';
Int(2).coat(2).med = 'ZnO23_SE';
Int(2).coat(3).med = 'nc-SiOx(p)';              Int(2).coat(3).thi = 0.015;

%interface 3
Int(3).model = 'ray';
Int(3).Z = -EZ500e_20um;
Int(3).xy = [20,20];

Int(3).coat(1).med = 'nc-SiOx(n)';              Int(3).coat(1).thi = 0.020;
Int(3).coat(2).med = 'nc-SiOx(p)';              Int(3).coat(2).thi = 0.015;

%Interface 4
Int(4).model = 'ray';
Int(4).Z = -EZ500e_20um;
Int(4).xy = [20,20];

Int(4).coat(1).med = 'nc-SiOx(n)';              Int(4).coat(1).thi = 0.020;
Int(4).coat(2).med = 'ZnO23_SE';                 Int(4).coat(2).thi = 0.140;
Int(4).coat(3).med = 'Ag';                      Int(4).coat(3).thi = 0.300;
```

```matlab
%===Overide default settings===
S.wav = 0.3:0.01:1.2;

Thi_IOH = 0.05:0.05:0.6; %TCO layer thickness range
Thi_ZnO = 0.05:0.05:1;



R = zeros(length(Thi_IOH),length(Thi_ZnO),length(S.wav));
A_glass = zeros(length(Thi_IOH),length(Thi_ZnO),length(S.wav));
A_IOH = zeros(length(Thi_IOH),length(Thi_ZnO),length(S.wav));
A_ZnO= zeros(length(Thi_IOH),length(Thi_ZnO),length(S.wav));
A_SiOx_p_1 = zeros(length(Thi_IOH),length(Thi_ZnO),length(S.wav));
A_aSi = zeros(length(Thi_IOH),length(Thi_ZnO),length(S.wav));
A_SiOx_n_1 = zeros(length(Thi_IOH),length(Thi_ZnO),length(S.wav));
A_SiOx_p_2 = zeros(length(Thi_IOH),length(Thi_ZnO),length(S.wav));
A_ncSi = zeros(length(Thi_IOH),length(Thi_ZnO),length(S.wav));
A_SiOx_n_2 = zeros(length(Thi_IOH),length(Thi_ZnO),length(S.wav));
A_ZnO_back = zeros(length(Thi_IOH),length(Thi_ZnO),length(S.wav));
A_Ag = zeros(length(Thi_IOH),length(Thi_ZnO),length(S.wav));

T = zeros(length(Thi_IOH),length(Thi_ZnO),length(S.wav));

A_IOH_average = zeros(length(Thi_IOH),length(Thi_ZnO));
A_ZnO_average = zeros(length(Thi_IOH),length(Thi_ZnO));
A_aSi_average = zeros(length(Thi_IOH),length(Thi_ZnO));
A_ncSi_average = zeros(length(Thi_IOH),length(Thi_ZnO));
A_AZO_average = zeros(length(Thi_IOH),length(Thi_ZnO));

J_R = zeros(length(Thi_IOH),length(Thi_ZnO));
J_T = zeros(length(Thi_IOH),length(Thi_ZnO));
J_glass = zeros(length(Thi_IOH),length(Thi_ZnO));
J_IOH = zeros(length(Thi_IOH),length(Thi_ZnO));
J_ZnO = zeros(length(Thi_IOH),length(Thi_ZnO));
J_SiOx_p_1 = zeros(length(Thi_IOH),length(Thi_ZnO));
J_aSi = zeros(length(Thi_IOH),length(Thi_ZnO));
J_SiOx_n_1= zeros(length(Thi_IOH),length(Thi_ZnO));
J_SiOx_p_2 = zeros(length(Thi_IOH),length(Thi_ZnO));
J_ncSi = zeros(length(Thi_IOH),length(Thi_ZnO));
J_SiOx_n_2 = zeros(length(Thi_IOH),length(Thi_ZnO));
J_ZnO_back = zeros(length(Thi_IOH),length(Thi_ZnO));
J_Ag = zeros(length(Thi_IOH),length(Thi_ZnO));
Thick_aSi = zeros(length(Thi_IOH),length(Thi_ZnO));
Thick_ncSi = zeros(length(Thi_IOH),length(Thi_ZnO));


for i = 1:length(Thi_IOH)
    for j = 1:length(Thi_ZnO)
        Thi_IOH(i)
        Thi_ZnO(j)

        Int(2).coat(1).thi = Thi_IOH(i);
        Int(2).coat(2).thi = Thi_ZnO(j);
```

```matlab
        [Lay,Int,out] = GENPRO4(Lay,Int,S);

        R(i,j,:) = Lay(1).abs(:);
        A_glass(i,j,:) = Lay(2).abs(:);
        A_IOH(i,j,:) = Int(2).coat(1).abs(:);
        A_ZnO(i,j,:) = Int(2).coat(2).abs(:);
        A_SiOx_p_1(i,j,:) = Int(2).coat(3).abs(:);
        A_aSi(i,j,:) = Lay(3).abs(:);
        A_SiOx_n_1(i,j,:) = Int(3).coat(1).abs(:);
        A_SiOx_p_2(i,j,:) = Int(3).coat(2).abs(:);
        A_ncSi(i,j,:) = Lay(4).abs(:);
        A_SiOx_n_2(i,j,:) = Int(4).coat(1).abs(:);
        A_ZnO_back(i,j,:) = Int(4).coat(2).abs(:);
        A_Ag(i,j,:) = Int(4).coat(3).abs(:);

        T(i,j,:) = Lay(5).abs(:);

        A_IOH_average(i,j,:) = sum(A_IOH(i,j,:))/length(S.wav);
        A_ZnO_average(i,j,:) = sum(A_ZnO(i,j,:))/length(S.wav);
        A_aSi_average(i,j,:) = sum(A_aSi(i,j,:))/length(S.wav);
        A_ncSi_average(i,j,:) = sum(A_ncSi(i,j,:))/length(S.wav);
        A_ZnO_back_average(i,j,:) = sum(A_ZnO_back(i,j,:))/length(S.wav);

        J_R(i,j,:) = Lay(1).cur;
        J_glass(i,j,:) = Lay(2).cur;
        J_IOH(i,j,:) = Int(2).coat(1).cur;
        J_ZnO(i,j,:) = Int(2).coat(2).cur;
        J_SiOx_p_1(i,j,:) = Int(2).coat(3).cur;
        J_aSi(i,j,:) = Lay(3).cur;
        J_SiOx_n_1(i,j,:) = Int(3).coat(1).cur;
        J_SiOx_p_2(i,j,:) = Int(3).coat(2).cur;
        J_ncSi(i,j,:) = Lay(4).cur;
        J_SiOx_n_2(i,j,:) = Int(4).coat(1).cur;
        J_ZnO_back(i,j,:) = Int(4).coat(2).cur;
        J_Ag(i,j,:) = Int(4).coat(3).cur;
        J_T(i,j,:) = Lay(5).cur;


        save('Filename');


    end

end
```

C.9. Call solar cell current matching function

```matlab
clear Lay Int S

load('EZ500e_20um') %load texturing

%===LAYERS===
Lay(1).med = 'air';                              Lay(1).thi = inf;
```

```matlab
Lay(2).med = 'glass';                          Lay(2).thi = 700;
Lay(3).med = 'a-Si(i)';                        Lay(3).thi = 0.5;
Lay(4).med = 'nc-Si(i)';                       Lay(4).thi = 2;
Lay(5).med = 'air';                            Lay(5).thi = inf;


%Interface 1
Int(1).model= 'flat';


%Interface 2
Int(2).model = 'ray';
Int(2).Z = -EZ500e_20um;
Int(2).xy = [20,20];

Int(2).coat(1).med = '3kA_SE';       Int(2).coat(1).thi = 0.240 ;
Int(2).coat(2).med = 'nc-SiOx(p)';           Int(2).coat(2).thi = 0.015;

%Interface 3
Int(3).model = 'ray';
Int(3).Z = - EZ500e_20um;
Int(3).xy = [20,20];

Int(3).coat(1).med = 'nc-SiOx(n)';           Int(3).coat(1).thi = 0.020;
Int(3).coat(2).med = 'nc-SiOx(p)';           Int(3).coat(2).thi = 0.015;

%Interface 4
Int(4).model= 'ray';
Int(4).Z = -EZ500e_20um;
Int(4).xy = [20,20];

Int(4).coat(1).med = 'nc-SiOx(n)';           Int(4).coat(1).thi = 0.020;
Int(4).coat(2).med = 'Zno23_SE';              Int(4).coat(2).thi = 0.120;
Int(4).coat(3).med = 'Ag';                   Int(4).coat(3).thi = 0.300;



S.wav = 0.3:0.02:1.2;

[Lay,Int,out] = CurrentMatcher2(Lay,Int,S)

out.wav=1000*out.wav;
out.abp=out.abp';
save('Filename')
```

C.10. solar cell current matching function

```matlab
function [Lay,Int,out] = CurrentMatcher2(Lay,Int,S)
    f = 0;

    x = Lay(3).thi;
    x_min = 1;
    x_max = 3;

    options = optimset('TolFun',1e-3,'TolX',2000)
```

```matlab
    [Thi_curMatch,delta,f] = fminsearch(@minimization,x, options);

    function delta = minimization(x)

        Lay(3).thi = x;

        [Lay,Int,out] = GENPRO4(Lay,Int,S);        %call genpro4

        Jph_aSi = Lay(3).cur;
        Jph_ncSi = Lay(4).cur;

        delta = abs(Jph_aSi - Jph_ncSi)             %calculate delta
        Thi_curMatch = x;

    end
end
```

C.11. Rearrange 2D bi-layer thickness data

```matlab
load('Workspace_file')

Thi_IOH = Thi_IOH*1000;
Thi_ZnO = Thi_ZnO*1000;
n= 0;

for i = 1:length(Thi)
    for j = 1:length(Thi_IOH)
        for k = 1:length(Thi_ZnO)

            if Thi_IOH(j)+Thi_ZnO(k) == Thi(i)

                n = n+1;
                A = [Thi_IOH(j) Thi_ZnO(k)];
                A_string = string(A);
                Thi_match(n) = join(A_string,"+");
                J_aSi_new(i,n) = J_aSi(j,k);
                J_ncSi_new(i,n) = J_ncSi(j,k);


            end


        end
    end
end
```

Bibliography

[1]   Adwait Atul Apte. "Textured back reflectors for thin-film silicon solar cells". In: (2015).

[2]   L Barraud et al. "Hydrogen-doped indium oxide/indium tin oxide bilayers for high-efficiency silicon heterojunction solar cells". In: *Solar Energy Materials and Solar Cells* 115 (2013), pp. 151–156.

[3]   AC Boccara et al. "Sensitive photothermal deflection technique for measuring absorption in optically thin media". In: *Optics Letters* 5.9 (1980), pp. 377–379.

[4]   KL Chopra, S Major, and DK Pandya. "Transparent conductors—a status review". In: *Thin solid films* 102.1 (1983), pp. 1–46.

[5]   IR Cisneros-Contreras, AL Muñoz-Rosas, and A Rodríguez-Gómez. "Resolution improvement in Haacke's figure of merit for transparent conductive films". In: *Results in Physics* 15 (2019), p. 102695.

[6]   Pan Dai et al. "Transparent conducting indium-tin-oxide (ITO) film as full front electrode in III–V compound solar cell". In: *Chinese Physics B* 26.3 (2017), p. 037305.

[7]   AS Ferlauto et al. "Analytical model for the optical functions of amorphous semiconductors from the near-infrared to ultraviolet: Applications in thin film photovoltaics". In: *Journal of Applied Physics* 92.5 (2002), pp. 2424–2436.

[8]   Hiroyuki Fujiwara and Robert W Collins. *Spectroscopic ellipsometry for photovoltaics*. Vol. 1. Springer, 2018.

[9]   Thomas Germer, Joanne C Zwinkels, and Benjamin K Tsai. *Spectrophotometry: Accurate measurement of optical properties of materials*. Elsevier, 2014.

[10]   Martin Green et al. "Solar cell efficiency tables (version 57)". In: *Progress in photovoltaics: research and applications* 29.1 (2021), pp. 3–15.

[11]   C. Han. "High-Mobility TCO-Based Contacting Schemes for c-Si Solar Cells". English. PhD thesis. Delft University of Technology, 2022. ISBN: 978-94-6421-734-6. DOI: `10.4233/uuid:d6f35adf-486e-453a-9ae9-679a81105bed`.

[12]   W. Theiss Hard- and Aachen Software. *Spectrum interpretation by simulation*. `http://www.mtheiss.com/docs/scout2/`. 2012.

[13]   Inc J. A. Woollam Co. *CompleteEASE™ Data Analysis Manual*. J. A. Woollam Co., Inc, 2011.

[14]   Warren B Jackson et al. "Photothermal deflection spectroscopy and detection". In: *Applied optics* 20.8 (1981), pp. 1333–1344.

[15]   Klaus Jäger. "On the scalar scattering theory for thin-film solar cells". In: (2012).

[16]   GE Jellison Jr. "Spectroscopic ellipsometry data analysis: measured versus calculated quantities". In: *Thin solid films* 313 (1998), pp. 33–39.

[17]   Prashand Kalpoe. "Transparent conductive oxide bi-layer as front contact for multijunction thin film silicon photovoltaic cells". In: (2023).

[18]   Charles C Kim et al. "Modeling the optical dielectric function of semiconductors: extension of the critical-point parabolic-band approximation". In: *Physical Review B* 45.20 (1992), p. 11749.

[19]   H Kim et al. "Effect of film thickness on the properties of indium tin oxide thin films". In: *Journal of applied physics* 88.10 (2000), pp. 6021–6025.

[20]   Ajay Kumar et al. "Increased efficiency of 23% for CIGS solar cell by using ITO as front contact". In: *Materials Today: Proceedings* 28 (2020), pp. 361–365.

[21]   Gianluca Limodio et al. "Modulated surface texturing of temporary Al foils substrates for high-efficiency thin-film, flexible solar cells". In: *2021 IEEE 48th Photovoltaic Specialists Conference (PVSC)*. IEEE. 2021, pp. 1103–1105.

[22]   MATLAB®. *Matlab*. Version R2019b. URL: `https://mathworks.com/`.

[23]   Mamoru Mizuhashi. "Electrical properties of vacuum-deposited indium oxide and indium tin oxide films". In: *Thin solid films* 70.1 (1980), pp. 91–100.

[24]   Joachim Müller et al. "TCO and light trapping in silicon thin film solar cells". In: *Solar Energy* 77.6 (Dec. 2004), pp. 917–930. ISSN: 0038092X. DOI: `10.1016/j.solener.2004.03.015`.

[25]   Joachim Müller et al. "TCO and light trapping in silicon thin film solar cells". In: *Solar energy* 77.6 (2004), pp. 917–930.

[26]   Stephen K O'Leary, SR Johnson, and PK Lim. "The relationship between the distribution of electronic states and the optical absorption spectrum of an amorphous semiconductor: An empirical analysis". In: *Journal of applied physics* 82.7 (1997), pp. 3334–3340.

[27]   PerkinElmer. *Technical Specifications for the LAMBDA 1050 UV/Vis/NIR and LAMBDA 950 UV/Vis/NIR Spectrophotometers*. PerkinElmer, Inc, 2007.

[28]   Open education Resource LibreTexts Project. *Spectroscopic Methods*. LibreTexts, 2019.

[29]   Hitoshi Sai, Takuya Matsui, and Koji Matsubara. "Stabilized 14.0%-efficient triple-junction thin-film silicon solar cell". In: *Applied Physics Letters* 109.18 (2016), p. 183506.

[30]   Hitoshi Sai et al. "Triple-junction thin-film silicon solar cell fabricated on periodically textured substrate with a stabilized efficiency of 13.6%". In: *Applied Physics Letters* 106.21 (2015), p. 213902.

[31]   Rudi Santbergen. "Manual for solar cell optical simulation software: GENPRO4". In: *Photovoltaic Materials and Devices, Delft University of Technology* (2016).

[32]   Rudi Santbergen and et al. "GenPro4 optical model for solar cell simulation and its application to multijunction solar cells." In: *IEEE journal of photovoltaics* 7.3 (2017), pp. 919–926.

[33]   Rudi Santbergen, Arno HM Smets, and Miro Zeman. "Optical model for multilayer structures with coherent, partly coherent and incoherent layers". In: *Optics express* 21.102 (2013), A262–A267.

[34]   K Sato et al. "Highly textured SnO2: F TCO films for a-Si solar cells". In: *Asahi Garasu Kenkyu Hokoku (Reports of the Research Lab., Asahi Glass Co.);(Japan)* 42.2 (1993).

[35]   Jianhua Shi et al. "MoOx modified ITO/a-Si: H (p) contact for silicon heterojunction solar cell application". In: *Materials Research Bulletin* 97 (2018), pp. 176–181.

[36]   Arno HM Smets et al. *Solar Energy: The physics and engineering of photovoltaic conversion, technologies and systems*. UIT Cambridge, 2015.

[37]   Jonathan D Spear, Richard E Russo, and Robert J Silva. "Collinear photothermal deflection spectroscopy with light-scattering samples". In: *Applied optics* 29.28 (1990), pp. 4225–4234.

[38]   Olaf Stenzel et al. *The physics of thin film optical spectra*. Springer, 2015.

[39]   K Tanaka et al. "Photothermal deflection spectroscopy of chalcogenide glasses". In: *Journal of applied physics* 91.1 (2002), pp. 125–128.